

Oxidation of Light Alkanes Using Photocatalytic Thin Films

by

Troy Matthew Twesme

A dissertation submitted in partial fulfillment of
the requirements for the degree of

Doctor of Philosophy

(Civil & Environmental Engineering)

at the

UNIVERSITY OF WISCONSIN-MADISON

2006

Report Documentation Page				Form Approved OMB No. 0704-0188	
Public reporting burden for the collection of information is estimated to average 1 hour per response, including the time for reviewing instructions, searching existing data sources, gathering and maintaining the data needed, and completing and reviewing the collection of information. Send comments regarding this burden estimate or any other aspect of this collection of information, including suggestions for reducing this burden, to Washington Headquarters Services, Directorate for Information Operations and Reports, 1215 Jefferson Davis Highway, Suite 1204, Arlington VA 22202-4302. Respondents should be aware that notwithstanding any other provision of law, no person shall be subject to a penalty for failing to comply with a collection of information if it does not display a currently valid OMB control number.					
1. REPORT DATE 01 FEB 2007		2. REPORT TYPE N/A		3. DATES COVERED -	
4. TITLE AND SUBTITLE Oxidation of Light Alkanes Using Photocatalytic Thin Films				5a. CONTRACT NUMBER	
				5b. GRANT NUMBER	
				5c. PROGRAM ELEMENT NUMBER	
6. AUTHOR(S)				5d. PROJECT NUMBER	
				5e. TASK NUMBER	
				5f. WORK UNIT NUMBER	
7. PERFORMING ORGANIZATION NAME(S) AND ADDRESS(ES) University of Wisconsin-Madison				8. PERFORMING ORGANIZATION REPORT NUMBER	
9. SPONSORING/MONITORING AGENCY NAME(S) AND ADDRESS(ES)				10. SPONSOR/MONITOR'S ACRONYM(S)	
				11. SPONSOR/MONITOR'S REPORT NUMBER(S)	
12. DISTRIBUTION/AVAILABILITY STATEMENT Approved for public release, distribution unlimited					
13. SUPPLEMENTARY NOTES The original document contains color images.					
14. ABSTRACT					
15. SUBJECT TERMS					
16. SECURITY CLASSIFICATION OF:			17. LIMITATION OF ABSTRACT UU	18. NUMBER OF PAGES 159	19a. NAME OF RESPONSIBLE PERSON
a. REPORT unclassified	b. ABSTRACT unclassified	c. THIS PAGE unclassified			

The views expressed in this thesis are those of the author and do not reflect the official policy or position of the United States Air Force, Department of Defense, or the U.S. Government.

Oxidation of Light Alkanes Using Photocatalytic Thin Films

Troy Matthew Twesme

Under the supervision of Professor Marc A. Anderson

At the University of Wisconsin-Madison

This investigation studied the photocatalytic oxidation of light alkanes using photocatalytic thin films. In the research presented, nearly complete oxidation of isobutane, n-butane and propane using $\text{ZrO}_2/\text{TiO}_2$ thin films in a single pass reactor was demonstrated. The importance of reactor design on the effectiveness of the photocatalytic reaction is discussed in terms of photocatalyst packing and adequate illumination for catalyst activation. The influence of relative humidity in the contaminant feed stream and the reactor operating temperature were evaluated to establish optimal operating conditions for the photocatalytic reactor. Further photocatalytic studies used propane as a probe compound to investigate metal-modification of photocatalytic thin films as a means to improve propane oxidation and mineralization. Six precious metals (Ag, Au, Pd, Pt, Rh, and Ru) were tested at 1 weight percent loadings in TiO_2 , $\text{SiO}_2/\text{TiO}_2$, and $\text{ZrO}_2/\text{TiO}_2$ thin films. The photocatalytic reactor was operated at temperatures up to 100°C with the expectation that a thermal catalytic enhancement due to the precious metals would be observed. Propane conversion data revealed that at 1% loading, the addition of metals to the thin films reduced the activity for conversion of propane, regardless of temperature. However, the reactor temperature

significantly affected light irradiance. Reaction rates adjusted for the influence of temperature on reactor irradiance revealed the highest reaction rates occurred at 100°C, but evaluation of Langmuir-Hinshelwood-Hougen-Watson kinetics showed that temperature significantly reduced the surface adsorption of propane. Of the 21 materials tested, an unmodified $\text{ZrO}_2/\text{TiO}_2$ thin film had the best activity for propane conversion and mineralization.

Lastly, a novel method to investigate the photoinduced change in surface potential of photocatalytic thin films was investigated. Using AFM-captured surface potential measurements we demonstrated a decreasing change in potential with higher platinum loadings in $\text{ZrO}_2/\text{TiO}_2$ thin films. The platinum loaded films showed a similar trend of decreasing photocatalytic activity as platinum content increased. It was concluded that surface potential measurements may provide a means to quickly evaluate the photoactivity of thin film coatings for gas phase applications, thereby significantly reducing the time and effort needed to perform reaction kinetic studies.

Marc A. Anderson, Professor

Acknowledgments

First and foremost I want to thank my advisor, Dr. Marc Anderson, for his guidance, support, and patience throughout the course of my research. Marc's willingness to let me explore countless tangents to my primary research allowed me to learn much more than I could ever convey in the pages of this thesis. I also must thank Dr. Dean Tompkins for his mentorship and friendship during my time at UW. His assistance was instrumental in the setup of experiments, analysis of results, and many other intangibles along the way.

Thanks to Dr. Walt Zeltner for the many rapid reviews in the past few weeks and for putting up with the invasion of an engineer into his lab for the last three years. I would like to thank Isabel Tejedor-Tejedor, Louise Tortorelli, Jeff Brownson, Andy Rutter, Shawn Chadwick and Kevin Leonard for their advice and helpful discussions of all topics, relevant to research or not. I would also like to thank the many undergraduates who helped me along the way, including, Chad Koci, Tyler Nelson, Jes Sanfilippo, Jen Sanfilippo, Ramsey Kropp, and Adam Johnston. Thanks also to Kari Myli and others at Cardinal Glass CG in Spring Green for the access to your lab that proved vital to completing my research.

I extend a special thanks to my parents, for always supporting me and for instilling in me the work ethic that has gotten me this far in life. Finally, and most importantly, I thank my wife and son for their unending love and support during this journey. My son was always ready to wash away the stress and frustrations of a long day with the simple *request* "Come play with me Dad!?" While my wife worked overtime keeping our lives in order so I could focus on research. I could have never done it without the two of them.

Table of Contents

	Page
Dedication	i
Abstract.....	ii
Acknowledgements	iv
List of Tables	vii
List of Figures	ix
Nomenclature	xv
1 Introduction.....	1
2 Literature Review	5
2.1 Photocatalysis	5
2.2 Mechanisms of Photocatalysis	5
2.3 Reaction Kinetics	7
2.4 Factors affecting PCO reactions	10
2.4.1 Irradiance	11
2.4.2 Temperature	11
2.4.3 Water Vapor.....	14
2.5 Photocatalyst Modification	15
2.5.1 Mixed Oxide Systems	15
2.5.2 Precious Metal Modified Photocatalysts.....	16
2.6 Oxidation of Propane	19
References	22
3 Photocatalytic oxidation of low molecular weight alkanes: Observations with ZrO₂-TiO₂ supported thin films	25
Abstract	25
3.1 Introduction	26
3.2 Experimental methods	28
3.2.1 Catalyst preparation	28
3.2.2 Apparatus	29
3.2.3 Experimental conditions	30

	vi
3.3 Results and Discussion.....	32
3.3.1 Photolysis and Catalysis	32
3.3.2 Optimizing Photocatalyst Packing and Illumination	33
3.3.3 Photocatalysis of Single Gases	35
3.3.4 Effect of Relative Humidity	36
3.3.5 Effect of Temperature	37
3.3.6 Complete Mineralization	38
3.3.7 A Tertiary Mixture	39
3.4 Conclusions	40
References	42
Figures	44
 4 Thermally assisted photocatalysis of propane using precious metal modified thin films	 56
Abstract	56
4.1 Introduction	57
4.2 Experimental Methods	60
4.2.1 Catalyst Preparation and Characterization	60
4.2.2 Apparatus	62
4.2.3 Experimental Conditions	63
4.3 Results and Discussion.....	64
4.3.1 Catalyst Characterization	64
4.3.2 Photocatalytic Results	66
4.3.3 Influence of Temperature on Irradiance	72
4.3.4 Photocatalytic Reaction Rates	73
References	77
Tables	80
Figures	81
 5 Platinized Photocatalytic Thin-Films: Relating Loading, Activity and Film Surface Potential	 90
Abstract	90
5.1 Introduction	91
5.2 Experimental Methods	93
5.2.1 Catalyst Preparation	93
5.2.2 Photocatalytic Testing	94
5.2.3 Surface Potential Imaging.....	96
5.3 Results and Discussion.....	98
5.3.1 Photocatalytic Oxidation	98
5.3.2 Surface Potential	99
5.4 Conclusion	104
References	106
Figures	109

6	Concluding Remarks and Suggestions for Future Research	116
6.1	Concluding Remarks	116
6.2	Suggestions for Future Work	117
Appendix A	Photoelectrochemical Studies	120
A.1	Materials and Methods.....	116
A.2	Results	117
A.3	Conclusion	126
	References	127
	Tables	128
	Figures	129
Appendix B	Lamp Irradiance	134
B.1	Materials and Methods.....	134
B.2	Results	135
B.3	Conclusion	136
	References	137
	Figures	138

List of Tables

Table 4.1	80
Parameter estimates obtained from non-linear regression analysis of kinetic data when fit to a first order LHHW model.	
Table A.1	128
Calculated flatband potentials extrapolated to pH 0 for thin film electrodes based on measurement of the photocurrent onset potential.	

List of Figures

Figure 2.1	7
Simplified diagram of the heterogeneous photocatalytic processes occurring in an illuminated TiO ₂ particle. 1) Activation 2) Bulk recombination, 3) Reduction of oxygen by e_{cb}^- , 4) Oxidation of water by h_{vb}^+ . (Adapted from [6])	
Figure 2.2	20
Proposed reaction pathway for photo-oxidation of propane to isopropyl alcohol to acetone via attack of reactive oxygen species. (Adapted from [7])	
Figure 3.1	44
Propane conversion at 70°C and 50% RH as a function of column diameter and number of rings: 1.5 cm i.d. – 102 rings (■), 2.5 cm i.d. – 102 rings (▽), 2.5 cm i.d. – 315 rings (○), 3.7 cm i.d. – 315 rings (●), 5.0 cm i.d. – 315 rings (△). Dotted lines represent the predicted conversion using the ½ order power law model. Data points are average value of 3 samples. Except where shown, error bars fall within the area of the series marker.	
Figure 3.2	45
Propane conversion versus linear velocity through the catalyst bed at constant space time. 2.5 cm i.d. (●), 3.7 cm i.d. (▲), 5.0 cm i.d. (○) Conditions: 70°C and 50% RH. Error bars for the 2.5 cm i.d. column are representative of 6 samples from 2 studies (catalyst was removed and repacked between studies – 3 samples per study). Error bars for the 3.7 cm i.d. and 5.0 cm i.d. are for 3 replicate samples from one study each.	
Figure 3.3	46
Schematic illustrating catalyst illumination in tubular reactor and the influence of end illumination as reactor diameter increases for a constant number of photocatalyst coated rings. 1) Photocatalyst bed, 2) UV light sources, 3) Glass column reactor: a) 2.5 cm i.d. b) 5.0 cm i.d., 4) Temperature wells. (Drawing not to scale).	

Figure 3.4	47
Single gas conversions versus space time @ 70°C and 30% RH. Propane (●), Isobutane (□), n-butane (▲). Data points are average value of 3 samples.	
Figure 3.5	48
Reaction rate constants ($\frac{1}{2}$ order power law model) for single gas experiments at 70°C as a function of relative humidity. Propane (●), Isobutane (□), n-butane (▲).	
Figure 3.6	49
Temperature effect on propane conversion in a dry feed stream. 35°C (●), 70°C (□) and 100°C (▼). Data points are average value of 3 samples.	
Figure 3.7a	50
Percent mineralization averaged over the humidity range tested (<2% – 60%) versus flowrate. (a) Propane: 70°C (●) and 100°C (○). Error bars represent the standard deviation of the averaged values.	
Figure 3.7b	51
Percent mineralization averaged over the humidity range tested (<2% – 60%) versus flowrate. (b) Isobutane: 70°C (■) and 100°C (□). Error bars represent the standard deviation of the averaged values.	
Figure 3.7c	52
Percent mineralization averaged over the humidity range tested (<2% – 60%) versus flowrate. (c) n-butane 70°C (▲) and 100°C (△). Error bars represent the standard deviation of the averaged values.	
Figure 3.8	53
Effect of relative humidity on percent mineralization of single gases. 70°C and 150 mL/min. Propane (●), Isobutane (□), n-butane (▲). Data points are average value of 3 samples.	
Figure 3.9	54
Acetone generation from photocatalysis of isobutane and propane single gas experiments at 70°C. Isobutane: 200 mL/min (□), 100 mL/min (■). Propane: 200 mL/min (○) and 100 mL/min (●). Acetone was not detected in PCO studies of n-butane. Data points are average value of 3 samples.	

Figure 3.10	55
Fractional conversion of gas components in a tertiary mixture consisting of 338 ppmv propane, 297 ppmv isobutane and 325 ppmv n-butane. 70°C and 30% RH. Propane (●), Isobutane (□), n-butane (▲). Data points are average value of 3 samples.	
Figure 4.1	81
BET surface area of the catalyst materials. Numbers correspond to modification of the photocatalyst listed on the abscissa with a given metal. 1 – unmodified, 2 – Ag, 3 – Au, 4 – Pd, 5 – Pt, 6 – Rh, 7 – Ru. ($n=1$, i.e. single sample)	
Figure 4.2	82
BJH pore size of the catalyst materials. Numbers correspond to modification of the photocatalyst listed on the abscissa with a given metal. 1 – unmodified, 2 – Ag, 3 – Au, 4 – Pd, 5 – Pt, 6 – Rh, 7 – Ru. ($n=1$, i.e. single sample)	
Figure 4.3	83
XRD patterns of TiO ₂ , SiO ₂ /TiO ₂ and ZrO ₂ /TiO ₂ powders from sintered xerogels. A – indicates the (101) anatase reflection and R – indicates the (110) rutile peak.	
Figure 4.4	84
Fractional conversion of propane at 50% RH and reactor temperatures of 50°C (■), 75°C (▒), and 100°C (□). Error bars represent the 95% confidence level.	
Figure 4.5	85
Mineralization ratios for conversion of propane at 50% RH and reactor temperatures of 50°C (■), 75°C (▒), and 100°C (□). The MR for Ru-T and Ru-ST was 0.0. The theoretical mineralization ratio for propane is 3 as indicated by the dotted line. Error bars represent the 95% confidence level.	
Figure 4.6	86
Effluent concentration of acetone during photocatalytic oxidation of 1000 ppmv (80 μmol·L ⁻¹) propane at 50% RH and reactor temperatures of 50°C (■), 75°C (▒), and 100°C (□). Error bars represent the 95% confidence level.	
Figure 4.7	87
Effluent concentration of acetone during photocatalytic oxidation of 1000 ppmv (80 μmol·L ⁻¹) propane at 50% RH and reactor temperatures of 50°C (■), 75°C (▒), and 100°C (□). Error bars represent the 95% confidence level.	

Figure 4.8	88
Dependence of propane oxidation on UV irradiance and reactor temperature, 1000 ppm propane and 50% RH. 35°C (●), 50°C (○), 75°C (▼), and 100°C (△). Solid black line is the linear least squares fit of the combined data. Slope = 0.94, $R^2 = 0.95$. Dashed lines are the linear least squares fit of the individual data sets. X-error bars are based on an average of 8 irradiance measurements in the reactor. Y-error bars are based on an average of three replicates analyses.	
Figure 4.9	89
Pseudo-first order reaction rate constants for propane oxidation adjusted for irradiance according to Equation 1. $\alpha = 0.94$. 50% RH and reactor temperatures of 50°C (■), 75°C (▣), and 100°C (□). Error bars are based on propagation of the measurement uncertainties calculated for I, W, and f_a .	
Figure 5.1	109
Experimental setup of the AFM-SP system. (drawing not to scale)	
Figure 5.2	110
Time course of propane effluent concentration from the single pass photoreactor experiments, with superimposed reactor temperature (right-hand side). 1000 ppmv C_3H_8 at inlet to reactor with 50% RH. (●) ZrO_2/TiO_2 , (■) 0.001%Pt, (△) 0.01%Pt, (▼) 0.1%Pt, and (○) 1%Pt. ----- Reactor Temperature.	
Figure 5.3	111
Time course of CO_2 effluent concentration from the single pass photoreactor experiments, with superimposed reactor temperature (right-hand side). 1000 ppmv C_3H_8 at inlet to reactor with 50% RH. (●) ZrO_2/TiO_2 , (■) 0.001%Pt, (△) 0.01%Pt, (▼) 0.1%Pt, and (○) 1%Pt. ----- Reactor Temperature.	
Figure 5.4	112
a) Topography and surface potential image of ZrO_2/TiO_2 thin film under dark and illuminated conditions. Scan proceeded from top to bottom beginning with dark conditions. UV-LEDs as light source with a measured surface irradiance of $14\text{ mW}\cdot\text{cm}^{-2}$. b) Section analysis depicting the average height profile (bottom curve – left axis) and average potential profile (top curve – right axis). The area profiled is designated by the box in the topography image in Figure 5.4a. Left to right in the profile graph corresponds to top to bottom in the images, centered about the dashed line in the box. The average along the width of each scan line in the box is plotted.	

Figure 5.5	113
Measured surface potential change of $\text{ZrO}_2/\text{TiO}_2$ and platinum loaded $\text{ZrO}_2/\text{TiO}_2$ thin films (and a control - the <i>substrate</i>) between dark and illuminated conditions upon exposure to UV-LEDs, with measured surface irradiance of $14 \text{ mW}\cdot\text{cm}^{-2}$. Surface potentials are averages of two replicate experiments.	
Figure 5.6	114
Measured surface potential change of $\text{ZrO}_2/\text{TiO}_2$ and platinum loaded $\text{ZrO}_2/\text{TiO}_2$ thin films between dark and illuminated conditions upon exposure to the UV fiber guide as the UV source with measured surface irradiance of approximately $45 \text{ mW}\cdot\text{cm}^{-2}$. Surface potentials are based on single measurements i.e., $n = 1$.	
Figure 5.7	115
Surface potential section analyses depicting potential decay associated with on – off transitions of the illumination source during the timecourse (proceeding left to right) of a scan for the $\text{ZrO}_2/\text{TiO}_2$ sample. Arabic numbers located next to the potential curves indicate switching on or off of the illumination source as listed below. a) UV-LED illuminated with measured surface irradiance of $14 \text{ mW}\cdot\text{cm}^{-2}$. 1 – On, 2 – Off, 3 – On, 4 – Off b) UV fiber guide illuminated with measured surface irradiance of $45 \text{ mW}\cdot\text{cm}^{-2}$. 5 – Off.	
Figure A.1a	129
Current density versus applied potential for TiO_2 -based thin film electrodes at pH 2. $10 \text{ mV}\cdot\text{sec}^{-1}$ scan rate starting at -1000 mV and progressing to 1000 mV . (Δ) TiO_2 , (\square) Ag-T, (\circ) Au-T, (\times) Pd-T, (\blacksquare) Pt-T, (\bullet) Rh-T, (\blacktriangle) Ru-T.	
Figure A.1b	130
Current density versus applied potential for $\text{SiO}_2\text{-TiO}_2$ -based thin film electrodes at pH 2. $10 \text{ mV}\cdot\text{sec}^{-1}$ scan rate starting at -1000 mV and progressing to 1000 mV . (Δ) S/T, (\square) Ag-S/T, (\circ) Au-S/T, (\times) Pd-S/T, (\blacksquare) Pt-S/T, (\bullet) Rh-S/T, (\blacktriangle) Ru-S/T.	
Figure A.1c	131
Current density versus applied potential for $\text{ZrO}_2\text{-TiO}_2$ -based thin film electrodes at pH 2. $10 \text{ mV}\cdot\text{sec}^{-1}$ scan rate starting at -1000 mV and progressing to 1000 mV . (Δ) Z/T, (\square) Ag-Z/T, (\circ) Au-Z/T, (\times) Pd-Z/T, (\blacksquare) Pt-Z/T, (\bullet) Rh-Z/T, (\blacktriangle) Ru-Z/T.	

Figure A.2a	132
Current density versus applied potential for TiO ₂ -based thin film electrodes at pH 6. 10 mV-sec ⁻¹ scan rate starting at -1000 mV and progressing to 1000 mV. (△) TiO ₂ , (□) Ag-T, (○) Au-T, (x) Pd-T, (■) Pt-T, (●) Rh-T, (▲) Ru-T.	
Figure A.2b	133
Current density versus applied potential for TiO ₂ -based thin film electrodes at pH 12. 10 mV-sec ⁻¹ scan rate starting at -1000 mV and progressing to 1000 mV. (△) TiO ₂ , (□) Ag-T, (○) Au-T, (x) Pd-T, (■) Pt-T, (●) Rh-T, (▲) Ru-T.	
Figure B.1	138
Irradiance (or intensity) (mW cm ⁻²) of several lamp-ballast combinations. □—magnetic ballast, ■—electronic ballast. [Average irradiance as plotted is the irradiance at the lamp's center position and an average of the replicate lamps of each lamp type and for the replicate (x 2) experiments.]	
Figure B.2	139
Irradiance (mW cm ⁻²) of several lamp-ballast combinations. □—magnetic ballast, ■—electronic ballast. [Average irradiance as plotted is an average of all five measurement locations of each lamp and for replicate experiments (x 2) of each lamp.]	
Figure B.3	140
Fractional conversion versus space time for two lamp-ballast ensembles – WIKO F8T5BLB-magnetic ballast combination (Ch. 3 herein) and F8T5-350BL-electronic ballast combination (Ch. 4 and 5). [Experimental conditions were 1000 ppmv C ₃ H ₈ , 50% RH and 35 °C.]	

Nomenclature

α	power of light irradiance
ϕ	work function
λ	wavelength
θ_A	surface coverage of species A
r_A	rate of reaction of species A
f_A	fractional conversion of species A
C_A	concentration of species A
C_{AO}	initial concentration of species A
C_{in}	concentration in
C_{out}	concentration out
n	reaction order
n	number of replicates
k_A	reaction rate constant for species A
K_A	adsorption equilibrium constant for species A
F_{Ao}	molar flowrate of species A
W	catalyst mass
I	light irradiance
E_F	Fermi energy
eV	electron volt
N_R	Reynolds number
e_{cb}^-	excited electron in conduction band

h_{vb}^+ positive hole in valence band

E_{fb} flatband potential

E_{fb}° flatband potential at pH 0

E_{oc} open circuit potential

ASHRAE American Society of Heating, Refrigerating and Air-Conditioning Engineers

AFM atomic force microscope

AFM-SP atomic force microscope – surface potential

BET Braunauer-Emmett-Teller

BJH Barrett, Johner, and Halenda

BL blacklight

BLB blacklight-blue

CB conduction band

CFC chlorofluorocarbon

FID flame ionization detector

FTIR Fourier transform infrared

GC gas chromatograph

IEP isoelectric point

IPA isopropyl alcohol

LED light emitting diode

LHHW Langmuir-Hinshelwood-Hougen-Watson

LSV linear sweep voltammetry

MFC	mass flow controller
MR	mineralization ratio
PAR	Princeton Applied Research
PCO	photocatalytic oxidation
PEC	photoelectrochemical
PFR	plug flow reactor
ppmv	parts per million (by volume)
RH	relative humidity
SCE	saturated calomel electrode
SP	surface potential
TCD	thermal conductivity detector
UV	ultra violet
VB	valence band
VOC	volatile organic compound
XRD	x-ray diffraction

Chapter 1

Introduction

The development of gas phase photocatalytic treatment processes for destruction of volatile organic compounds (VOCs) is a burgeoning field of research. Photocatalysis is an attractive treatment alternative because of several unique attributes: 1) organic contaminants are readily destroyed (or oxidized) instead of being merely transferred from one phase to another as present in adsorption processes; 2) mineralization (complete oxidation to CO₂ and H₂O) of a wide array of organic pollutants has been demonstrated; 3) reactions may occur at near ambient temperatures; 4) it may be possible to utilize solar energy to initiate photocatalytic reactions; 5) the growing cost of petroleum based fuels used for thermal treatment alternatives (e.g., incineration and catalytic oxidation) engenders conditions in which photocatalytic oxidation is an attractive treatment alternative. Photocatalysis has been applied to many niche applications for VOC treatment (e.g. ethylene control in fruit storage), but large-scale application for treating emissions from manufacturing processes are rare and under developed.

Despite the many positive features, photocatalytic oxidation (PCO) rates are often slow, which can make implementation to large scale treatment applications cost prohibitive. On the other hand, photocatalytic systems are well suited to the low VOC concentrations (<1000 ppmv) and high volumetric flow rates (30 – 70 m³-min⁻¹) that often characterize the effluent gas stream of manufacturing facilities. In situations where contaminants are

not effectively or efficiently treated through adsorption or thermal processes, photocatalysis may be a viable alternative.

As an example, a light alkane mixture of isobutane, n-butane and propane has been commercially used as a propellant in aerosol spray cans since the ban of chlorofluorocarbons (CFCs) in 1978. The characteristics of high vapor pressure and high chemical stability make short-chained alkanes good CFC substitutes. These characteristics also make short-chained alkanes very inert and a challenge to photocatalytically oxidize. The research described in this dissertation was performed in an effort to characterize the reactivity of photocatalytic thin films for complete mineralization of light alkanes. Furthermore, we evaluated means to improve the PCO reactivity and mineralization of these compounds.

The following chapters detail the evaluation of photocatalytic thin films for alkane destruction and research aimed at improving the reactivity and degree of mineralization in a bench-top reactor. Chapter 2 presents a brief literature review of photocatalysis and the factors that affect photocatalytic reactions. Methods reported in the literature to improve reactivity and mineralization of gas phase reactions are also summarized.

Chapter 3 presents an evaluation of the PCO of isobutane, n-butane and propane over $\text{ZrO}_2/\text{TiO}_2$ thin films in a packed bed reactor. Results indicate that humidity does not have a significant influence on the photocatalytic reaction rate. However, humidity does greatly affect the generation of intermediate reaction products. Increases in reactor temperature, as measured by thermocouple probes mounted on the external surface of the reactor, resulted in improved reactivity as the temperature was increased from 30°C to 70°C, but no distinct difference was noticeable between 70°C and 100°C. PCO of propane displayed the slowest

reaction rate in single gas studies and it was the slowest to degrade in tertiary mixtures.

Subsequent studies detailed in chapters 4 and 5 focus on improving the PCO of propane since it is the least reactive of the three alkanes studied in Chapter 3.

Chapter 4 discusses the study of TiO_2 , $\text{ZrO}_2/\text{TiO}_2$ and $\text{SiO}_2/\text{TiO}_2$ thin films and precious metal loaded variants of the films in an attempt to improve reaction rates and mineralization of propane at temperatures between 35°C and 100°C . A suite of six precious metals (Ag, Au, Pd, Pt, Rh, and Ru) individually deposited on the photocatalyst films at a loading of 1 wt % was tested. Results indicate that at a 1 wt % loading the metals had an adverse affect on the rate of photocatalytic activity, but in some cases did positively influence mineralization.

The observations presented in Chapter 4 suggest that platinum is the most reactive of the metals tested for oxidation of propane, but a loading of 1 wt % may not be optimal for the thin films. Chapter 5 presents the PCO results for systems wherein platinum is loaded into $\text{ZrO}_2/\text{TiO}_2$ thin films at levels of 0.001, 0.01, 0.1 and 1 wt %. The thin films were evaluated in the PCO of propane and characterized by traditional methods such as Brauner-Emmett-Teller (BET) surface area and x-ray diffraction (XRD), as well as a novel approach using atomic force microscopy surface potential (AFM-SP) measurement to evaluate the change in electrostatic potential of the films upon illumination. PCO results indicate $\text{ZrO}_2/\text{TiO}_2$ was the best material tested for photocatalytic degradation of propane, regardless of Pt content.

Chapter 6 offers concluding remarks and discusses proposals for future research. Recommendations for follow-up work address issues for making implementation of PCO more feasible. There is also a brief discussion for further development of the AFM-SP

analysis method for evaluation and comparison of the photocatalytic activity of thin film coatings.

Chapter 2

Literature Review

2.1 Photocatalysis

Photocatalysis is a process in which photons of sufficient energy activate a semiconductor thereby catalyzing a thermodynamically unfavorable reaction. Titanium dioxide (TiO_2) is the most prominent and widely used semiconductor in the field of photocatalysis. Titania has several appealing qualities that make it an almost ideal photocatalyst. 1) It is photoactivated by near UV (300-380 nm) illumination, which allows one to employ artificial (UV lamps) as well as solar (sun) sources; 2) it is almost chemically inert as well as stable and therefore safe for many applications; 3) a wide array of compounds may undergo selective or complete oxidation/reduction reactions on TiO_2 ; 4) it operates at near ambient temperatures [1,2]. Additionally, titania is commercially available or can easily be synthesized using a variety of methods (thermal hydrolysis, chemical vapor deposition, sputtering, sol-gel, etc.). The versatility of TiO_2 has led to numerous applications discussed in thousands of literature citations over the last 20 years [3].

2.2 Mechanisms of Photocatalysis

The energy band model for a semiconductor describes the valence band (VB) as the occupied energy bands and the conduction band (CB) as a collection of unfilled energy states. The VB and CB are separated by an energy gap of forbidden energy

states called the bandgap. The band gap of the anatase phase of titania is approximately 3.2 eV which corresponds to UV light with $\lambda \leq 380$ nm.

When an incident photon of sufficient energy is absorbed by the semiconductor, an electron (e_{cb}^-) is excited from the VB up to the CB, leaving behind a positively charged hole (h_{vb}^+). The h_{vb}^+ and e_{cb}^- can recombine in as little as ~10 nsec [4] in the catalyst bulk or on the surface giving off heat; or these charge carriers may be trapped in surface states where they can mediate oxidation and reduction reactions, respectively. Figure 2.1 illustrates the major processes that may occur in illuminated TiO_2 .

In aqueous systems, hydroxyl radicals and surface trapped holes are credited as the active species in oxidation of organics [4-6]. In gaseous systems, water vapor can react with holes to form hydroxyl radicals (Figure 2.1, step 4), which in turn can oxidize organic compounds. Some researchers also suggest that the activated surface adsorbed oxygen ($\text{O}_2^{\cdot-}$, O^- , etc.) (Figure 2.1, step 3) may be the active species for organic destruction, especially in gas phase reactions [7,8]. Universal agreement on the active species or mechanism in gas phase photocatalytic reactions has yet to be reached.

Charge carrier recombination (Step 2 in Figure 2.1) is the main detriment to oxidizing adsorbed species. Therefore, alterations to a photocatalyst that improve charge separation and/or interfacial charge transfer should improve photocatalytic efficiencies.

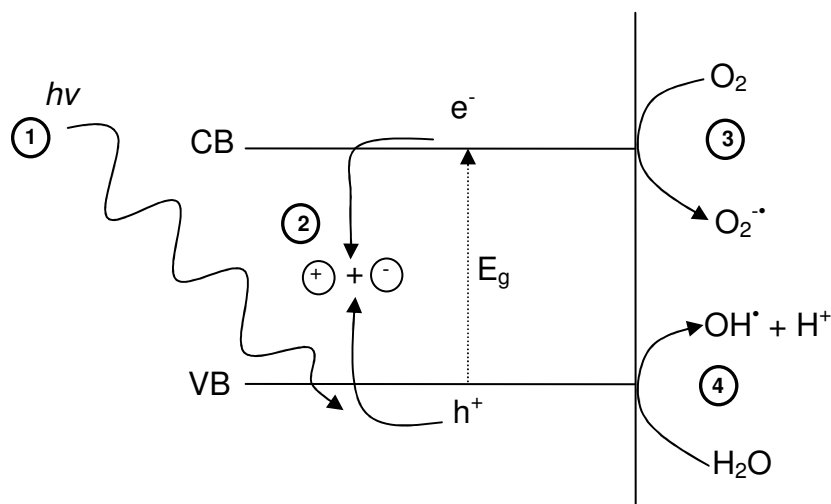


Figure 2.1: Simplified diagram of the heterogeneous photocatalytic processes occurring in an illuminated TiO_2 particle. 1) activation 2) bulk recombination, 3) reduction of oxygen by e_{cb}^- , 4) oxidation of water by h_{vb}^+ . (Adapted from [6])

2.3 Reaction Kinetics

Modeling the reaction kinetics of heterogeneous PCO reactions has been the focus of a considerable body of research [9-15]. Kinetic data for these reactions aid in evaluating the pertinent factors affecting PCO reactions. Kinetic analysis of laboratory studies is also crucial to the design and scale-up of industrial reactors employing photocatalysts.

The design for an end-of-pipe treatment system for gaseous emissions would likely consist of a single-pass reactor. Single pass reactors have been successfully modeled using plug flow reactor (PFR) models. Plug flow reactor models utilize the following simplifying assumptions: 1) No radial mixing 2) No translational diffusion along the direction of flow, 3) Complete mixing in the plug [16]. While these

assumptions may not accurately reflect the true conditions in a single-pass reactor, PFR models often provide an acceptable simulation of the experimental data. Models using power law rate expressions and Langmuir-Hinshelwood-Hougen-Watson (LHHW) rate expressions have both successfully fit kinetic data from single-pass gas phase PCO reactors [11,14,17,18].

The following paragraphs briefly describe the design and kinetic equations typically used to model PFRs. For a more detailed discussion, the reader is referred to “Evaluation of Photocatalysis for Gas-Phase Air Cleaning—Part 1: Process, Technical, and Sizing Considerations,” ASHRAE Transactions, Volume 111, Part 2.

The reactor design equation for a plug flow reactor can be expressed as [19]:

$$\frac{W}{F_{A0}} = \int_{f_{A,in}}^{f_{A,out}} \frac{df_A}{-r_A} \quad (2.1)$$

In Eq. 2.1, $-r_A$ is the rate of disappearance of species A, W is the mass of the catalyst, F_{A0} is the molar flow rate of reactant A entering the reactor, and f_A is the fractional conversion of reactant A. Fractional conversion may be expressed as:

$$f_A = 1 - \left(\frac{C_A}{C_{A0}} \right) \quad (2.2)$$

where C_{A0} equals the initial contaminant concentration. Taking the derivative of Eq. 2.1 and rearranging leads to an expression in differential form

$$\frac{df_A}{d\left(\frac{W}{F_{A0}}\right)} = -r_A \quad (2.3)$$

Substitution for f_A using Eq. 2.2 yields:

$$\frac{dC_A}{d\left(\frac{W}{F_{Ao}}\right)} = r_A C_{Ao} \quad (2.4)$$

Initial estimates of reaction rate constants (and equilibrium adsorption constants for LHHW models) may be calculated from linear regression after substituting an appropriate rate expression into Eq. 2.1. These initial estimates combined with Eq. 2.4 allow for nonlinear regression analysis using Athena Visual Workbench® software (Athena Visual Software, Inc.) for process modeling, nonlinear parameter estimation and optimization.

The power law model uses the following rate equation

$$r_A = k_A C_A^n \quad \text{Eq. (2.5)}$$

where r_A is the reaction rate (in units of $\text{mol} \cdot \text{g}^{-1} \cdot \text{s}^{-1}$), k_A is the reaction rate constant (units depend on the reaction order, n), C_A is the contaminant effluent concentration ($\text{mol} \cdot \text{l}^{-1}$) and $n = 0.5, 1, 1.5$ and 2 . Power law kinetic models can arise as limiting forms of LHHW rate expressions.

Because PCO reactors involve interactions between the gas-phase contaminants and the surface of the photocatalyst, LHHW rate expressions are expected to provide a good approximation for the overall kinetics of these reactions. The LHHW models of photocatalytic reactions are based on a mechanism that involves a reactant adsorbed on the surface of a catalyst. A simple LHHW rate expression for a reaction that is first order - with respect to the fraction of the surface covered by adsorbed species A (θ_A) - can be written as

$$-r_A = k_A \theta_A = \frac{k_A K_A C_A}{1 + K_A C_A} \quad (2.6)$$

For this equation, the rate constant k_A has units of $\text{mol}\cdot\text{g}^{-1}\cdot\text{s}^{-1}$. The adsorption equilibrium constant for adsorbate A (K_A) has units of reciprocal concentration (e.g., $\text{l}\cdot\text{mol}^{-1}$). According to LHHW theory, reactants may compete to adsorb on the photocatalyst surface on the same type of surface site, or be adsorbed on different types of surface sites with or without competition. These possibilities lead to more complex forms of the rate expression. More complex forms of the LHHW rate expression are not considered herein.

2.4 Factors Affecting PCO Reactions

The effectiveness of the photocatalytic process to degrade a given compound can vary greatly depending on the target compound, catalyst properties and reactor operating conditions. Reaction rates, end-products and catalyst activity as well as catalyst lifetime may be influenced by the reaction temperature, water vapor concentration, catalyst formulation, reactor design and possibly many other factors. The discussion that follows is not all inclusive, but it does cover the most pertinent variables that apply to this work.

2.4.1 Irradiance

Photocatalysis requires the input of photons to activate the semiconductor. Therefore, the irradiance in a PCO reactor can drastically affect the effectiveness of the reaction. Photocatalytic reactions are commonly grouped into two categories: light rich and light poor. Light-rich systems are defined as having irradiance greater than 20 mW-cm⁻² [1,20-22]. For these systems the reaction rate has a half-order dependence on the irradiance. This dependence is a result of the increase in electron-hole recombination at higher intensities being the rate dominating process [21]. Light-poor systems follow a first-order dependence that is attributed to dominance of the surface-contaminant reaction.

The relationship between irradiance and the PCO reaction rate can be expressed according to Eq. 2.7.

$$k_a = k'_a I^\alpha \quad (2.7)$$

where k_a is the observed reaction rate constant, k'_a is the reaction rate constant, I is irradiance (mW-cm⁻²) and α is the exponential factor. A logarithmic transform of Eq. 2.7 yields:

$$\ln k_a = \ln k'_a + \alpha \ln I \quad (2.8)$$

A plot of $\ln k_a$ vs $\ln I$ should yield a straight line with a slope of α .

2.4.2 Temperature

Because photocatalysis is activated by photons, photocatalytic reactions can operate at room temperature and are relatively insensitive to temperature changes [5]. The peer-reviewed literature reports that reaction rates are typically the highest for

reactor temperatures between 20°C and 80°C, with reaction rates generally decreasing at temperatures above 80°C [23].

Water adsorbed on the photocatalyst has been reported extensively to play a critical role in the surface-mediated photocatalytic reactions, trapping valence band holes and forming hydroxyl radicals [4]. As reactor temperatures exceed 80°C and approach the boiling point of water, the loss of water on the surface may limit the photocatalytic reaction [23]. Likewise, the surface adsorption-desorption equilibrium of target compounds and intermediates may shift towards the gas phase at elevated temperatures thereby reducing the interaction of gas molecules with the photocatalytic surface. On the other hand, the change in surface coverage of the reactants and intermediates at elevated temperatures may make more surface sites available for the desired reactions. Furthermore, conventional heterogeneous catalytic reactions may occur at elevated temperatures depending on the reacting species and the catalyst. Thus, the effect of temperature on a given photocatalytic reaction will be highly dependent on the contaminant, catalyst and other compounds present at the catalyst surface (e.g. water, intermediates or end reaction products).

Despite the suggested insensitivity of PCO reactions to temperature changes, many studies of the photocatalytic treatment of volatile organic compounds (VOCs) have reported a beneficial effect of increasing reaction temperature. In the case of ethylene oxidation at temperatures ranging from 40 – 110°C, the desorption of water from the catalyst surface appears to free up additional reactive sites for reaction with ethylene [17]. PCO of benzene demonstrates a similar response to increases in

temperature with the amount of benzene converted to CO_2 significantly higher at temperatures up to 110°C [24]. Photocatalytic treatment of acetone was found to have an optimum rate at 100°C [12], with the peak reaction rate significantly affected by the relative humidity in the reactor. Conversion of a 6400-ppmv ethanol feed stream in a TiO_2 single-pass annular reactor had a maximum of nearly 100% conversion at $\sim 100^\circ\text{C}$, but minimal mineralization ($\sim 20\%$) [25]. Complete mineralization of trichloroethylene was observed at a temperature of 64°C while monochloroacetic acid was formed at 23°C . Recently, Haaglund et al. [26] observed an optimal reaction condition of 130°C and 1% water content for conversion of 0.1% propane in a glass plate single pass reactor. Finally, Kim et al. reported a decrease in the photocatalysis of TCE, acetone, methanol and toluene above temperatures of 45°C [27]. The decrease in performance was attributed to poorer VOC adsorption on the catalyst surface coupled with a decrease in irradiance at high temperatures.

These observations result in a conundrum facing designers of photocatalytic reactors for treating industrial VOC emissions. Typical UV lamps have an optimal operating temperature near 35°C , with lamp irradiance decreasing above and below the optimal temperature [28]. Sufficient illumination of the photocatalyst is essential to optimizing a PCO reactor; therefore, a large bank of UV lamps will likely be required. Approximately 80% of the energy used to power a fluorescent UV lamp is lost as heat [17]. Therefore, in a commercial-scale PCO treatment device employing dozens to hundreds of lamps, the photocatalytic reactor could very well operate at temperatures in excess of 80°C depending on reactor design. Consequently, design of a PCO reactor

must aim to optimize the reaction temperature for the desired reaction while also considering the influence of lamp irradiance on the photocatalytic reactions.

2.4.3 Water Vapor

The results of studies by Haaglund et al. [26], Kennedy and Datye [25], and Kim et al. [29], among other investigators, suggest the presence of a complex relationship between the contaminant, relative humidity (RH) and temperature in a PCO reactor. As depicted in Step 4 of Figure 2.1, water adsorbed on the photocatalyst surface is oxidized by a valence-band hole to produce hydroxyl radicals. The continuous consumption of these radicals requires replenishment of the adsorbed water [10]. Coronado et al. demonstrated that only low RH (ca. 10%) is required to begin the formation of a physisorbed monolayer of water on the surface of a thin film TiO_2 with completion of the monolayer occurring at ~57% RH [9]. Thus, as surface coverage increases at higher water vapor concentrations, competitive adsorption for reactive sites on the catalyst surface may decrease reaction rates [30].

Investigations into the effects of relative humidity on the PCO of VOCs often show conflicting results and no readily discernable trend is evident, which is likely due to differences in the chemical and physical properties of the contaminants and catalyst materials. For example, the reactivity of acetone has been shown to increase [9,31] or decrease [27,29,32,33] as a result of increasing the concentration of water. Furthermore, investigations involving the PCO of ethylene [17,20] and heptane [34] suggest an inverse relationship between water vapor concentration and reaction rate, whereas

photocatalysis of hexane showed an initial increase in conversion up to 20% RH followed by a significant decrease in conversion at RH higher than 45% [14]. Additionally, the presence of water vapor in a photocatalytic system has been shown to affect the selectivity of the reaction [26].

2.5 Photocatalyst Modification

Attempts at improving photocatalytic reactions generally aim to modify the catalyst so as to (1) inhibit recombination by increasing the charge separation and improving the efficiency of the photocatalytic process; (2) increasing the wavelength response range (i.e. excitation of wide band gap semiconductors by visible light); and (3) changing the selectivity or yield of a particular product [6].

The following sections discuss methods of photocatalyst modification that have proven beneficial for impacting VOC oxidation. Increasing the wavelength response of photocatalysts will not be presented because utilization of solar light for a large scale single-pass photoreactor is unlikely due to design limitations and requirements such as 24-hr operation.

2.5.1 Mixed Oxide Systems

Mixed oxide systems typically consist of TiO_2 with small quantities (<20%) of a second metal oxide added. Addition of the second metal oxide affects several characteristics of the photocatalyst that in many cases has led to improved photocatalytic activity. The dissimilar boundaries between metal oxide particles slow the sintering

process resulting in higher surface areas and changes in crystalline structure. The substitution of one mixed oxide into the crystal structure of another is also suspected of causing a charge imbalance due to the difference in coordination of the cationic species [35]. Such a charge imbalance may lead to more surface acid sites in a binary oxide.

Fu et al. [36] demonstrated that mixing TiO_2 with ZrO_2 and SiO_2 improved photocatalytic rates by more than 2 times compared to plain TiO_2 . Small quantities (<16 wt %) of ZrO_2 and SiO_2 mixed into the TiO_2 matrix increased the surface area by a factor of 1.7 and 2.3, respectively, when fired at 350°C . Transformation of the TiO_2 from anatase to the rutile crystalline phase was also delayed in the mixed oxides leading to a photocatalyst with higher activity (anatase is generally regarded as the more active photocatalyst). Keller et al. [37] documented a 50% improvement in conversion of butyl acetate at room temperature using a WO_3/TiO_2 binary system compared to plain TiO_2 . Improvements in the photocatalytic activity were attributed to more surface hydroxyl groups resulting from higher surface acidity in the binary system.

2.5.2 Precious Metal Modified Photocatalysts

Metallization of the photocatalyst surface is the most common approach used to enhance the performance of the photocatalyst. Precious metals have been shown to improve charge carrier separation (mainly in aqueous systems) [6,38], but in gaseous systems the benefit of adding metals is typically conducted to produce a conventional catalytic effect [1]. In many cases, the optimal quantity of metal added to the photocatalyst ranges between (0.1 and 2%). Fermi level equilibration at the metal-

semiconductor interface can lead to formation of a space charge layer and a localized trapping of electrons at a metal island. At higher loadings, these metals may act as recombination centers because they are no longer localized, discrete particles, rather they are large centers that build up negative excess charge thereby attracting holes from the valence band [39]. Additionally, as the weight percent loading increases beyond an optimum (~3 wt %), the metal may block a significant portion of the photocatalyst from receiving illumination [40].

The thermal catalytic effect of many precious metals improves reactivity by direct oxidation of the target contaminant or oxidation of intermediate compounds. For example, in the case of ethanol, Kennedy and Datye [25] reported 100% conversion of ethanol and about 35% mineralization using 0.2%Pt-TiO₂ at reaction temperatures below 425 K (152°C). At temperatures > 425 K, ethanol mineralization quickly reached 100%. Ethanol conversion reached a high of ~95% using plain TiO₂, but mineralization did not exceed 20% regardless of temperature. Acetaldehyde is an intermediate of ethanol photooxidation over TiO₂ and when reaction temperatures exceeded 425 K the catalytic effect of platinum quickly oxidized the acetaldehyde [25]. Not surprisingly, Pt-modified TiO₂ has also improved photocatalytic reactions for acetaldehyde [41]. Likewise, the photocatalytic destruction of benzene [24] and ethylene [15] improved when Pt-modified TiO₂ was used at reaction temperatures greater than 100°C. However, 1% platinum addition to TiO₂ decreased the photooxidation of butyl acetate at both room temperature and 100°C compared to plain TiO₂ [37].

Gold and silver are other common surface modifiers for photocatalysts, but have mainly been used in aqueous systems. Due to its high activity at the nanoparticle level, gold has been investigated by many groups interested in photocatalytic reactions. For instance, Li and Li demonstrated a significant increase in photooxidation of methylene blue in aqueous systems using Au/Au³⁺-TiO₂ powder [42]. Gold-capped TiO₂ also improved the photooxidation of thiocyanate [43]. Chandrasekharan and Kamat recently demonstrated increased photocurrent generation by adsorbing gold nanoparticles onto a TiO₂-coated electrode [38].

Silver-TiO₂ studies have provided evidence that small quantities (<5 mol %) of silver readily trap charged electrons and reduce recombination in the degradation of rhodamine B solutions [44]. An optimum loading of 0.5 wt% Ag on TiO₂ enhanced decomposition of phenol [45]. Furthermore, silver-modification of a TiO₂ sol and characterization of the films revealed an increase of methylene blue degradation due to increased specific surface area, promotion of charge transfer, and enhancement of electron-hole pair separation [46].

Very little work with palladium-, rhodium- or ruthenium-modified photocatalysts has been documented in the literature. As with other precious metals, modifications with these have aimed to improve electron transfer for oxygen reduction in aqueous systems and to date, results using Pd, Rh and Ru have not been as promising as those using Pt, Ag, and Au [47]. However, Pd, Rh, and Ru are commonly used as thermal catalysts and reported evidence suggests (to be discussed in the following section) these metals could be beneficial adjuncts in gas-phase PCO of light alkanes [48].

2.6 Oxidation of Propane

The first systematic study of gas-phase heterogeneous photocatalysis over illuminated TiO₂ evaluated the partial oxidation of low molecular weight alkanes [7]. This study proposed a reaction pathway for the photooxidation of propane to acetone. As seen in Figure 2.2, an active oxygen species is suspected of initiating the reaction of propane to form isopropyl alcohol (IPA). IPA quickly converts to acetone through nucleophilic attack of another active oxygen species. An alternative pathway involves the formation of a primary alcohol with subsequent formation of an aldehyde. Selectivity towards acetone in the photocatalysis of propane is more than five times the selectivity to acetaldehyde [7,49-51].

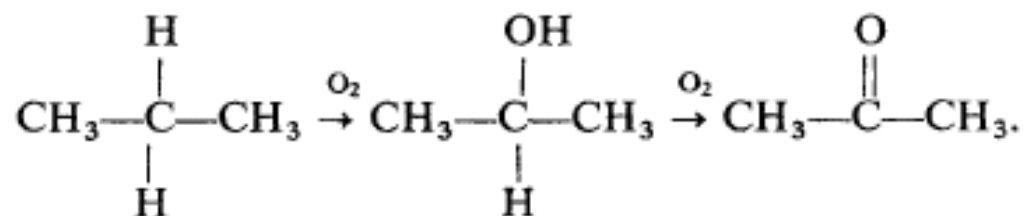


Figure 2.2: Proposed reaction pathway for photo-oxidation of propane to isopropyl alcohol to acetone via attack of reactive oxygen species. (Adapted from [7].)

Since Djeghri's seminal study [7], very few studies of the photocatalysis of propane have been performed. Tanaka's group at Kyoto University studied the selective photooxidation of light alkanes [49,50]. In their studies of TiO₂/SiO₂ and alkali-ion-modified vanadium oxide, a commercially available powder-based form of titania (Degussa P-25) was investigated. Their results indicate that titania has high selectivity

(~70%) to CO₂, and increasing the weight percent of SiO₂ increased acetone production. Brigden et al. demonstrated near complete photoconversion of 600 ppmv propane to CO₂ using high surface area TiO₂ (357 m²-g⁻¹) at conditions of 12% O₂ and 150°C [52]. More recently, Haaglund et al. studied the PCO of 0.1% (1000 ppmv) propane at varying temperatures and water vapor concentrations using Fourier Transform Infrared (FTIR) spectroscopy to detect both the disappearance of the reactants and to monitor the appearance of reaction intermediates and products. They confirmed the primary conversion of propane to acetone, but also suggested various reaction pathways where branching depends on the temperature and water coverage of the catalyst surface [26]. They reported that the optimal reaction condition for propane conversion is 130°C with 1% water vapor concentration.

Thermal catalytic oxidation of propane has also been pursued, primarily over Pt and Pd catalysts [53-56]. Typical light-off temperatures occur at 200°C or higher. A recent study of propane catalytic oxidation using 5 wt % Pt catalysts supported on seven different metal oxides indicated a relationship between the surface acidity of the support and catalytic activity [55]. Platinum deposited on the more acidic supports was capable of near complete oxidation of a 2500 ppmv propane feed stream at lower temperatures (~474 K) while platinum on less acidic supports required higher temperatures to achieve similar performance. The authors suggested that more acidic supports aid in preventing the oxidation of the platinum metal. Rodemerck et al. evaluated a plethora of titania supported precious metal catalysts for low-temperature catalytic oxidation of 0.1% propane. A genetic algorithm was used to determine the optimal mixture of a ternary catalyst with up to

3 wt % metal loading. They found 3 wt % ruthenium supported on TiO_2 to be the most active catalyst showing ca. 20, 25 and 75% propane conversion at 50, 100 and 150°C, respectively. Other catalysts showing activity for propane conversion included (in descending order of performance) Rh, Pt, Pd, Au, Cu, Ag and Mn [48].

In summary, the literature indicates that the addition of precious metals into thin-film photocatalysts with the intent of improving photocatalytic oxidation of propane has not been reported. Additionally, the recent work by Rodemerck et al. [48] suggests several precious metals may prove beneficial as additives.

References

- [1] O.Carp, C.L.Huisman, A.Reller, *Prog. Solid State Chem.* 32 (2004) 33-177.
- [2] J.Peral, X.Domenech, D.F.Ollis, *J. Chem. Technol. Biotechnol.* 70 (1997) 117-140.
- [3] D.M.Blake, in *National Renewable Energy Laboratory (Ed.), National Renewable Energy Laboratory, National Renewable Energy Laboratory, 2005.*
- [4] M.R.Hoffmann, S.T.Martin, W.Y.Choi, D.W.Bahnemann, *Chem. Rev.* 95 (1995) 69-96.
- [5] M.A.Fox, M.T.Dulay, *Chem. Rev.* 93 (1993) 341.
- [6] A.L.Linsebigler, G.Lu, J.T.J.Yates, *Chem. Rev.* 95 (1995) 735.
- [7] N.Djeghri, M.Formenti, F.Juillet, S.J.Teichner, *Faraday Discuss.* (1974) 185-193.
- [8] Y.C.Liu, G.L.Griffin, S.S.Chan, I.E.Wachs, *J. Catal.* 94 (1985) 108-119.
- [9] J.M.Coronado, M.E.Zorn, I.Tejedor-Tejedor, M.A.Anderson, *Appl. Catal. B* 43 (2003) 329-344.
- [10] T.N.Obee, R.T.Brown, *Environ. Sci. Technol.* 29 (1995) 1223-1231.
- [11] A.Sirisuk, C.G.Hill, M.A.Anderson, *Catal. Today* 54 (1999) 159-164.
- [12] A.V.Vorontsov, E.N.Kurkin, E.N.Savinov, *J. Catal.* 186 (1999) 318-324.
- [13] S.Yamazaki, S.Tanaka, H.Tsukamoto, *J. Photochem. Photobiol. A* 121 (1999) 55-61.
- [14] P.Y.Zhang, J.Liu, *J. Photochem. Photobiol. A* 167 (2004) 87-94.
- [15] M.E.Zorn, D.T.Tompkins, W.A.Zeltner, M.A.Anderson, *Environ. Sci. Technol.* 34 (2000) 5206-5210.
- [16] O.Levenspiel, *Chemical Reaction Engineering*, Second ed., John Wiley & Sons, Inc., New York, 1972.
- [17] X.Z.Fu, L.A.Clark, W.A.Zeltner, M.A.Anderson, *J. Photochem. Photobiol. A* 97 (1996) 181-186.
- [18] M.E.Zorn, D.T.Tompkins, W.A.Zeltner, M.A.Anderson, *Appl. Catal. B* 23 (1999) 1-8.

- [19] C.G.Hill Jr., *An Introduction to Chemical Engineering Kinetics & Reactor Design*, Wiley, New York, 1977.
- [20] T.N.Obee, S.O.Hay, *Environ. Sci. Technol.* 31 (1997) 2034-2038.
- [21] D.F.Ollis, E.Pelizzetti, N.Serpone, *Environ. Sci. Technol.* 25 (1991) 1522-1529.
- [22] C.S.Turchi, D.F.Ollis, *J. Catal.* 122 (1990) 178-192.
- [23] J.M.Herrmann, *Catal. Today* 53 (1999) 115-129.
- [24] X.Fu, W.A.Zeltner, M.A.Anderson, 1995, pp. 209-224.
- [25] J.C.Kennedy, A.K.Datye, *J. Catal.* 179 (1998) 375-389.
- [26] C.Hagglund, B.Kasemo, L.Osterlund, *J. Phys. Chem. B* 109 (2005) 10886-10895.
- [27] S.B.Kim, S.C.Hong, *Appl. Catal. B* 35 (2002) 305-315.
- [28] Product Information Bulletin, T5 Linear Fluorescent Lamps, Osram Sylvania, 2006.
- [29] S.B.Kim, H.T.Hwang, S.C.Hong, *Chemosphere* 48 (2002) 437-444.
- [30] L.X.Cao, Z.Gao, S.L.Suib, T.N.Obee, S.O.Hay, J.D.Freihaut, *J. Catal.* 196 (2000) 253-261.
- [31] M.E.Zorn, D.T.Tompkins, W.A.Zeltner, M.A.Anderson, *Appl. Catal. B* 23 (1999) 1-8.
- [32] S.Hager, R.Bauer, *Chemosphere* 38 (1999) 1549-1559.
- [33] C.Raillard, V.Hequet, P.Le Cloirec, J.Legrand, *J. Photochem. Photobiol. A* 163 (2004) 425-431.
- [34] J.Shang, Y.G.Du, Z.L.Xu, *Chemosphere* 46 (2002) 93-99.
- [35] K.Tanabe, *Solid Acids and Bases*, Kodansha Scientific Books, Tokyo, 1970.
- [36] X.Z.Fu, L.A.Clark, Q.Yang, M.A.Anderson, *Environ. Sci. Technol.* 30 (1996) 647-653.
- [37] V.Keller, P.Bernhardt, F.Garin, *J. Catal.* 215 (2003) 129-138.
- [38] N.Chandrasekharan, P.V.Kamat, *J. Phys. Chem. B* 104 (2000) 10851-10857.
- [39] W.Mu, J.M.Herrmann, P.Pichat, *Catal. Lett.* 3 (1989) 73-84.

- [40] I.M.Arabatzis, T.Stergiopoulos, D.Andreeva, S.Kitova, S.G.Neophytides, P.Falaras, *J. Catal.* 220 (2003) 127-135.
- [41] T.Sano, N.Negishi, K.Uchino, J.Tanaka, S.Matsuzawa, K.Takeuchi, *J. Photochem. Photobiol. A* 160 (2003) 93-98.
- [42] F.B.Li, X.Z.Li, *Appl. Catal. A* 228 (2002) 15-27.
- [43] V.Subramanian, E.E.Wolf, P.V.Kamat, *Langmuir* 19 (2003) 469-474.
- [44] B.F.Xin, L.Q.Jing, Z.Y.Ren, B.Q.Wang, H.G.Fu, *J. Phys. Chem. B* 109 (2005) 2805-2809.
- [45] A.Dobosz, A.Sobczynski, *Water Res.* 37 (2003) 1489-1496.
- [46] C.He, Y.Yu, X.F.Hu, A.Larbot, *Appl. Surf. Sci.* 200 (2002) 239-247.
- [47] C.M.Wang, A.Heller, H.Gerischer, *J. Am. Chem. Soc.* 114 (1992) 5230-5234.
- [48] U.Rodemerck, D.Wolf, O.V.Buyevskaya, P.Claus, S.Senkan, M.Baerns, *Chem. Eng. J.* 82 (2001) 3-11.
- [49] T.Tanaka, T.Ito, S.Takenaka, T.Funabiki, S.Yoshida, *Catal. Today* 61 (2000) 109-115.
- [50] T.Tanaka, K.Teramura, T.Yamamoto, S.Takenaka, S.Yoshida, T.Funabiki, *J. Photochem. Photobiol. A* 148 (2002) 277-281.
- [51] K.Wada, K.Yoshida, T.Takatani, Y.Watanabe, *Appl. Catal. A* 99 (1993) 21-36.
- [52] C.T.Brigden, S.Poulston, M.V.Twigg, A.P.Walker, A.J.J.Wilkins, *Appl. Catal. B* 32 (2001) 63-71.
- [53] Y.Yazawa, H.Yoshida, N.Takagi, S.Komai, A.Satsuma, T.Hattori, *J. Catal.* 187 (1999) 15-23.
- [54] Y.Yazawa, N.Kagi, S.Komai, A.Satsuma, Y.Murakami, T.Hattori, *Catal. Lett.* 72 (2001) 157-160.
- [55] Y.Yazawa, N.Takagi, H.Yoshida, S.Komai, A.Satsuma, T.Tanaka, S.Yoshida, T.Hattori, *Appl. Catal. A* 233 (2002) 103-112.
- [56] L.Kiwi-Minsker, I.Yuranov, E.Slavinskaia, V.Zaikovskii, A.Renzen, *Catal. Today* 59 (2000) 61-68.

Chapter 3

Photocatalytic oxidation of low molecular weight alkanes: Observations with ZrO₂-TiO₂ supported thin films

Abstract

Low molecular weight alkanes including, propane, isobutane and n-butane can be completely oxidized to carbon dioxide and water vapor using a tubular photoreactor containing supported ZrO₂-TiO₂ thin film photocatalyst. It was observed that efficient reactor design requires optimization of catalyst packing to minimize bypass of the contaminant gas and optimization of the reactor diameter to maximize catalyst illumination. Single gas streams of ~1000 ppmv were fed into the optimized tubular reactor and evaluated for complete oxidation at relative humidity ranging from <2% to 60% and at reactor temperatures of 35, 70, and 100°C. The magnitude of reaction rate constants for isobutane and n-butane were comparable while on average the reaction rates of propane were significantly smaller. Reaction rates of propane and n-butane respond similarly to humidity levels, but isobutane reactivity differs in response to humidity. Reaction rates increase significantly from 35 to 70°C, but not from 70 to 100°C. In a feed stream containing a tertiary mixture of these alkanes and passed through the reactor, n-butane had the highest photoconversion followed by isobutane and propane. Variations in the gases' reactivity in single gas and tertiary

experiments were attributed to differences in strength of adsorption to the catalyst and reaction pathways that led to different intermediate compounds.

3.1 Introduction

In recent years, the use of gas phase photocatalytic oxidation (PCO) for the destruction of volatile organic compounds (VOC) has gained increased attention because of its potential application in such areas as environmental clean up (soil vapor extraction, air stripping, etc.), control of indoor air contaminants, and industrial end-of-pipe treatment. The attractiveness of gas phase PCO lies in its capacity to completely mineralize many organics to CO_2 and H_2O (and HCl for chlorinated compounds) at near ambient temperatures with atmospheric oxygen serving as the oxidant [1-3]. Studies of VOC treatment employing titania-based photocatalysts have investigated a myriad of compounds - alkanes, alkenes, alcohols, aromatic hydrocarbons, chlorinated hydrocarbons, ketones, aldehydes as well as other organic species.

Low molecular weight alkanes, despite being one of the first groups of gases studied in photocatalysis [4], have received comparatively little attention in contemporary work on heterogeneous PCO [5-7]. Research on low molecular weight alkanes has primarily focused on selective oxidation for the synthesis of intermediate compounds. Ketones and aldehydes are the primary intermediates [4], but complete oxidation has been documented [6,7]. Photocatalysis of light alkanes is exceptionally challenging because their strong C-C and C-H bonds are difficult to break. Additionally, their non-polarity is not conducive to gas-solid adsorption processes, a key component of gas phase photocatalysis [8]. Furthermore, alkanes

such as propane, n-butane and isobutane are generally inert and are of minimal environmental concern when compared to the impact of other VOCs on the environment.

Since the 1978 ban on the use of chlorofluorocarbons (CFCs), light alkanes (C_3 - C_6) with their low boiling point and stable nature have been recommended as substitutes for CFC-based propellants in aerosol cans [9]. However, VOCs including light alkanes have been linked to tropospheric ozone formation [10], leading to a need for abatement control technologies, especially in ozone non-attainment areas. Low VOC concentrations (<1000 ppmv) and high flow volume often characterize the effluent gas stream of manufacturing facilities; thus, thermal and catalytic oxidation of these species is costly [2], while low adsorptivity hinders their removal using adsorption processes. Despite the high stability and low adsorptivity of light alkanes, PCO holds the potential to provide a relatively cheap and effective means of treatment.

The purpose of this paper is to assess the photocatalytic activity of three common aerosol propellants (isobutane, n-butane and propane) using supported ZrO_2 - TiO_2 photocatalyst thin films in single gas and tertiary mixtures. Optimizing the plug-flow reactor as a function of support packing and catalyst illumination is also presented. Photocatalytic experiments performed at varying relative humidities and temperatures allowed for identification of operating conditions that were more favorable for the complete oxidation of the target compounds. Comparisons in the reactivity of the different alkanes were drawn from kinetic analyses using two common kinetic models: a general power law model and a Langmuir-Hinshelwood-Hougen-Watson model.

3.2 Experimental Methods

3.2.1 Catalyst Preparation

The mixed-oxide catalyst material used in this study was prepared using a sol-gel method [11] in which titania and zirconia sols were prepared separately prior to combining. The titania sol was prepared by adding titanium isopropoxide, $\text{Ti}(\text{OPri})_4$ (Aldrich, Milwaukee, WI), to an aqueous solution of nitric acid at a volumetric mixing ratio of 1 HNO_3 : 136.4 H_2O : 11.4 $\text{Ti}(\text{OPri})_4$. The zirconia sol was prepared by adding zirconium propoxide, $\text{Zr}(\text{OPrn})_4$ (Aldrich, Milwaukee, WI), to an aqueous solution of nitric acid at a volumetric mixing ratio of 1 HNO_3 : 50 H_2O : 3.7 $\text{Zr}(\text{OPrn})_4$. The individual sols were stirred continuously for 3-5 days until peptization was complete, after which the two sols were combined and stirred for approximately 30 min. The acidic mixed-oxide sol (pH of ca. 1) was dialyzed (Spectra/Por® 3 membrane, 3500 MW cutoff, Spectrum, Laguna Hills, CA) to a final pH of between 3.5 and 4.0.

Three layers of active catalyst material were deposited via dip-coating onto borosilicate glass cylinders or “rings” (4 mm o.d. x 3 mm i.d. x 12 mm long) that had been previously soaked in a 10% HNO_3 solution for 20 min, rinsed three times with ultrapure water and ashed at 450°C for 3 h. After applying a layer of catalyst, the rings were dried in air at 100°C for 1 h. After applying the last layer, the rings were fired in air at 350°C for 3 h after a 3°C per minute ramp rate. Physical properties of this catalyst can be estimated from measurements on a xerogel of the sol fired under the same conditions. Fu et al. [12] have reported the specific surface area and porosity of similarly prepared $\text{TiO}_2/\text{ZrO}_2$ particulates as 250 $\text{m}^2\cdot\text{g}^{-1}$ and 55%, respectively. Zorn et al. [13] determined the average total mass of

catalyst deposited using the above dip coating process as 0.12 mg/ring (for three coats), with an average composition by weight of 10% zirconia and 90% titania. The approximate thickness of the photocatalyst film was 390 nm [14].

3.2.2 Apparatus

Photocatalyst coated rings were packed in a 2.5 cm x 30 cm borosilicate glass column (Ace Glass Vineland, NJ) which was surrounded by eight 8 watt (Wiko model F8T5, Japan) blacklight blue (BLB) fluorescent bulbs (Bulb Direct Pittsford, NY). These bulbs were located 3.8 cm away from the centerline of the reactor and evenly spaced every 45°. Peak wavelength of the bulbs was 365 nm providing a light irradiance of 2.1, 2.1, and 1.6 mW-cm⁻² at 30, 70, and 100°C, respectively. Light irradiance was measured at the center of the reactor housing using a light meter (250–400 nm wavelength range, IL1400, International Light, Newburyport, MA). The lamps and glass column were held in place by an acrylic vessel (28 cm long and 12.7 cm diameter). Glass wool was packed into the ends of the glass column to maintain tight packing of the rings.

Compressed gas cylinders containing propane, isobutane, and n-butane at concentrations of 1004 ppmv, 925 ppmv, and 993 ppmv, respectively ($\pm 2\%$) were obtained from Linde Gas. The balance of the cylinder gas was hydrocarbon-free air containing less than 0.1 ppmv total hydrocarbons. Gas cylinders containing 101 ppmv acetone and 3000 ppmv CO₂ were also acquired from Linde for calibrating the gas chromatograph. Gas flowrates were controlled by MKS 1179A mass flow controllers (MFC) (MKS Instruments,

Wilmington, MA). A Gilian electronic bubble flow meter (Sensidyne, Clearwater, FL) was used to calibrate the MFCs.

The feed gas flowed either directly to the photoreactor (if no addition of water was required) or was split with a portion of the flow passing through a sparger to achieve the desired relative humidity (RH) in the inlet flow. Relative humidity was monitored upstream of the photoreactor with a humidity probe (P/N: HMP 235 Vaisala Inc., Woburn, MA).

After passing through the reactor, the effluent gas stream was sampled periodically via a six-way valve with a 250 μ l sampling loop connected to a gas chromatograph (GC) (Shimadzu GC-2010). The GC was equipped with a thermal conductivity detector (TCD) and a flame ionization detector (FID) positioned in series. The TCD detector was used to monitor CO₂ and water concentrations while the FID measured the test gas effluent and acetone generation. The capillary column was a 30 m x 0.32 mm Rt-QPLOT (Fused Silica PLOT) from Restek Corp. (Bellefonte, PA). The oven temperature was maintained at 35°C for 1 min followed by a ramp (15°C/min) to 180°C which was maintained for 1 min. Using the gas cylinders mentioned previously, four point calibration curves were generated for calibration of the FID and TCD.

3.2.3 Experimental Conditions

Glass rings (Qty = 315) coated with ZrO₂/TiO₂ were randomly packed in the 2.5 cm i.d. glass column. Three J-type thermocouples (Omega Engineering Inc., Stamford, CT) were evenly spaced in temperature wells along the length of the glass column to monitor reactor temperatures. Temperature wells consisted of a thin-walled, gas-tight, fish-hook shaped glass

tube blown into the glass column (Figure 3.3). After approximately one hour of illumination, the reactor reached a steady state temperature of $70^{\circ}\text{C} \pm 2^{\circ}\text{C}$. In experiments conducted at 35°C , cooling air was blown in at both ends of the acrylic vessel to maintain a constant temperature during the experiment. The cooling air flows in the annulus between the borosilicate column and the acrylic vessel. For experiments performed at 100°C , glass wool was packed around the ends of the reactor between the glass column and the acrylic vessel thereby reducing convective cooling.

After catalyst placement and initiation of illumination, a 30 min equilibration time proved adequate to attain stable relative humidity within the reactor and for the photocatalytic reaction to achieve steady state. Following equilibration, gas samples were acquired automatically every 18 min. This sample interval allows for the GC to analyze a sample and cool to the initial program temperature.

Single gas experiments were conducted to elucidate the influence of relative humidity and temperature on the photocatalytic oxidation of the three target gases. Experiments involving tertiary gas mixtures were also conducted. Conversion of the contaminant gases was monitored at five flowrates (50, 100, 150, 200 and 250 ml/min). By calculating an equivalent diameter of a sphere having the same external surface as a glass ring support, we were able to approximate the Reynolds number (N_R) for the flow conditions described above [15]. At each of the five flowrates $N_R < 1$ indicating that laminar flow conditions predominate in the reactor. The FID and TCD were calibrated at each of the five flowrates. This was required due to the fact that as flowrate increases, pressure also increases in the automatic sampling loop resulting in larger chromatogram peaks at larger flowrates. By

changing flowrates, it was possible to vary the space time (weight of catalyst / molar flowrate) yielding data suitable for kinetic analysis.

Reaction kinetics were assessed to establish reaction rate constants for the target gases. Both Power Law (Eq. 3.1) and Langmuir-Hinshelwood Hougen-Watson (LHHW) (Eq. 3.2) models were evaluated:

$$r_A = kC_A^n \quad (3.1)$$

where r_A is the reaction rate (in units of $\text{mol}\cdot\text{g}^{-1}\cdot\text{s}^{-1}$), k is the reaction rate constant (units depend on the reaction order, n), C_A is the contaminant effluent concentration ($\text{mol}\cdot\text{l}^{-1}$) and $n = 0.5, 1, 1.5$ and 2 .

$$r_A = kK_A C_A / (1 + K_A C_A) \quad (3.2)$$

Where k is the reaction rate constant ($\text{mol}\cdot\text{g}^{-1}\cdot\text{s}^{-1}$) and K_A is the equilibrium adsorption coefficient ($\text{l}\cdot\text{mol}^{-1}$).

3.3 Results and Discussion

3.3.1 Photolysis and Catalysis

Blank tests were performed in order to establish the effect of photolysis and catalysis on the conversion of these gases. No measurable conversion of the target gases was detected with UV illumination and no photocatalyst present in the reactor. Likewise, with the photocatalyst in the reactor and no UV illumination, no statistically significant change in initial gas concentrations could be detected.

3.3.2 Optimizing Photocatalyst Packing and Illumination

Efficient illumination of the catalyst is a critical design feature with a packed bed photocatalytic reactor. Ideally supports should be transparent to UV light or at least UV-C to allow activation of TiO_2 . The borosilicate glass supports used in this study absorb UV wavelengths shorter than 300 nm, therefore the supports do not interfere with the light necessary for activation of the photocatalyst (~365 nm). Lamp spacing should also be optimized to provide a minimum level of illumination to all of the photocatalyst. These two factors contribute to designs that minimize inactive catalyst or “dead zones” in the reactor. The high UV absorptivity of TiO_2 -based photocatalysts exacerbates this design obstacle. We evaluated four 30-cm-long glass columns, each with a different inner diameter (1.5, 2.5, 3.7, or 5.0 cm). The PCO of propane with an inlet concentration of 1004 ppmv was studied in these columns packed with catalyst-coated rings. The 1.5 cm column could hold a maximum of 102 rings while the 2.5 cm column could hold a maximum of 315 rings. For sake of comparison, 102 rings were studied in the 1.5 and 2.5 cm i.d. columns and 315 rings were tested in the 2.5, 3.7 and 5.0 cm i.d. columns. The same 102 or 315 rings were used in each experiment. Figure 3.1 is a plot of the fractional conversion versus space time for the four columns.

Figure 3.1 reveals that for both 102 and 315 catalyst coated rings a 2.5 cm i.d. reactor provides the highest conversion of propane. The 1.5 cm i.d. column should provide the best catalyst illumination as there was minimal catalyst overlap radially within the reactor. However, the conversion achieved in studies with the 1.5 cm i.d. column was significantly lower than that achieved in the 2.5 cm i.d. column. This observation was due to preferential

packing of the 12 mm long rings oriented lengthwise along the longitudinal axis of the reactor, yielding a less tortuous path and less catalyst-gas interaction. As the column diameter increases, the ring packing orientation was more random and the packing density was greater, providing a better opportunity for catalyst-gas interaction. However, in the larger diameter columns the UV light has to penetrate more catalyst layers in order to activate the rings in the center of the column.

The decrease in photocatalytic performance from the 2.5 cm to the 3.7 and 5.0 cm i.d. columns indicates that either the catalyst was not fully activated in the larger diameter columns or there may be mass transfer limitations due to lower gas velocities in the larger columns. Hill [16] provides a method for determining mass transfer limitations in heterogeneous catalytic reactors. By simultaneously varying the catalyst weight and molar flow rate, a constant reactor space time is maintained while linear velocity is varied. A plot of conversion versus linear velocity should yield a horizontal line if external mass transfer is not limiting. Should mass transfer limitations exist, conversion is expected to increase as the linear velocity increases due to a decrease in boundary layer thickness.

Figure 3.2 illustrates the fractional conversion versus linear velocity in the 2.5, 3.7, and 5.0 cm i.d. columns. As observed in Figure 3.1, conversion in experiments utilizing the 2.5 cm i.d. column was greater than in experiments utilizing the larger diameter columns. Conversion of propane in the 3.7 and 5.0 cm i.d. columns initially decreases as the linear velocity through the reactor increases, until leveling off at the larger velocities. When the catalyst bed was narrow (low linear velocity), a large percent of the catalyst was illuminated via the ends of the packing as opposed to mostly radial illumination in longer catalyst beds

(See Figure 3.3). As the number of rings in the reactor increases, the catalyst bed lengthens and end illumination effects decrease. Figure 3.2 demonstrates that as end illumination effects diminish, the conversion becomes relatively constant. This indicates that mass transfer limitations were not present. Therefore, the difference in conversion as the column diameter increases beyond 2.5 cm i.d. was not due to mass transfer limitations, but was a result of insufficient catalyst illumination near the centerline of the wider columns.

All subsequent data presented herein are from experiments using the 2.5 cm i.d. column. A single batch of 315 ZrO₂/TiO₂ coated glass rings was used throughout the duration of these experiments. Brigden et al. [5] reported catalyst deactivation after a few hours of n-butane photooxidation, however, throughout the course of our experiments we did not observe any deactivation of the photocatalyst during photooxidation of the contaminant gases.

3.3.3 Photocatalysis of Single Gases

Figure 3.4 compares the fractional conversion versus space time for the three test gases at 70°C and 30% RH. The figure indicates that the reactivity of these alkanes was similar. Isobutane conversion was slightly better than that of n-butane and not surprisingly propane conversion was ~5 – 10% lower than the butanes. Djeghri et al. [4] noted that longer chained alkanes had higher photoreactivities over TiO₂ and the reactivity was linked to the type of carbon atoms, $C_{\text{tert}} > C_{\text{quat}} > C_{\text{sec}} > C_{\text{prim}}$. Reaction pathways of the compounds may also affect the reactivity. The quantity of intermediates formed and their photoreactivity likely have salient impacts on the surface chemistry as well as competitive adsorption for active sites on the catalyst surface. Further studies utilizing Fourier Transform IR are planned

to better assess the formation of intermediates and catalyst surface chemistry directly using in situ techniques [17].

3.3.4 Effect of Relative Humidity

By fitting experimental results to the kinetic models one can obtain a more accurate comparison of the reactivity of these target gases. Over all of the experimental conditions tested, the $\frac{1}{2}$ order power law model often yielded the best fit to our data. The LHHW analysis did not always provide a meaningful fit; in some cases yielding a negative adsorption equilibrium constant. Figure 3.5 illustrates the $\frac{1}{2}$ order reaction rate constant for the three gases at 70°C as a function of inlet relative humidity ranging from <2 to 60% (~500 ppmv to ~ 16000 ppmv). Propane reaction rate constants were between 5 and 15% lower than those of the butanes. The lower constants were attributed to the stability of the shorter molecule.

Propane and n-butane both exhibited their highest reaction rate constants when relative humidity fell between 40 and 50%. Isobutane degradation peaked between 20 and 30% RH with degradation decreasing significantly as humidity increased beyond 30%. It is well established that water vapor is a source of OH radicals on the photocatalyst surface and that surface-mediated reactions deplete OH[•] if sufficient water is not available for replenishment [18]. Thus, under conditions of dry flow, the rate of photooxidation may be limited by the concentration of hydroxyl radicals. As humidity in the reactor increases, the reaction was no longer limited by the OH[•], leading to an observed increase in the reaction rate constant. At higher water concentrations, competitive adsorption of water with the contaminant gases for reactive sites on the catalyst surfaces may decrease reaction rates [19].

The effects of relative humidity on the PCO of VOCs have been studied by numerous researchers with often conflicting results and no readily discernable trend. The reactivity of acetone has been shown to increase [20,21] or decrease [22-25] as a result of increasing the concentration of water. There is an optimal water vapor concentration relative to trichloroethylene concentrations, with reactivity decreasing dramatically as humidity levels surpass the optimum [23,24,26-28]. Investigations involving the PCO of ethylene [29,30] and heptane [31] found an inverse relationship between water vapor concentration and reaction rate, whereas photocatalysis of hexane showed an initial increase in conversion up to 20% RH followed by a significant decrease in conversion at RH higher than 45% [32]. The short alkanes examined in this study yielded results similar in nature to those for hexane, albeit with peak activity over dissimilar RH ranges. These variations were likely a result of differences in adsorption mechanisms between the straight and branched molecules.

3.3.5 Effect of Temperature

Herrmann [33] asserts that optimal temperatures for photocatalytic reactions are typically found between 20°C and 80°C and it is commonly accepted that temperature increases have little or no effect on photocatalytic rates [8]. We evaluated the degradation of the gases in a dry feed stream at 35, 70 and 100°C. Figure 3.6 compares the performance of propane oxidation at these temperatures. Conversion of isobutane and n-butane showed similar responses to temperature. A significant improvement in performance occurs as the temperature increases from 35 to 70°C, but no noticeable increase was apparent between 70 and 100°C. Zorn et al. [21] observed a similar response to temperature in photocatalytic

oxidation of acetone and ascribed the differences to a 25% decrease in UV light intensity from 77 to 113°C. Similarly, UV light irradiance in this study dropped from 2.1 to 1.6 mW cm⁻² at 70 and 100°C, respectively.

3.3.6 Complete Mineralization

For purposes of contaminant control, complete oxidation of target species to CO₂ and water is the desired result. Accordingly, complete oxidation of propane and butane should yield three and four moles of CO₂, respectively. Percent mineralization was calculated by dividing the quantity ([CO₂-generated] / [ΔC_nH_{2n+2}]) by three or four depending on the alkane with a value of 100% indicating complete oxidation. Figure 3.7 shows the percent mineralization of the three gases averaged over the range of relative humidity tested. Mineralization generally decreased with increasing flowrate which was a consequence of decreasing the residence (or contact) time in the reactor. Increasing reactor temperature from 70°C to 100°C did not greatly affect the mineralization of propane or isobutane. Conversely, the percent mineralization of n-butane decreased at the higher temperature (100°C). Figure 3.8 provides a closer look at the effect of relative humidity on mineralization at 70°C and a flowrate of 150 mL min⁻¹. As seen in Figures 3.7 and 3.8, the degree of mineralization of n-butane was substantially higher than that of the other two gases. This was most likely due to the relative reactivity of the intermediates formed during photooxidation. Acetone is the primary intermediate of isobutane and propane photocatalysis whereas butanone is the primary intermediate of n-butane [4]. As detailed in section 3.4.4, acetone photooxidation has been shown to both increase and decrease as water concentration increases. The disparity of

these results is likely due to differences in catalyst characteristics [34]. Raillard et al. studied the photooxidation of acetone and 2-butanone over TiO_2 containing paper and observed greatly inhibited acetone photoactivity as RH increased while RH had little effect on 2-butanone photodegradation [25].

Figure 3.9 depicts the acetone formation during photocatalytic oxidation of propane and isobutane as RH increases. For sake of clarity, data from 50, 150 and 250 mL min^{-1} flowrates have been omitted. As water vapor increases in the reactor, complete oxidation decreases and the selectivity for acetone formation increases. The selectivity to acetone is not strictly a function of isobutane or propane oxidation, rather it may be the combined effects of reaction pathway and the inhibitory affects of water concentration on acetone photoreactivity. No acetone was detected in the photocatalysis of n-butane.

3.3.7 A Tertiary Mixture

A feed stream containing a tertiary mixture of the gases was passed through the photoreactor under conditions of 70°C and 30% RH. Inlet concentrations for propane, isobutane and n-butane were 338, 297, and 325 ppmv, respectively. The fractional conversion versus space time for each gas in the mixture is given in Figure 3.10. Whereas the single gases had very similar photocatalytic reactivity (see Figure 3.4), in the tertiary mixture, n-butane yields a much higher conversion relative to isobutane and propane. Assuming the number of active catalyst sites remains relatively constant from one experiment to another, n-butane may preferentially adsorb to these sites better than isobutane and propane. Propane, having the highest vapor pressure, was the least competitive for surface adsorption and it was

observed that it was the least reactive of the gases. Thus, propane degradation rates would be the limiting factor in designing a photocatalytic reactor for treatment of a similar tertiary mixture.

3.4 Conclusions

Observations presented in this study suggest that nearly complete oxidation of low molecular weight alkanes is possible over $\text{ZrO}_2\text{-TiO}_2$ thin films at near ambient conditions. Reactor diameter affects packing of the glass ring supports and illumination of the catalyst. A 2.5 cm i.d. column diameter proved optimal for conversion of the target gases employing the photocatalyst supported on 1.2 cm long glass rings. In studies using a 1.5 cm i.d. column, the rings preferentially packed inline with the longitudinal axis of the column allowing unacceptable bypass. Moreover, light penetration was not sufficient to fully activate the thicker catalyst beds in studies with the 3.7 and 5.0 cm i.d. columns.

Similar photoactivity was demonstrated for isobutane and n-butane, but isobutane activity peaked between 20 and 30% RH while n-butane photoactivity peaked between 40 and 50% RH. Propane photoactivity was distinctly slower than the butanes studied, but responded to humidity in a manner similar to n-butane. Increasing the reactor temperature, as monitored within the thermocouple well, from 35 to 70°C significantly enhanced reaction rates while an increase from 70 to 100°C had little effect.

Mineralization of n-butane was greater than isobutane and propane, possibly due to reaction mechanisms and the photoreactivity of intermediates formed during photooxidation. Increasing relative humidity had a detrimental effect on mineralization of all three gases.

Generation of acetone from photocatalysis of isobutane and propane also increased as relative humidity increased.

In a tertiary mixture with approximately equal concentrations of the three gases, n-butane conversion was higher than isobutane, and both butanes had significantly higher fractional conversions as compared to propane. The differences in conversion were partially attributed to the disparity in vapor pressures as a driving force in competitive adsorption for active sites on the catalyst surface.

References

- [1] R.M.Alberici, W.E.Jardim, Appl. Catal. B 14 (1997) 55-68.
- [2] O.Carp, C.L.Huisman, A.Reller, Prog. Solid State Chem. 32 (2004) 33-177.
- [3] J.Peral, X.Domenech, D.F.Ollis, J. Chem. Technol. Biotechnol. 70 (1997) 117-140.
- [4] N.Djehgri, M.Formenti, F.Juillet, S.J.Teichner, Faraday Discuss. (1974) 185-193.
- [5] C.T.Brigden, S.Poulston, M.V.Twigg, A.P.Walker, A.J.J.Wilkins, Appl. Catal. B 32 (2001) 63-71.
- [6] T.Tanaka, T.Ito, S.Takenaka, T.Funabiki, S.Yoshida, Catal. Today 61 (2000) 109-115.
- [7] K.Wada, K.Yoshida, T.Takatani, Y.Watanabe, Appl. Catal. A 99 (1993) 21-36.
- [8] M.A.Fox, M.T.Dulay, Chem. Rev. 93 (1993) 341.
- [9] USEPA, Protection of Stratospheric Ozone, 40 CFR Parts 9 and 82, 94 A.D., p. IX. i.
- [10] N.A.Kelly, T.Y.Chang, Atmos. Environ. 33 (1999) 2101-2110.
- [11] Q.Y.Xu, M.A.Anderson, J. Mater. Res. 6 (1991) 1073-1081.
- [12] X.Z.Fu, L.A.Clark, Q.Yang, M.A.Anderson, Environ. Sci. Technol. 30 (1996) 647-653.
- [13] M.E.Zorn, D.T.Tompkins, W.A.Zeltner, M.A.Anderson, Environ. Sci. Technol. 34 (2000) 5206-5210.
- [14] A.Sirisuk, C.G.Hill, M.A.Anderson, Catal. Today 54 (1999) 159-164.
- [15] A.Sirisuk, Photocatalytic Oxidation of Ethylene over Thin Films of Titanium Dioxide Supported on Glass Rings, Ph.D. Thesis, University of Wisconsin-Madison, Madison, WI, 2003.
- [16] C.G.Hill Jr., An Introduction to Chemical Engineering Kinetics & Reactor Design, Wiley, New York, 1977.
- [17] J.M.Coronado, S.Kataoka, I.Tejedor-Tejedor, M.A.Anderson, J. Catal. 219 (2003) 219-230.
- [18] T.N.Obee, R.T.Brown, Environ. Sci. Technol. 29 (1995) 1223-1231.

- [19] L.X.Cao, Z.Gao, S.L.Suib, T.N.Obee, S.O.Hay, J.D.Freihaut, *J. Catal.* 196 (2000) 253-261.
- [20] J.M.Coronado, M.E.Zorn, I.Tejedor-Tejedor, M.A.Anderson, *Appl. Catal. B* 43 (2003) 329-344.
- [21] M.E.Zorn, D.T.Tompkins, W.A.Zeltner, M.A.Anderson, *Appl. Catal. B* 23 (1999) 1-8.
- [22] S.Hager, R.Bauer, *Chemosphere* 38 (1999) 1549-1559.
- [23] S.B.Kim, S.C.Hong, *Appl. Catal. B* 35 (2002) 305-315.
- [24] S.B.Kim, H.T.Hwang, S.C.Hong, *Chemosphere* 48 (2002) 437-444.
- [25] C.Raillard, V.Hequet, P.Le Cloirec, J.Legrand, *J. Photochem. Photobiol. A* 163 (2004) 425-431.
- [26] L.A.Dibble, G.B.Raupp, *Catal. Lett.* 4 (1990) 345-354.
- [27] L.A.Dibble, G.B.Raupp, *Environ. Sci. Technol.* 26 (1992) 492.
- [28] T.H.Lim, S.D.Kim, *Chemosphere* 54 (2004) 305-312.
- [29] T.N.Obee, S.O.Hay, *Environ. Sci. Technol.* 31 (1997) 2034-2038.
- [30] X.Z.Fu, L.A.Clark, W.A.Zeltner, M.A.Anderson, *J. Photochem. Photobiol. A* 97 (1996) 181-186.
- [31] J.Shang, Y.G.Du, Z.L.Xu, *Chemosphere* 46 (2002) 93-99.
- [32] P.Y.Zhang, J.Liu, *J. Photochem. Photobiol. A* 167 (2004) 87-94.
- [33] J.M.Herrmann, *Catal. Today* 53 (1999) 115-129.
- [34] C.Raillard, V.Hequet, P.Le Cloirec, J.Legrand, *Water Sci. Technol.* 50 (2004) 241-250.

Figures

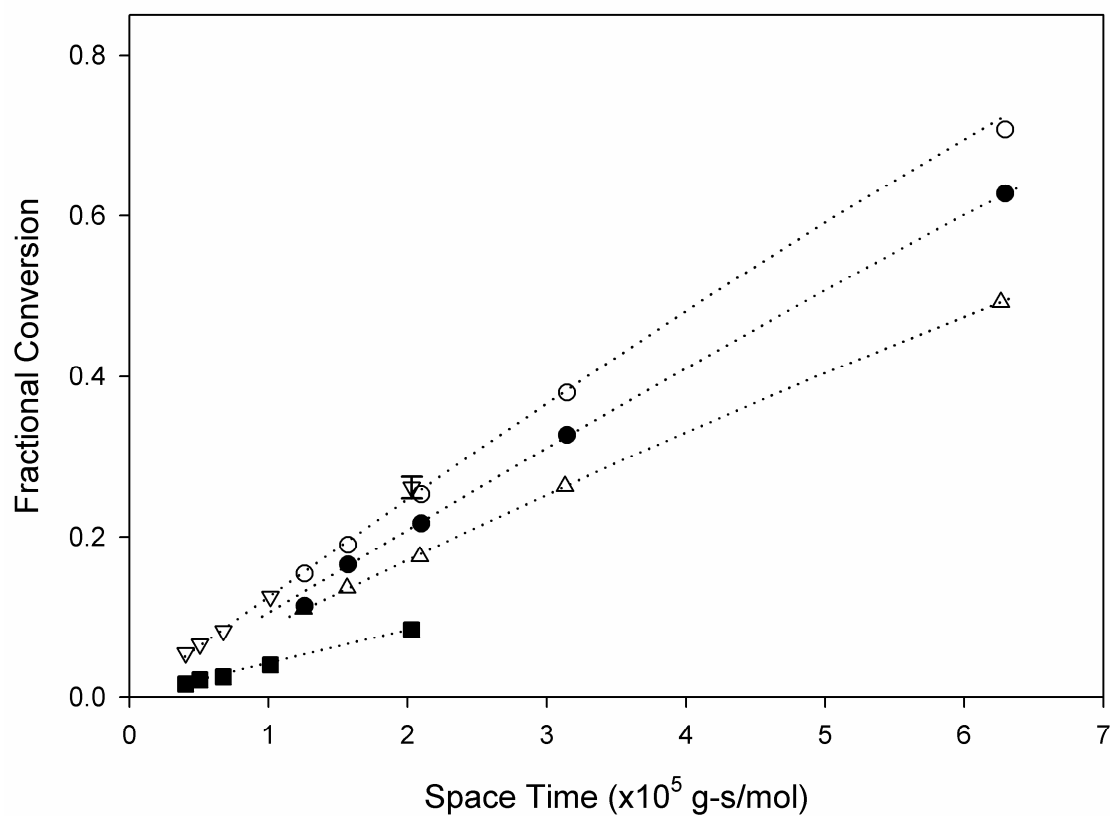


Figure 3.1 Propane conversion at 70°C and 50% RH as a function of column diameter and number of rings: 1.5 cm i.d. – 102 rings (■), 2.5 cm i.d. – 102 rings (▽), 2.5 cm i.d. – 315 rings (○), 3.7 cm i.d. – 315 rings (●), 5.0 cm i.d. – 315 rings (△). Dotted lines represent the predicted conversion using the $\frac{1}{2}$ order power law model. Data points are average value of 3 samples. Except where shown, error bars fall within the area of the series marker.

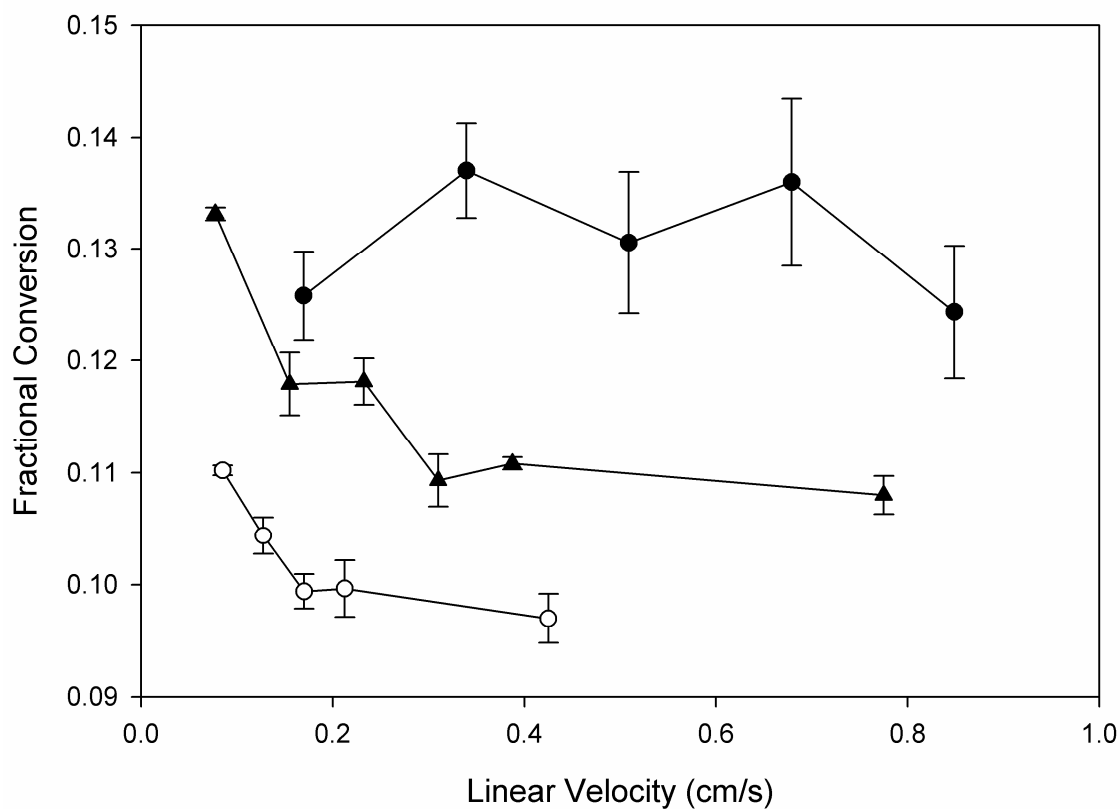


Figure 3.2 Propane conversion versus linear velocity through the catalyst bed at constant space time. 2.5 cm i.d. (●), 3.7 cm i.d. (▲), 5.0 cm i.d. (○) Conditions: 70°C and 50% RH. Error bars for the 2.5 cm i.d. column are representative of 6 samples from 2 studies (catalyst was removed and repacked between studies – 3 samples per study). Error bars for the 3.7 cm i.d. and 5.0 cm i.d are for 3 replicate samples from one study each.

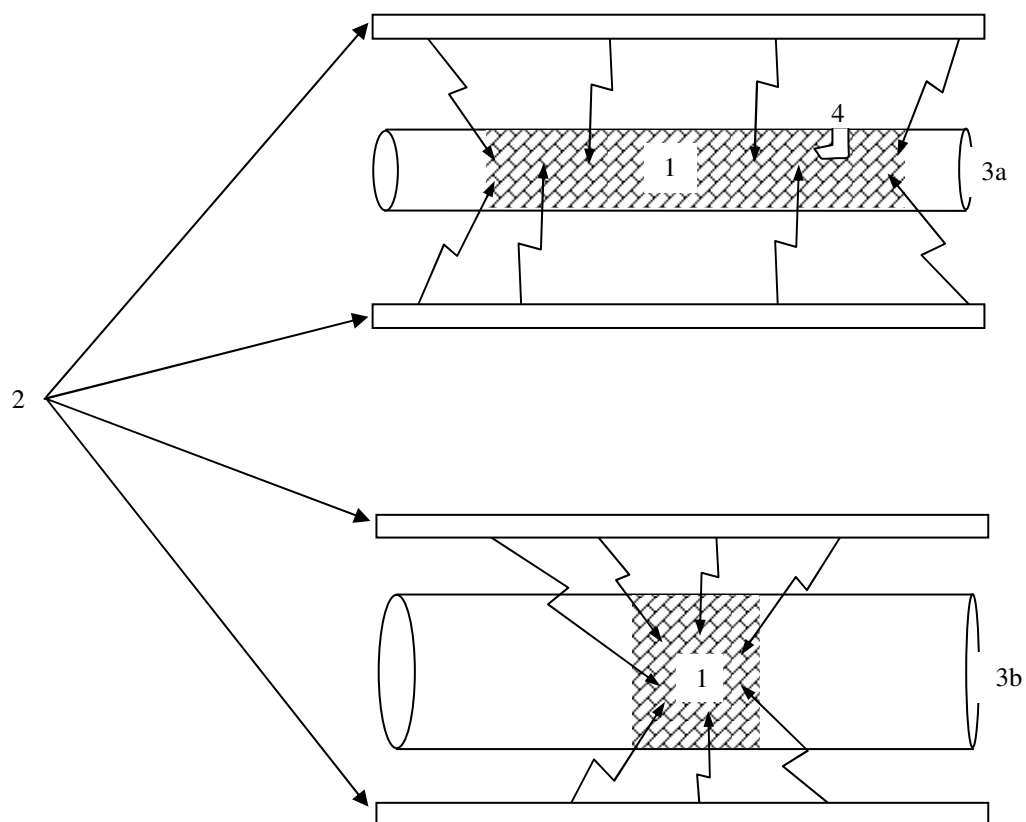


Figure 3.3 Schematic illustrating catalyst illumination in tubular reactor and the influence of end illumination as reactor diameter increases for a constant number of photocatalyst coated rings. 1) Photocatalyst bed, 2) UV light sources, 3) Glass column reactor: a) 2.5 cm i.d. b) 5.0 cm i.d., 4) Temperature wells. (Drawing not to scale).

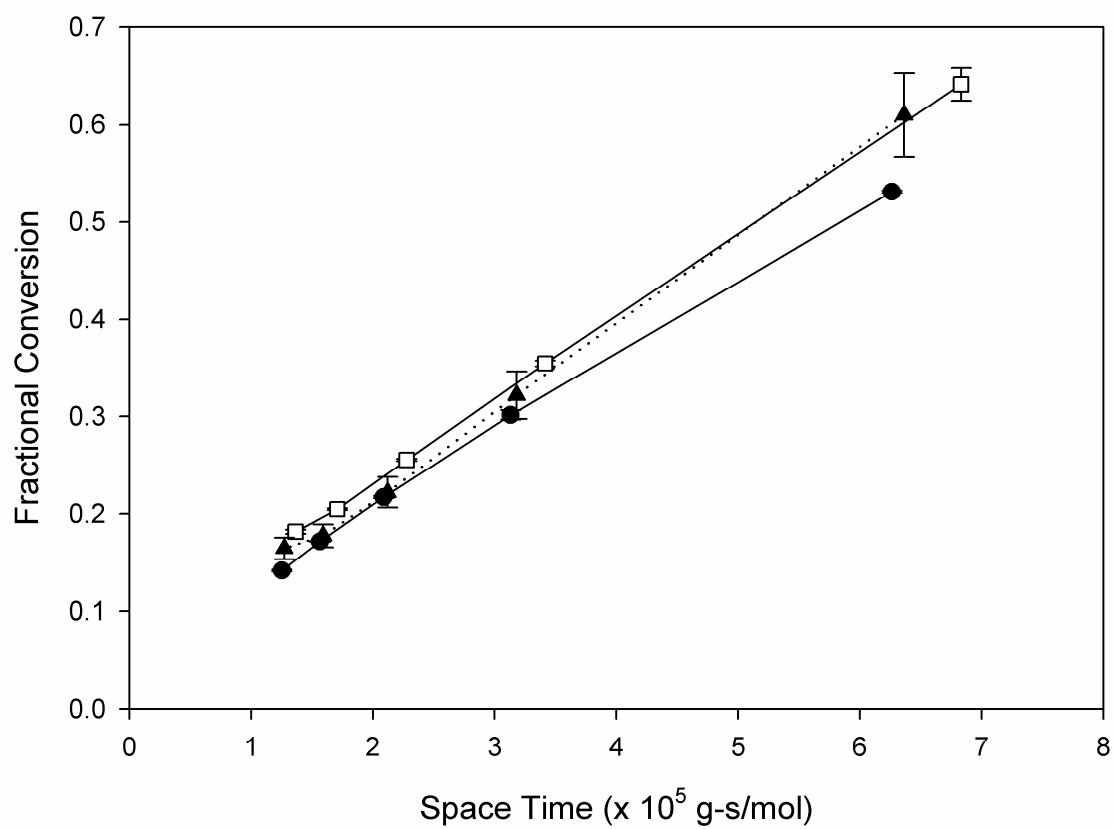


Figure 3.4 Single gas conversions versus space time @ 70°C and 30% RH. Propane (●), Isobutane (□), n-butane (▲). Data points are average value of 3 samples.

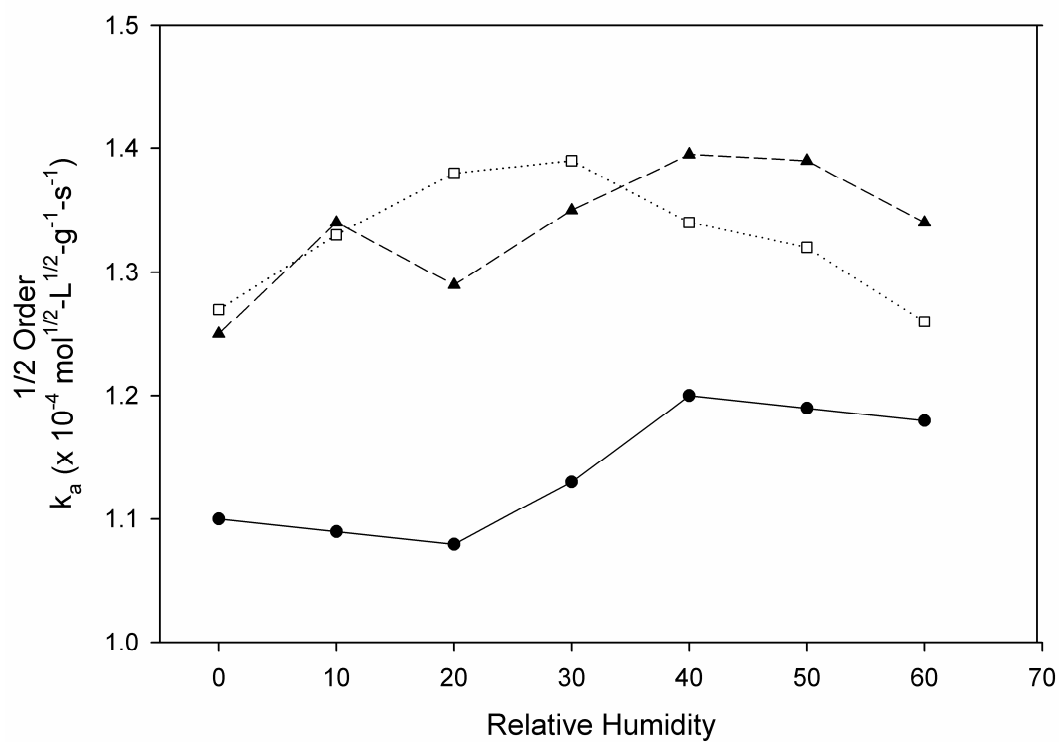


Figure 3.5 Reaction rate constants ($1/2$ order power law model) for single gas experiments at 70°C as a function of relative humidity. Propane (\bullet), Isobutane (\square), n-butane (\blacktriangle).

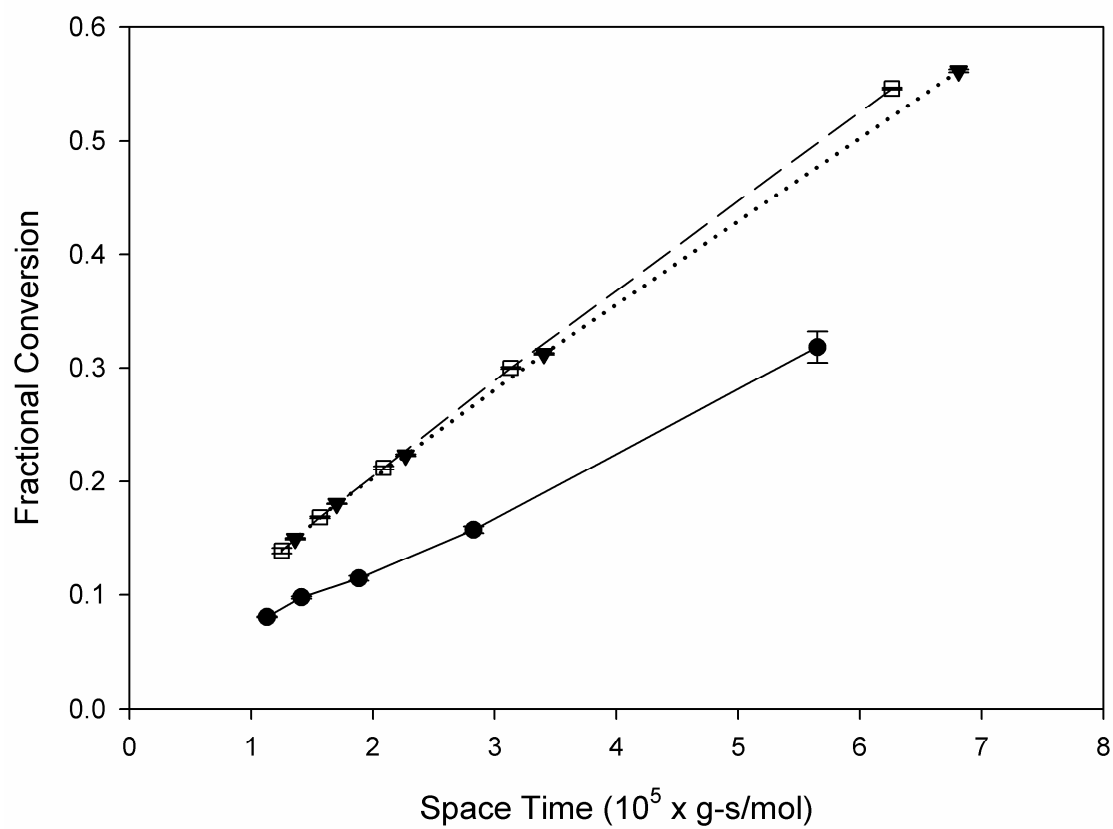


Figure 3.6 Temperature effect on propane conversion in a dry feed stream. 35°C (●), 70°C (□) and 100°C (▼). Data points are average value of 3 samples.

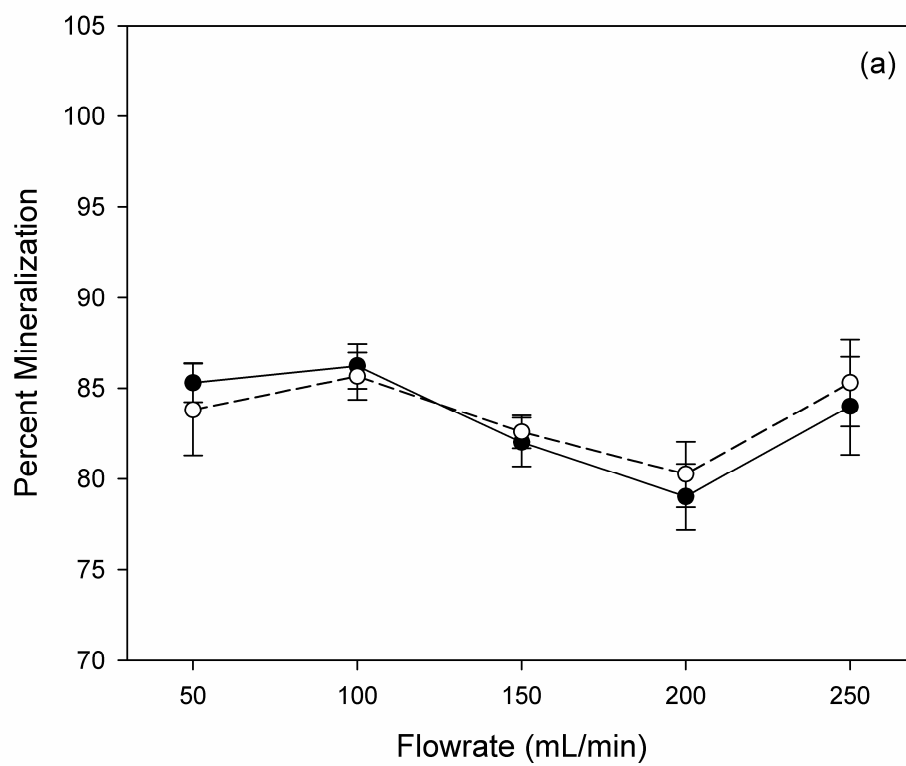


Figure 3.7a Percent mineralization averaged over the humidity range tested (<2% – 60%) versus flowrate. (a) Propane: 70°C (●) and 100°C (○). Error bars represent the standard deviation of the averaged values.

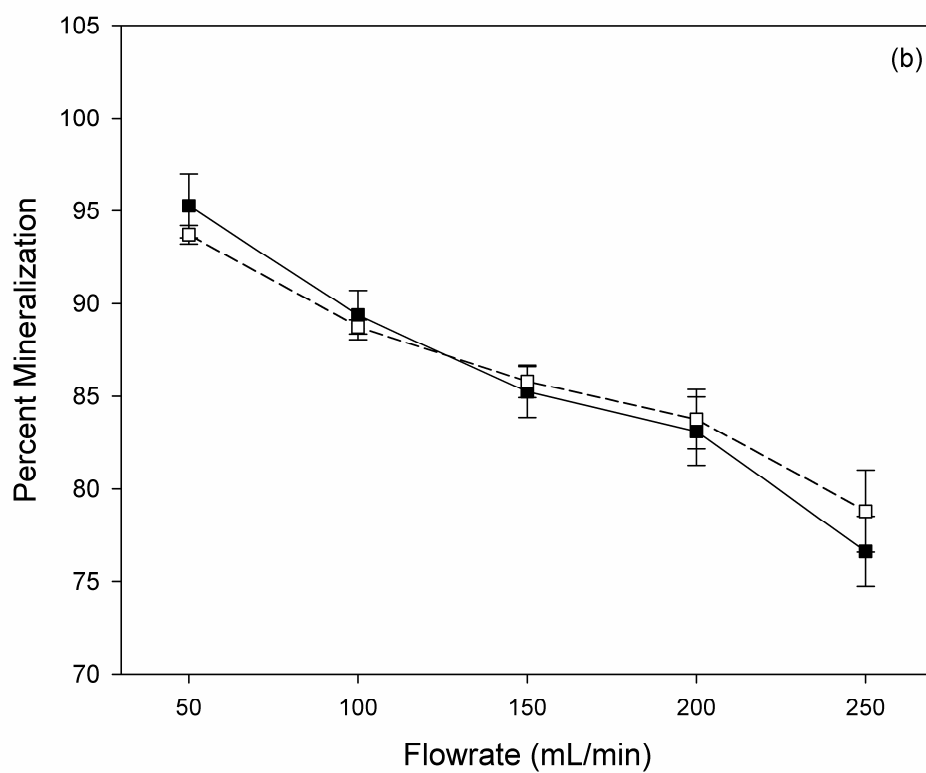


Figure 3.7bPercent mineralization averaged over the humidity range tested (<2% – 60%) versus flowrate. (b) Isobutane: 70°C (■) and 100°C (□). Error bars represent the standard deviation of the averaged values.

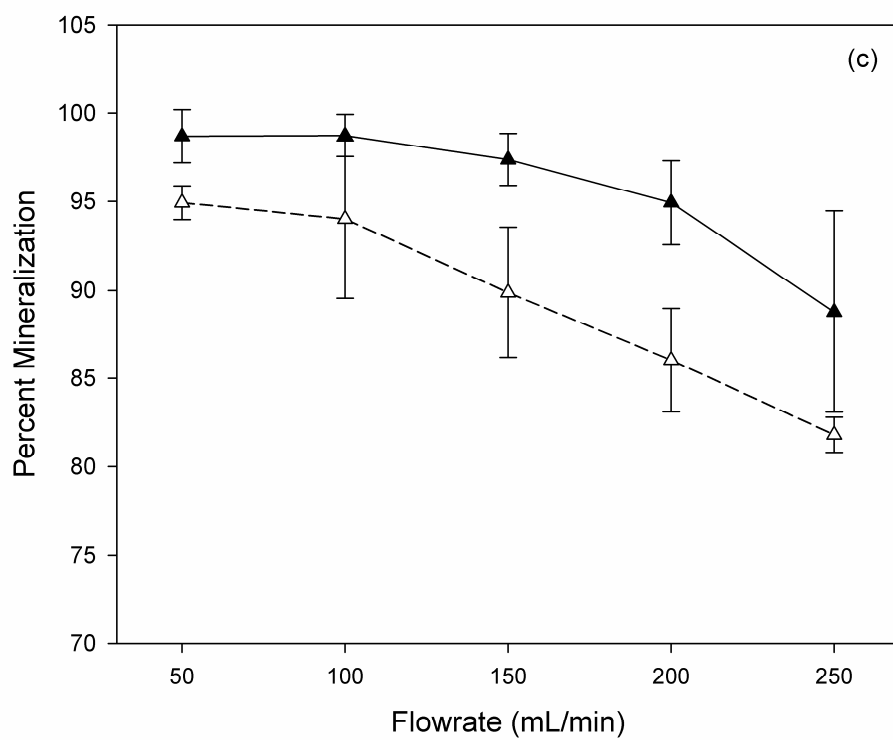


Figure 3.7c Percent mineralization averaged over the humidity range tested (<2% – 60%) versus flowrate. (c) n-butane 70°C (▲) and 100°C (△). Error bars represent the standard deviation of the averaged values.

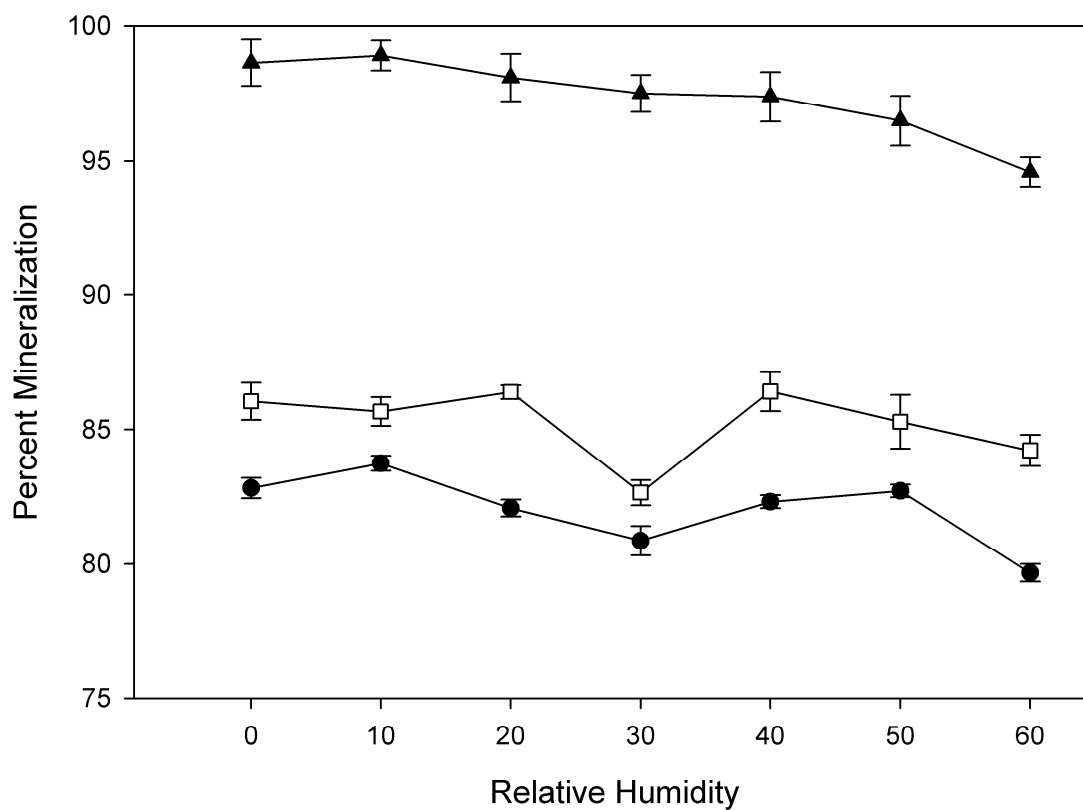


Figure 3.8 Effect of relative humidity on percent mineralization of single gases. 70°C and 150 mL/min. Propane (●), Isobutane (□), n-butane (▲). Data points are average value of 3 samples.

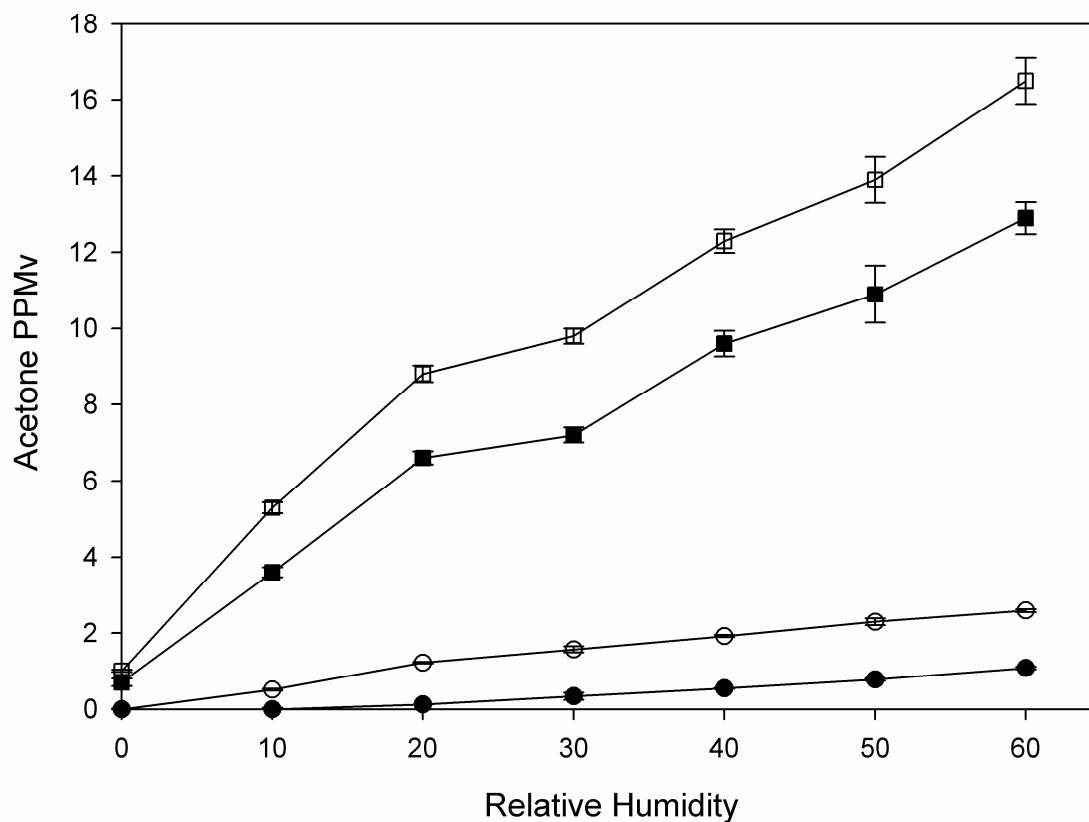


Figure 3.9 Acetone generation from photocatalysis of isobutane and propane single gas experiments at 70°C. Isobutane: 200 mL/min (□), 100 mL/min (■). Propane: 200 mL/min (○) and 100 mL/min (●). Acetone was not detected in PCO studies of n-butane. Data points are average value of 3 samples.

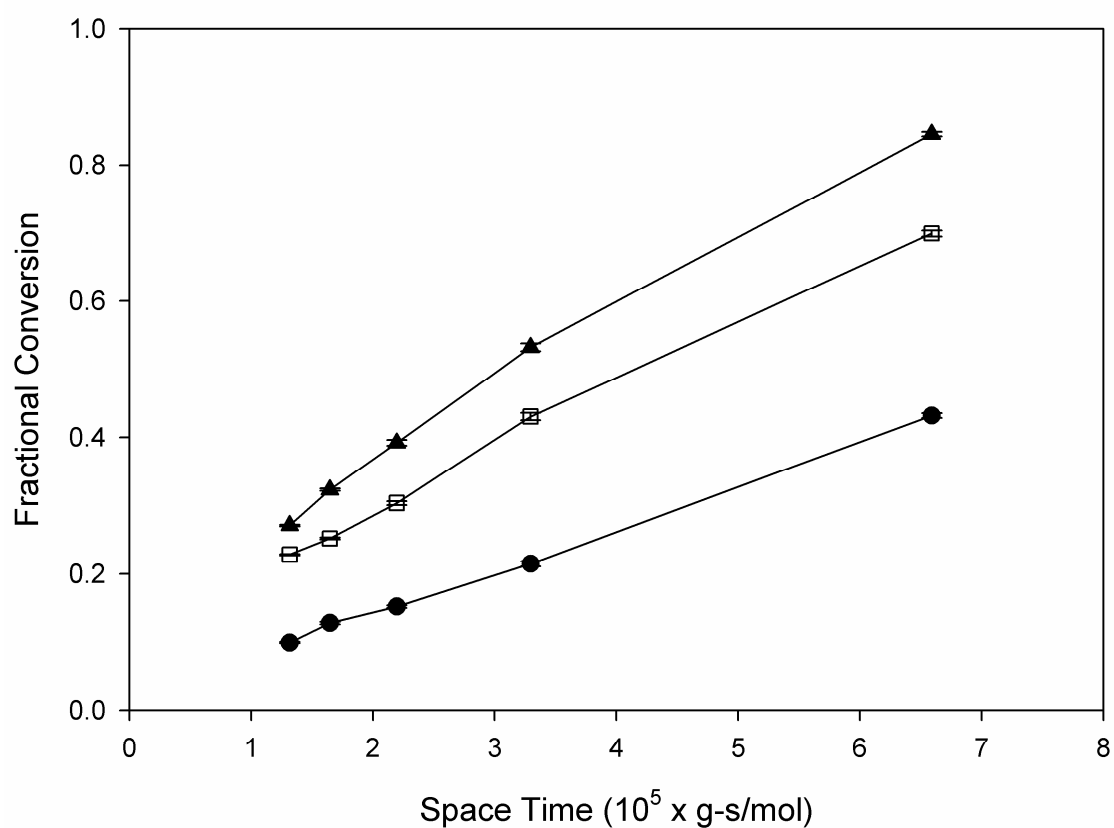


Figure 3.10 Fractional conversion of gas components in a tertiary mixture consisting of 338 ppmv propane, 297 ppmv isobutane and 325 ppmv n-butane. 70°C and 30% RH. Propane (●), Isobutane (□), n-butane (▲). Data points are average value of 3 samples.

Chapter 4

Thermally assisted photocatalysis of propane using precious metal modified thin films

Abstract

Six precious metals (Ag, Au, Pd, Pt, Rh, and Ru) were tested at 1 weight percent loadings in TiO₂, SiO₂/TiO₂, and ZrO₂/TiO₂ photocatalytic thin films for oxidation of propane. Thin films were synthesized via a sol-gel route, coated on glass rings and evaluated in a tubular reactor at reaction temperatures of 50, 75 and 100°C. Analysis of propane conversion data reveals that at 1% loading, the metals reduced the activity for conversion of propane, regardless of temperature. Platinum, gold and silver modified photocatalysts had the highest activity of the metal-modified materials while the palladium, rhodium and ruthenium materials had little activity for the conversion of propane. Evaluation of oxidation intermediates and CO₂ data showed near complete (>95%) mineralization of propane and a decrease in the trace quantity of acetaldehyde that was present in the influent over many of the materials that were tested.. Reactor temperature significantly affected the irradiance in the photoreactor. Reaction rates adjusted for the influence of temperature on reactor irradiance revealed that the highest reaction rates occurred at 100°C, but evaluation of Langmuir-Hinshelwood-Hougen-Watson kinetics showed that temperature significantly affected the surface adsorption of propane. Of the 21 materials tested, an unmodified ZrO₂/TiO₂ thin film had the best activity for propane conversion and mineralization.

4.1. Introduction

The 1978 ban on the use of chlorofluorocarbons (CFCs) in the U.S. led to the increased use of light alkanes (C_3 - C_6) as substitutes for CFC-based propellants in aerosol cans [1]. Light alkanes are classified as volatile organic carbons (VOCs). VOCs have been linked to tropospheric ozone formation [2], resulting in a need for abatement control technologies at facilities that manufacture aerosol spray cans. Manufacturing emissions are typically high in volumetric flow ($25 - 75 \text{ m}^3\text{-min}^{-1}$) and low in concentrations ($< \sim 1,500 \text{ ppmv}$). These characteristics, coupled with the high vapor pressure and chemical stability that render light alkanes as excellent propellants, also make alkanes difficult compounds to oxidize. Heterogeneous photocatalytic oxidation (PCO) may be a treatment alternative with the potential to be a cost effective and an efficient technology to treat VOCs.

The photocatalytic degradation of light alkanes over TiO_2 was first studied by Djeghri et al. in the 1970s [3]. Photocatalytic activity was linked to the length of the carbon chain, with longer chains being more reactive. This work also proposed a mechanism by which an alkane decomposes to an alcohol or alkene, which quickly converts to an aldehyde or ketone and finally may decompose to CO_2 . Subsequent studies have corroborated the proposed reaction mechanism [4-6]. In a waste treatment scenario incomplete mineralization and consequent formation of certain intermediates presents a potential problem. The reactivity of aldehydes in photochemical smog-forming reactions is much higher than that of light alkanes and ketones [7,8]. Thus the formation of aldehydes as partial oxidation products, even in very limited quantities, may present a worse pollution problem than that posed by alkanes.

Propane is a key component of propellant mixtures and would likely be the limiting component in development of a treatment alternative because of the higher stability of the shorter carbon chain. Studies investigating the photocatalysis of propane have focused on improving the selectivity to intermediate reaction products [5,6,9] with a lesser focus on achieving complete oxidation of propane [4,10]. Recently, Haaglund et al. [4] used diffuse reflectance Fourier transform infrared spectroscopy to assess the optimal reaction conditions for the complete oxidation of propane. They suggested that optimal PCO of propane on TiO_2 requires a balance among (i) sustaining a photoactive water monolayer on the catalyst surface to prevent detrimental bonding of surface species, (ii) allowing reactants to adsorb to bulk TiO_2 , and (iii) maximizing the thermally assisted decomposition of intermediates. Optimal conditions of 1% water in a 130°C reactant gas stream were reported.

Photocatalytic reactions are generally considered to be relatively insensitive to increases in temperature since the activation energy for the reaction is gained from absorption of a photon [11-13]. However, several studies of the photocatalytic destruction of VOCs have demonstrated elevated temperatures to be beneficial to some degree [14-20]. It is suggested that improvements in reactivity at temperatures up to approximately 130°C are often correlated to shifts in the adsorption-desorption equilibrium of reactants and products on the catalyst surface thereby freeing up additional sites for the desired reaction [4,14]. The addition of precious metals to photocatalysts has also been shown to improve the oxidation of numerous VOCs (including acetone and acetaldehyde) when PCO reactors were operated at high temperatures [17-21]. These studies suggest that improvements in photocatalytic destruction are a result of the catalytic effect of the metals.

Platinum and palladium are the most commonly used precious metals for propane destruction in thermal catalytic reactors, but light-off temperatures are typically greater than 200°C [22-24]. However, Rodemerck et al. [24] demonstrated that numerous precious metals are capable of catalytically oxidizing propane at low temperatures. They evaluated a plethora of titania-supported metal catalysts for low-temperature catalytic oxidation of 0.1% (1,000 ppmv) propane in a balance of air. Ruthenium at a loading of 3 weight percent was the most active precious metal showing ca. 20%, 25% and 75% propane conversion at 50, 100 and 150°C, respectively (no CO₂ generation data were reported). Other catalysts showing activity for propane conversion included (in descending order of performance) Rh, Pt, Pd, Au, Cu, Ag and Mn. This work suggests several precious metals may prove beneficial as additives in a PCO system if operated at temperatures greater than 50°C.

One of the attractive features of TiO₂ photocatalysis is its substantial activity at room temperatures. However, a large scale reactor will likely operate at temperatures much greater than room temperature. The large bank of UV-lights required for sufficient illumination of the catalyst will produce a significant quantity of thermal energy, given that approximately 80% of the energy used by UV fluorescent bulbs is given off in the form of heat. By capitalizing on the heat generated by the lamps through incorporation of precious metals into a photocatalyst, one may increase the overall conversion of propane to CO₂.

Previous work in our laboratory using ZrO₂/TiO₂ thin films supported on glass *rings* showed nearly 80% mineralization of propane at near ambient conditions [25]. In the current study, we evaluate the performance of metal modified photocatalytic thin films for the destruction of a 1000 ppmv propane air stream. Six precious metals (gold, palladium,

platinum, rhodium, ruthenium, and silver) were evaluated as additives to TiO_2 , $\text{SiO}_2/\text{TiO}_2$, and $\text{ZrO}_2/\text{TiO}_2$ photocatalysts. Our goal has been to improve the mineralization of propane and to increase the PCO reaction rate. Detailed characterization of the physical properties of the metal-modified thin films is discussed along with results of photocatalytic testing.

4.2 Experimental Methods

4.2.1 Catalyst Preparation and Characterization

All catalysts were prepared using sol-gel methods [26]. Binary oxides were mixed according to the optimal percent mixing of ZrO_2 or SiO_2 as presented by Fu et al. [27]. The appropriate metal oxide sols were prepared by acid hydrolysis of their metal alkoxide precursors. The separate sols were stirred until clear and then mixed to the desired composition. The titania sol was prepared by adding titanium isopropoxide, $\text{Ti}(\text{OPr}^i)_4$ (Aldrich, Milwaukee, WI), to an aqueous solution of nitric acid at a volumetric mixing ratio of 1 HNO_3 : 136.4 H_2O : 11.4 $\text{Ti}(\text{OPr}^i)_4$. The zirconia sol was prepared by adding zirconium propoxide, $\text{Zr}(\text{OPr}^n)_4$ (Aldrich, Milwaukee, WI), to an aqueous solution of nitric acid at a volumetric mixing ratio of 1 HNO_3 : 50 H_2O : 3.7 $\text{Zr}(\text{OPr}^n)_4$. The individual sols were stirred continuously for 3-5 days until peptization was complete. The silica sol was prepared in a slightly different manner. Tetraethyl orthosilicate [$\text{Si}(\text{OC}_2\text{H}_5)_4$] was mixed with ethanol, water, and HCl in a volumetric ratio of 2000:525:625:1. Appropriate volumes of the pure precursor sols to achieve a 12 wt % and 16 wt % mixing of the ZrO_2 and SiO_2 , respectively, in the TiO_2 sol were combined and stirred for approximately 30 min. The unmodified acidic

sols (pH of ca. 1) were dialyzed in ultrapure ($>18\text{ M}\Omega\text{cm}$) water (Spectra/Por® 3 membrane, 3500 MW cutoff, Spectrum, Laguna Hills, CA) to a final pH of ca. 2 or 3.

Metal modification of the TiO_2 and $\text{ZrO}_2/\text{TiO}_2$ sols was achieved by adding an aliquot of an 8 weight percent aqueous metal salt solution to the undialyzed sol in an amount appropriate to achieve 1 weight percent loading of the metal. After 2 hr of stirring, the metal was reduced by addition of NaBH_4 dissolved in a 0.01M NaOH solution. The reduced sols were titrated with nitric acid to pH 1.5 prior to dialysis. Because of the low isoelectric point of SiO_2 ($\text{IEP} \approx 2.5$), modified $\text{SiO}_2/\text{TiO}_2$ sols were made in a slightly different manner. Undialyzed TiO_2 was first modified with the selected metal, but at a loading higher than 1 wt %. The SiO_2 and metal modified TiO_2 were mixed following reduction of the metal and titration of the M- TiO_2 sol to pH ca. 1.5. This procedure was followed to prevent destabilizing of the binary mixture as the pH increased during the metal reduction step. The metal modified $\text{SiO}_2/\text{TiO}_2$ mixture was dialyzed as described above. The mass of catalyst per volume of sol for the entire suite of catalyst materials ranged from 23–35 g/L. Thin film coatings were applied to borosilicate glass tubes (3-mm ID, 4-mm OD, 12-mm long) or “rings” following a dip coating procedure described previously [25]. The coated rings were then fired at 350°C in air for 3 hours using a $3^\circ\text{C}/\text{min}$ ramp and allowing the furnace to cool at its natural rate after firing.

Throughout the remainder of this chapter the catalysts will be referred to as m-T, m-S/T, m-Z/T where “m” represents the precious metal and T, S/T, and Z/T correspond to TiO_2 , $\text{SiO}_2/\text{TiO}_2$, and $\text{ZrO}_2/\text{TiO}_2$, respectively.

4.2.2 Apparatus

A photocatalytic reactor similar to that described previously [25] was used in this study, but with slight modification. Three hundred photocatalyst coated rings were packed in a 2.5 cm x 30 cm borosilicate glass column (Ace Glass Vineland, NJ) which was surrounded by eight 8-W (Sylvania model F8T5, Danvers, Massachusetts) blacklight (BL) fluorescent bulbs (Bulb Direct Pittsford, NY). These bulbs were located 3.8 cm away from the centerline of the reactor and were evenly spaced every 45°. The UV lamps and glass column were held in place by a piece of cylindrically-fabricated (28 cm long and 12.7 cm diameter) sheet metal. Light irradiance was measured at the center of the glass column using a ramp-probe, light meter (250–400 nm wavelength range, IL1400, International Light, Newburyport, MA). The ramp probe was placed in the center of the reactor column and rotated on the centerline of the column with eight irradiance measurements recorded (i.e. every $\frac{1}{4} \pi$ radians). Peak wavelength of the lamps was 365 nm providing a light irradiance of 5.1 ± 0.2 , 4.1 ± 0.20 , 3.05 ± 0.09 , and $2.38 \pm 0.37 \text{ mW-cm}^{-2}$ at 35, 50, 75, and 100°C, respectively.

The entire reactor was placed in a Yamato DKN-600 mechanical convection oven (Santa Clara, CA). The oven served to maintain control of the reactor and gas temperature during experiments. Three J-type thermocouple probes (P/N TC-J-NPT-G-72-SMP, Omega Engineering Inc., Stamford, CT) measured gas temperatures at the reactor inlet, reactor outlet and in the oven chamber directly above the reactor apparatus.

The test gas was provided by a compressed gas cylinder of 1009 ppmv propane ($\pm 2\%$) in a balance of hydrocarbon-free air containing less than 0.1 ppmv total hydrocarbons (Linde Gas Comp., Madison, WI). Trace quantities of acetone, acetaldehyde, methane,

ethane, isobutane, and n-butane were detected in the feed stream. Gas flowrates were controlled by MKS 1179A mass flow controllers (MFC) (MKS Instruments, Wilmington, MA).

The reactor effluent was sampled every 10 min via a six-way valve with a 25- μ l gas sampling loop connected to a gas chromatograph (Shimadzu GC-2010, Japan). The GC-2010 was equipped with a thermal conductivity detector (TCD) and a flame ionization detector (FID) positioned in series. The capillary column was a 30 m x 0.32 mm Rt-QPLOT (Fused Silica PLOT) from Restek Corp. (Bellefonte, PA). The GC oven temperature was maintained at 125°C.

4.2.3 Experimental Conditions

All experiments were performed at a flowrate of 200 mL/min and 50% relative humidity (RH). To achieve this RH, the feed gas flow was split with a portion of the flow passing through a sparger to attain the desired relative humidity (RH) in the reactor inlet. Relative humidity was monitored upstream of the photoreactor with a humidity probe (P/N: HMP 235, Vaisala Inc., Woburn, MA). LabviewTM software and data acquisition hardware (National Instruments, Austin, Texas) using a proportional-integral-derivative (PID) algorithm was employed to monitor the RH in the system and as well to control the MFCs in order to adjust the flow split to maintain the target of 50% RH.

Three reaction temperatures were tested sequentially. The oven temperature was ramped up to 50°C over 5 min, after which the temperature was sustained at 50°C for 65 min. This was followed by a 5-min ramp and 65-min hold time at 75°C followed by a similar ramp

to 100°C. Gas samples of the reactor effluent were acquired every 10 min during an experiment. (Testing of the ZrO₂/TiO₂ catalyst was also conducted following a reverse temperature profile (i.e. 100, 75, 50°C) with no statistical difference in results.) Additionally, experiments to generate data suitable for detailed kinetic analysis were performed at 35, 50, 75 and 100°C and at flowrates of 50, 100, 150, 200 and 250 mL·min⁻¹. Maximum temperatures used in this study did not exceed 100°C to insure the mechanical/material integrity of reactor components, namely the UV lights and electrical wiring.

4.3 Results and Discussion

4.3.1 Catalyst Characterization

The TiO₂, SiO₂/TiO₂ and ZrO₂/TiO₂ catalysts synthesized in this study had specific surface areas of 119, 350, and 231 m²·g⁻¹, respectively, as determined by Brauner-Emmett-Teller (BET) N₂ adsorption at 77K. The increase in surface areas of the binary materials was a function of the different particle sizes of the oxides and the dissimilar boundaries present in the films when sintering [27]. The BET specific surface area of all 21 catalysts is shown in Figure 4.1. Addition of the metals generally promoted the sintering process as 14 of the 18 metal modified catalysts decreased in surface area. Some metals decreased the surface area more than others, but the effect of a metal was not consistent from TiO₂ to Z/T to S/T. Similarly, Sakthivel et al. [28] found the addition of Au, Pd and Pt to Degussa P-25 photocatalysts caused the catalyst surface area to decrease, however, the degree to which the surface area decreased did vary substantially from metal to metal. The Z/T photocatalysts showed the highest sensitivity to metal addition with five of the six m-Z/T catalysts

decreasing more than 20%. The m-T catalysts had the smallest percent change in surface area.

The average Barret-Johner-Halenda (BJH) pore size of the catalysts is given in Figure 4.2. The pore sizes of the m-T catalysts were distinctly larger than those of the plain TiO₂. The pore sizes of the m-S/T photocatalysts did not vary significantly from the unmodified S/T film while the m-Z/T catalysts exhibited smaller pore sizes than the Z/T catalyst. The pore size of the Au-Z/T catalyst was drastically different from the other materials with an average pore size of ≤ 18 Å, which classified this film as microporous [29]. All other films tested contained both mesopores and micropores.

The mass of catalyst coated per glass ring was assessed by inductively coupled plasma spectroscopy following digestion of the catalyst coating [19]. The average mass of the coating per ring was $0.12 \text{ mg} \pm 0.036$, $0.21 \text{ mg} \pm 0.059$, and $0.15 \text{ mg} \pm 0.010$ for the TiO₂, S/T, and Z/T groups of rings, respectively. All ring supports were coated under similar conditions, but the viscosity (although unmeasured) of the sols was visibly different. The m-S/T sols were distinctly thicker than the m-TiO₂ or m-Z/T sols, possibly because of more aggregation in the S/T sols resulting from a lesser degree of charge stabilization. The isoelectric point (IEP) of SiO₂ is approximately 2.5 while the IEP of titania is close to 6. The sols were stabilized at a $\text{pH} \leq 2.0$ and the S/T sols maintained a stable suspension for a few days after which a gel layer formed in the bottom of the sol. This gel was easily re-suspended with vigorous stirring and again the stability was retained for a few days. The S/T coatings were also noticeably thicker on the glass supports and more opaque. The importance of the

mass deposited was paramount when interpreting conversion data for kinetic analysis and determination of reaction rate coefficients.

Representative x-ray diffraction (XRD) spectra of the TiO_2 , S/T, and Z/T catalysts are shown in Figure 4.3. All peaks are anatase reflections except for the rutile reflection at $\sim 27.5^\circ$ forming in the TiO_2 catalyst. These findings agree well with the data presented by Fu et al [27]. It is theorized that the dissimilar boundaries between the titania and the silica or zirconia inhibits densification and crystallite growth. Only the anatase phase of titania was detected in the S/T and Z/T catalysts, regardless of metal addition. The m- TiO_2 catalysts averaged 15% rutile $\pm 6\%$. There were no diffraction patterns characteristic of the precious metals in the XRD patterns.

Crystallite size as determined by peak broadening using the Scherrer equation confirm that crystallite growth in the S/T and Z/T photocatalysts was slowed. Average crystallite size for the TiO_2 , S/T and Z/T groups was 5.3 ± 0.41 , 3.7 ± 0.2 and 3.9 ± 0.45 nm, respectively.

4.3.2 Photocatalytic Results

Experiments were performed to characterize reactant gas concentrations associated with increased temperatures and photolysis. Temperature alone did not discernibly affect the propane effluent from the reactor while operation of the reactor while the lamps were energized decreased the propane concentration by $2.1\% \pm 0.2\%$. The trace quantities ($<0.5 \mu\text{mol-L}^{-1}$) of acetone and acetaldehyde detected during temperature and photolysis experiments were higher than the levels measured in the influent, with the concentration of each contaminant increasing by almost a factor of two as reactor temperature increased to

100°C. Given that photolysis of propane requires $\lambda < \sim 157$ nm [30], the observed increase in acetone and acetaldehyde concentrations as temperature increased is attributed to desorption from (or lack of adsorption to) reactor components at elevated temperatures. Conversely, the concentrations of the other trace contaminants present in the feed stream did not change during these experiments. These differences in behavior were attributed to the presumed differences in adsorption affinity of acetone and acetaldehyde versus the light alkanes.

Conversion of propane over the complete suite of catalyst materials at the three reaction temperatures is shown in Figure 4.4. It is immediately apparent that the Z/T and Pt-Z/T photocatalysts were the most active materials for conversion of propane. The Z/T material provided nearly 20% better conversion than the next best performer and over 40% better than the unmodified TiO₂ and S/T photocatalysts. These data suggest the photocatalyst surface area is not the determining factor for conversion of propane considering that the surface area of S/T is approximately 40% larger than the Z/T photocatalyst and more than double the surface area of the TiO₂ photocatalyst. Other characteristics of the films, such as the nature and quantity of surface acid groups, could be the key features influencing the photocatalytic activity. Similarly, Fu et al. found that a Z/T mixture outperformed both TiO₂ and S/T for conversion of ethylene [27].

Generally, the addition of 1 wt % precious metal to the thin films was detrimental to the photocatalytic activity. Studies of platinum loading for photocatalysis of other VOCs have reported some loss in photocatalytic activity for platinum loadings of 0.5 to 0.1 wt % at temperatures below 60°C, although the rate of photooxidation significantly increased for

acetaldehyde, acetone, ethanol and ethylene at temperatures between 60°C and 140°C [14,17,21,31]. Our results provide little evidence that the addition of precious metals increased the conversion of propane at the temperatures tested. In fact, only Au-Z/T yielded a higher conversion of propane at 100°C compared to 50°C. By and large, observations demonstrate an inverse relationship between conversion and temperature, with the conversion of propane decreasing as the temperature increased. Two phenomena could explain these observations: 1) As temperature in the reactor increased, the UV output of the lights decreased causing a decrease in catalyst photoactivation. 2) Desorption of propane from the catalyst surface at elevated temperatures may reduce the interaction time of the gaseous propane with photoactive species on the catalyst surface.

The palladium, rhodium and ruthenium modified materials had very little PCO activity (except for Rh-ZT). For the most part, these metals appeared to quench the PCO reaction. A possible reason for their inactivity in these tests was that these metals were more prone to oxidation during the sintering process (the Pd catalysts had a distinct yellow hue indicative of Pd^{+2}), leading to the formation of metal ions that may act as scavenging sites for electrons when under UV illumination.

Figure 4.5 presents the mineralization of propane for the photocatalysts tested where $\text{MR} = [\text{CO}_2\text{-generated}] / [\Delta\text{C}_3\text{H}_8]$, where $\Delta\text{C}_3\text{H}_8$ is the difference in propane concentration between the inlet and outlet of the reactor. As stated earlier, we previously reported ~80% mineralization of propane over our Z/T thin films, but at irradiance of 2.1 mW-cm^{-2} . In this study, several of the photocatalysts yielded greater than 90% mineralization as a result of increased irradiance and possibly improved degradation of intermediate

compounds at the elevated temperatures. Evaluation of the data in Figure 4.5 indicates that mineralization may have increased for the gold, platinum and rhodium doped materials at 100°C, but not at 75°C when compared to 50°C. This is an indication that these materials, although detrimental to propane oxidation, promoted oxidation of intermediate species to CO₂ when temperatures were sufficient to thermally activate the metals, whereas mineralization of propane over the unmodified photocatalysts was relatively constant or slightly decreased as the temperature increased from 50 to 75 to 100°C.

Interestingly, the ruthenium photocatalysts have little activity for propane oxidation and no CO₂ was detected in the effluent when using the Ru-T and Ru-S/T. Recall that Rodemerck et al. [24] identified a 3 wt % Ru thermal catalyst supported on TiO₂ as the most active material they studied for low temperature conversion of propane. The 1 wt % loading in this study may not have been high enough and coupled with a space-time (mass of catalyst / molar flowrate) that was two orders of magnitude smaller may explain why we did not observe a substantial catalytic effect from the metal. On the other hand, the 1 wt % loading caused a decrease in PCO activity of the films and a higher loading would likely induce an even more severe reduction in PCO activity resulting from blockage of UV by the metal islands or enhanced charge carrier recombination [11,32].

Mineralization can be a good indication of the quantity of intermediates produced during the photocatalytic reaction. Figures 4.6 and 4.7 present the concentration of acetone and acetaldehyde in the reactor effluent, respectively. For nearly every material studied, the amounts of both species in the effluent increased as temperature increased, except for two cases where acetone generation either remained nearly constant (Ru-S/T) or decreased (Ru-

Z/T) with increasing temperature (Fig. 4.6). As evidenced by the photolysis experiments, desorption of these compounds from reactor components occurred at the elevated temperatures. Additionally, acetone and acetaldehyde are both polar compounds, therefore they likely adsorbed more strongly to the photocatalyst surface than propane. Furthermore, these compounds would also be more soluble in surface adsorbed water. As the reactor temperature increased, the gas-solid equilibrium for these compounds would shift towards the gas phase driving the compounds off of the surface.

As a whole, the acetone levels measured in PCO experiments with the various materials varied only slightly from the quantities detected during photolysis experiments, with the exception of three materials (Z/T, Au-Z/T, and Pt-Z/T) at 50°C, where acetone concentrations were approximately one-half of that in the photolysis experiments. Previous studies have shown our $\text{ZrO}_2/\text{TiO}_2$ thin films to be very active for the oxidation of acetone vapor [33]. The fact that there was little variation in the acetone concentration suggests that little or no acetone was formed during PCO over our films or at a minimum, the rate of production from the PCO of propane was approximately equal to the rate of acetone photooxidation. This is a significant observation when one considers that acetone is purported to be the principal intermediate of propane photooxidation [3,5,6].

In contrast to the acetone data, acetaldehyde quantities were generally lower than those measured in photolysis experiments and operation at 50°C (highest irradiance) resulted in the lowest acetaldehyde concentrations in the effluent (Fig. 4.7). From these data it appears that little acetaldehyde was formed during the PCO of propane over the majority of the films tested. Previously we reported that the PCO of propane over our Z/T thin films did not

produce any detectable quantities of acetaldehyde [25]. Thus the decrease in acetaldehyde quantities was due to photooxidation of the trace quantities present in the influent.

Decreasing the level of acetaldehyde in the effluent was a primary goal of this study; therefore, these results in conjunction with a catalyst's performance for conversion of propane will weigh heavily on the selection of the optimal catalyst.

We must also note that the quantities of methane and ethane in the effluent were constant for all of the materials tested except for the Au- and Pt-loaded materials. Methane concentrations increased up to 5 times the quantity in the inlet when the Au-S/T photocatalyst was used. The Au-TiO₂, Au-Z/T, Pt-S/T and Pt-TiO₂ materials yielded between 1.5 and 2 times the levels of methane in the influent. The Au-S/T material also exhibited a 20% increase in ethane generation and the other gold-modified materials showed roughly a 10% increase. The unique catalytic properties of gold nanoparticles have garnered a fair amount of interest in recent years. Our results suggest that a secondary reaction associated with nanoparticulate gold in photocatalytic thin films may be the cracking of higher molecular weight alkanes, thus resulting in the formation of methane and ethane. Trace quantities of propylene were also generated in some of the photocatalysis tests, but only over the Ag-TiO₂, Ag-Z/T, Au-TiO₂, Au-Z/T and Rh-Z/T materials.

4.3.3 Influence of Temperature on Irradiance

It is well established that the irradiance of a fluorescent UV lamp decreases as the temperature increases [14,19,34]. To quantify the influence of irradiance on propane destruction we measured the irradiance at the three reaction temperatures. Previous

investigations [35,36] have demonstrated a one-half or first-order relationship between the irradiance and the photocatalytic reaction rate (equation 1)

$$k_a = k_a'(I)^\alpha \quad (4.1)$$

where k_a is the observed reaction rate constant, k_a' is the actual reaction rate constant, I is irradiance ($\text{mW}\cdot\text{cm}^{-2}$) and α is the exponential factor. Light-rich systems have previously been defined as having irradiance greater than $20 \text{ mW}\cdot\text{cm}^{-2}$ [11].

A logarithmic transform of Eq. 4.1 yields

$$\ln k_a = \ln k_a' + \alpha \ln I \quad (4.2)$$

A plot of $\ln k_a$ versus $\ln I$ should yield a straight line with a slope equal to the magnitude of α .

Values for k_a are determined using a pseudo first-order reaction rate constant with the Z/T_{catalyst}

$$k_a = (\dot{V} / W) \ln[1/(1 - f_a)], \quad (4.3)$$

where the units for k_a are $\text{L g}^{-1} \text{ s}^{-1}$, \dot{V} is the volumetric flowrate of propane (L s^{-1}), W is catalyst mass (g), and f_a is the fractional conversion given as $1 - (C_{\text{out}} / C_{\text{in}})$ where C_{in} and C_{out} are the propane concentrations entering and leaving the reactor, respectively.

Figure 4.8 displays the results for determination of α from experiments with 2, 4, 6, and 8 lamps operating in the reactor at four temperatures. The large error bars in the lower UV values derive from the standard deviation of the eight measurements when only two lamps were energized. Alpha as determined from a combined data set equaled 0.94 ± 0.10 . The value for α indicates the system was light poor. This was expected based on the criteria for light-rich systems. The dashed lines in Figure 4.8 represent the linear regression fit to each individual data set. As derived from the dashed lines, the values of α increase as the

reaction temperature increases (note the shift in the slope of the dashed lines as the temperature changes), indicating that less UV energy is required to achieve the same reaction rate at higher temperatures. From these observations, one can conclude that increasing the reactor temperature did improve the overall rate of the reaction to some degree.

4.3.4 Photocatalytic Reaction Rates

Reaction rates for propane conversion over the 21 catalysts, as calculated by Eq. 4.3 and normalized to average reactor irradiance using Eq. 4.1, are shown in Figure 4.9. Reaction rate constants provide a better analysis of catalytic activity because the results are normalized to the irradiance and the mass of the photocatalyst in the reactor. A direct relationship is observed between reaction rates and reactor temperature for most of the photocatalysts evaluated. However, the absence of an increase in reaction rates with any of the metal modified photocatalysts suggests the metals are not appreciably active as thermal catalysts for propane oxidation at the temperatures studied. The unmodified Z/T photocatalyst had the largest reaction rate constant at each of the three temperatures.

This increase in the reaction rate may be due to a shift in the adsorption – desorption equilibrium of propane, water and other reactants in the feed stream freeing up more reactive sites for oxidation of propane. Although the relative humidity of the inlet stream was held constant, the amount of water adsorbed on the photocatalyst surface could vary significantly as the reactor temperature increased. Surface coverage by water is documented as having a significant impact on PCO reactions [4,15,25,37,38]. Water molecules may trap positive holes forming hydroxyl radicals that can effectively oxidize reactants. Yet, if the water

content is above an optimal level, 1% at 130°C as suggested by Haaglund et al. [4] for propane oxidation, the excess water molecules may prevent reactants from interacting with the active species at the catalyst surface. Our condition of 50% RH prior to the inlet is equivalent to approximately 1.5% water vapor which provides sufficient water for nearly complete surface coverage at 295 K [39]. This water content could have blocked propane from reacting with active sites on the surface. However, as the reactor temperature increased, some of the water would be driven off of the surface, which in turn would expose more active sites and result in the observed higher reaction rates.

The platinized photocatalysts performed the best of all the metal-loaded photocatalysts. This observation was not entirely unexpected since platinization of photocatalysts has proven to be beneficial in numerous other photocatalytic investigations. Platinum has the highest work function of the precious metals, leading to the largest Schottky Barrier at the metal-semiconductor interface; thus recombination should decrease and charge separation should be enhanced [39]. However, since the unmodified photocatalysts had the highest activity for propane oxidation, the metal loadings did not produce the desired effect. There are at least three plausible reasons for this observation: (1) As stated previously, our weight percent loading may not have been optimized to successfully initiate a thermal catalytic effect. (2) At high metal loadings, the large number of nanometal islands in the film may cause a decrease in electron density due to attraction by numerous metal islands and thus hindered charge separation [32]. (3) The metal islands could have shadowed the photocatalyst material, preventing it from receiving sufficient illumination and nullifying any beneficial effect of the metals. However, others have shown that such an effect was not

significant until metal weight loading exceeded 3 wt %, at which point surface coverage surpassed 10% [40].

To further evaluate the influence of material and temperature on the reactivity of propane in the photocatalytic reaction, we performed a series of experiments at multiple flowrates (50 – 250 ml·min⁻¹) through the reactor to produce data sufficient for kinetic analysis using a Langmuir-Hinshelwood-Hougen-Watson (LHHW) model. The LHHW rate expression incorporates a term for the adsorption of the reacting contaminant onto the surface of the photocatalyst. Use of this model to fit reaction data lends insight into how changes in temperature and catalyst material affect the gas-solid interaction. Ultimately, one desires a data set that encompasses a space-time range with conversion values between 10 and 95% [41]. Our reactor configuration and the generally low reactivity of propane limited the data to a range between 20 and 90% conversion. Therefore, the error values are appreciably high, but the data are useful for a qualitative analysis.

Table 4.1 presents the results of non-linear regression analysis of propane conversion data for TiO₂, S/T, Z/T at 35°C and Z/T at 50, 75, and 100°C. Reaction rates of the TiO₂, S/T, and Z/T materials are similar, but as shown in previous results, the Z/T is 12.5% and 33.3% more active than T and S/T photocatalysts, respectively, at 35°C. One might expect the adsorption equilibrium constants to fall in order according to the surface area of the materials; however, this was not observed. The surface area of the Z/T material was roughly two times the surface area of the TiO₂, yet the estimated adsorption coefficient of the Z/T was half that of the TiO₂ material. This observation may be an indication that attributes other than

surface area (i.e. surface acidity) may play an important role in photocatalysis and the gas-solid interaction [42].

Evaluation of the reaction rate constants at the four temperatures reveal a dramatic increase in the reaction rate constant as temperature increased and a corresponding decrease in adsorption equilibrium coefficient. So, even though the rate increased by several orders of magnitude, the lack of affinity for the surface at the higher temperatures was detrimental to the conversion of propane. These observations along with other data presented in this paper denote the complexity of PCO reactions and the difficulty in optimizing a reaction pathway.

References

- [1] USEPA, Protection of Stratospheric Ozone, 40 CFR Parts 9 and 82, 94 A.D., p. IX. i.
- [2] N.A.Kelly, T.Y.Chang, *Atmos. Environ.* 33 (1999) 2101-2110.
- [3] N.Djaghri, M.Formenti, F.Juillet, S.J.Teichner, *Faraday Discuss.* (1974) 185-193.
- [4] C.Hagglund, B.Kasemo, L.Osterlund, *J. Phys. Chem. B* 109 (2005) 10886-10895.
- [5] T.Tanaka, K.Teramura, T.Yamamoto, S.Takenaka, S.Yoshida, T.Funabiki, J. *Photochem. Photobiol. A* 148 (2002) 277-281.
- [6] K.Wada, K.Yoshida, T.Takatani, Y.Watanabe, *Appl. Catal. A* 99 (1993) 21-36.
- [7] K.R.Darnall, A.C.Lloyd, A.M.Winer, J.N.Pitts, *Environ. Sci. Technol.* 10 (1976) 692-696.
- [8] R.A.Cox, R.G.Derwent, M.R.Williams, *Environ. Sci. Technol.* 14 (1980) 57-61.
- [9] T.Tanaka, T.Ito, S.Takenaka, T.Funabiki, S.Yoshida, *Catal. Today* 61 (2000) 109-115.
- [10] C.T.Brigden, S.Poulston, M.V.Twigg, A.P.Walker, A.J.J.Wilkins, *Appl. Catal. B* 32 (2001) 63-71.
- [11] O.Carp, C.L.Huisman, A.Reller, *Prog. Solid State Chem.* 32 (2004) 33-177.
- [12] M.A.Fox, M.T.Dulay, *Chem. Rev.* 93 (1993) 341.
- [13] J.M.Herrmann, *Catal. Today* 53 (1999) 115-129.
- [14] X.Z.Fu, L.A.Clark, W.A.Zeltner, M.A.Anderson, *J. Photochem. Photobiol. A* 97 (1996) 181-186.
- [15] T.N.Obee, S.O.Hay, *Environ. Sci. Technol.* 31 (1997) 2034-2038.
- [16] T.Sano, N.Negishi, K.Uchino, J.Tanaka, S.Matsuzawa, K.Takeuchi, *J. Photochem. Photobiol. A* 160 (2003) 93-98.
- [17] A.V.Vorontsov, E.N.Savinov, Z.S.Jin, *J. Photochem. Photobiol. A* 125 (1999) 113-117.
- [18] A.V.Vorontsov, V.P.Dubovitskaya, *J. Catal.* 221 (2004) 102-109.
- [19] M.E.Zorn, D.T.Tompkins, W.A.Zeltner, M.A.Anderson, *Environ. Sci. Technol.* 34 (2000) 5206-5210.

- [20] X.Z.Fu, W.A.Zeltner, M.A.Anderson, Appl. Catal. B 6 (1995) 209-224.
- [21] J.C.Kennedy, A.K.Datye, J. Catal. 179 (1998) 375-389.
- [22] Y.Yazawa, N.Takagi, H.Yoshida, S.Komai, A.Satsuma, T.Tanaka, S.Yoshida, T.Hattori, Appl. Catal. A 233 (2002) 103-112.
- [23] Y.Yazawa, H.Yoshida, T.Hattori, Appl. Catal. A 237 (2002) 139-148.
- [24] U.Rodemerck, D.Wolf, O.V.Buyevskaya, P.Claus, S.Senkan, M.Baerns, Chem. Eng. J. 82 (2001) 3-11.
- [25] T.M.Twesme, D.T.Tompkins, M.A.Anderson, T.W.Root, Appl. Catal. B 64 (2006) 153-160.
- [26] Q.Y.Xu, M.A.Anderson, J. Mater. Res. 6 (1991) 1073-1081.
- [27] X.Z.Fu, L.A.Clark, Q.Yang, M.A.Anderson, Environ. Sci. Technol. 30 (1996) 647-653.
- [28] S.Sakthivel, M.V.Shankar, M.Palanichamy, B.Arabindoo, D.W.Bahnmann, V.Murugesan, Water Res. 38 (2004) 3001-3008.
- [29] E.P.Barrett, L.G.Joyner, P.P.Halenda, J. Am. Chem. Soc. 73 (1951) 373-380.
- [30] S.M.Wu, J.J.Lin, Y.T.Lee, X.Yang, J. Chem. Phys. 111 (1999) 1793-1796.
- [31] J.L.Falconer, K.A.Magrini-Bair, J. Catal. 179 (1998) 171-178.
- [32] M.Sadeghi, W.Liu, T.G.Zhang, P.Stavropoulos, B.Levy, J. Phys. Chem. 100 (1996) 19466-19474.
- [33] M.E.Zorn, D.T.Tompkins, W.A.Zeltner, M.A.Anderson, Appl. Catal. B 23 (1999) 1-8.
- [34] S.B.Kim, H.T.Hwang, S.C.Hong, Chemosphere 48 (2002) 437-444.
- [35] A.Mills, J.S.Wang, Int. J. Res. Phys. Chem. Chem. Phys. 213 (1999) 49-58.
- [36] D.F.Ollis, E.Pelizzetti, N.Serpone, Environ. Sci. Technol. 25 (1991) 1522-1529.
- [37] L.X.Cao, Z.Gao, S.L.Suib, T.N.Obee, S.O.Hay, J.D.Freihaut, J. Catal. 196 (2000) 253-261.
- [38] J.M.Coronado, M.E.Zorn, I.Tejedor-Tejedor, M.A.Anderson, Appl. Catal. B 43 (2003) 329-344.
- [39] A.L.Linsebigler, G.Lu, J.T.J.Yates, Chem. Rev. 95 (1995) 735.

- [40] I.M.Arabatzis, T.Stergiopoulos, D.Andreeva, S.Kitova, S.G.Neophytides, P.Falaras, J. Catal. 220 (2003) 127-135.
- [41] C.G.Hill Jr., An Introduction to Chemical Engineering Kinetics & Reactor Design, Wiley, New York, 1977.
- [42] M.D.Hernandez-Alonso, I.Tejedor-Tejedor, J.M.Coronado, J.Soria, M.A.Anderson, Thin Solid Films 502 (2006) 125-131.

Tables

Table 4.1 Parameter estimates obtained from non-linear regression analysis of kinetic data when fit to a first order LHHW model.

Catalyst	Reaction Rate Constant ^a (mol g ⁻¹ s ⁻¹)	Adsorption Equilibrium Coefficient (L mol ⁻¹)	R ²
TiO ₂ , T=35°C	$3.2 \times 10^{-6} \pm 5.8 \times 10^{-7}$	$4.1 \times 10^4 \pm 2.2 \times 10^4$	0.99
SiO ₂ /TiO ₂ , T=35°C	$2.7 \times 10^{-6} \pm 1.3 \times 10^{-6}$	$5.5 \times 10^4 \pm 9.6 \times 10^4$	0.99
ZrO ₂ /TiO ₂ , T=35°C	$3.6 \times 10^{-6} \pm 1.5 \times 10^{-6}$	$1.9 \times 10^4 \pm 1.6 \times 10^4$	0.99
ZrO ₂ /TiO ₂ , T=50°C	$1.3 \times 10^{-4} \pm 5.5 \times 10^{-6}$	150 ^b	0.98
ZrO ₂ /TiO ₂ , T=75°C	$1.1 \times 10^{-2} \pm 1.7 \times 10^{-3}$	1.6 ^b	0.95
ZrO ₂ /TiO ₂ , T=100°C	$1.9 \times 10^{-2} \pm 5.4 \times 10^{-3}$	1.1 ^b	0.77

^aReaction rate constants have not been adjusted for the influence of temperature on reactor irradiance. ^bAdsorption equilibrium constant was statistically indeterminate. The value shown is the initial estimate for K_A that yielded the best fit to the data set.

Figures

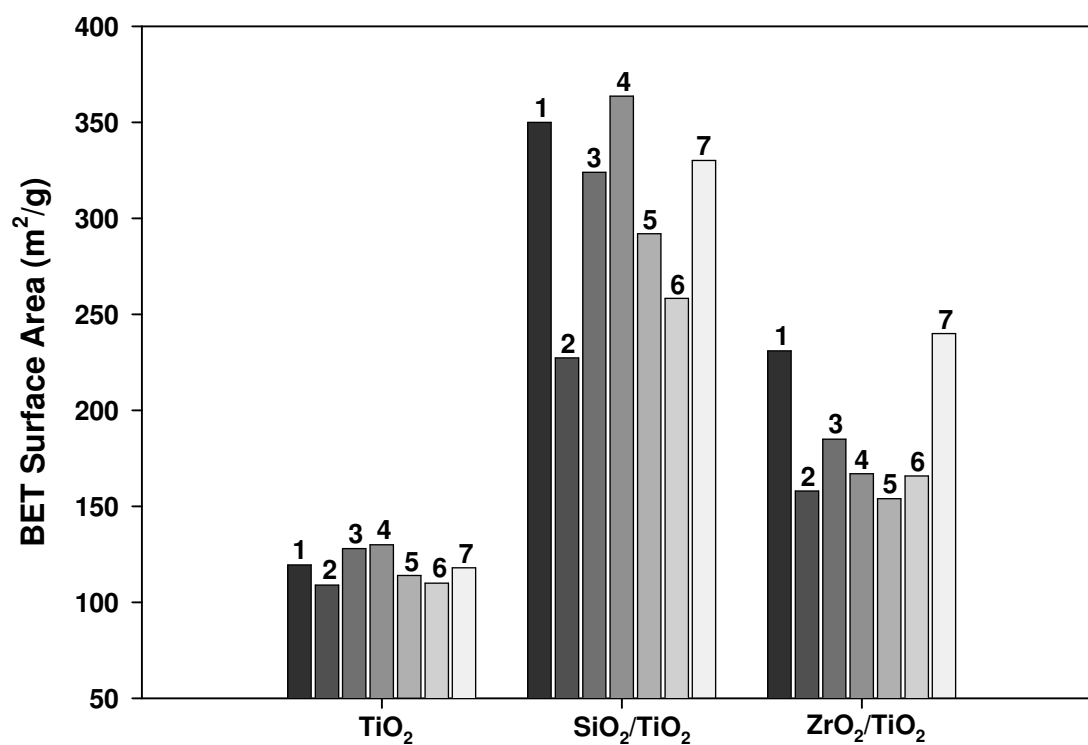


Figure 4.1 BET surface area of the catalyst materials. Numbers correspond to modification of the photocatalyst listed on the abscissa with a given metal. **1** – unmodified, **2** – Ag, **3** – Au, **4** – Pd, **5** – Pt, **6** – Rh, **7** – Ru. ($n=1$, i.e. single sample)

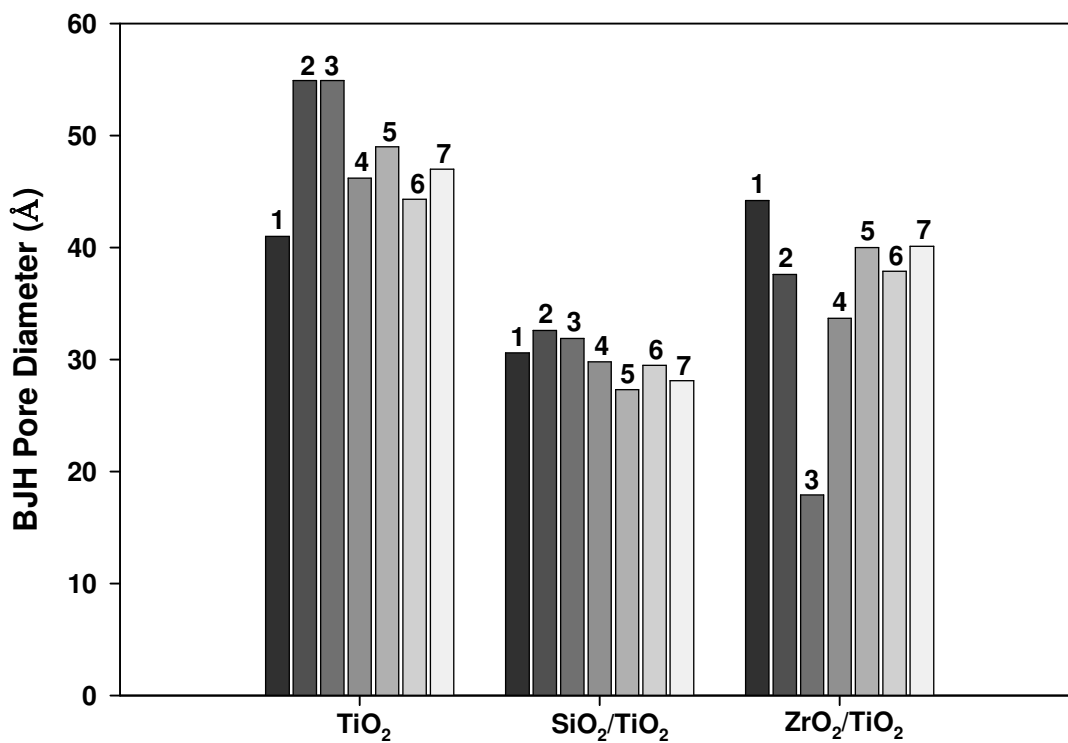


Figure 4.2 BJH pore size of the catalyst materials. Numbers correspond to modification of the photocatalyst listed on the abscissa with a given metal. **1** – unmodified, **2** – Ag, **3** – Au, **4** – Pd, **5** – Pt, **6** – Rh, **7** – Ru. ($n=1$, i.e. single sample)

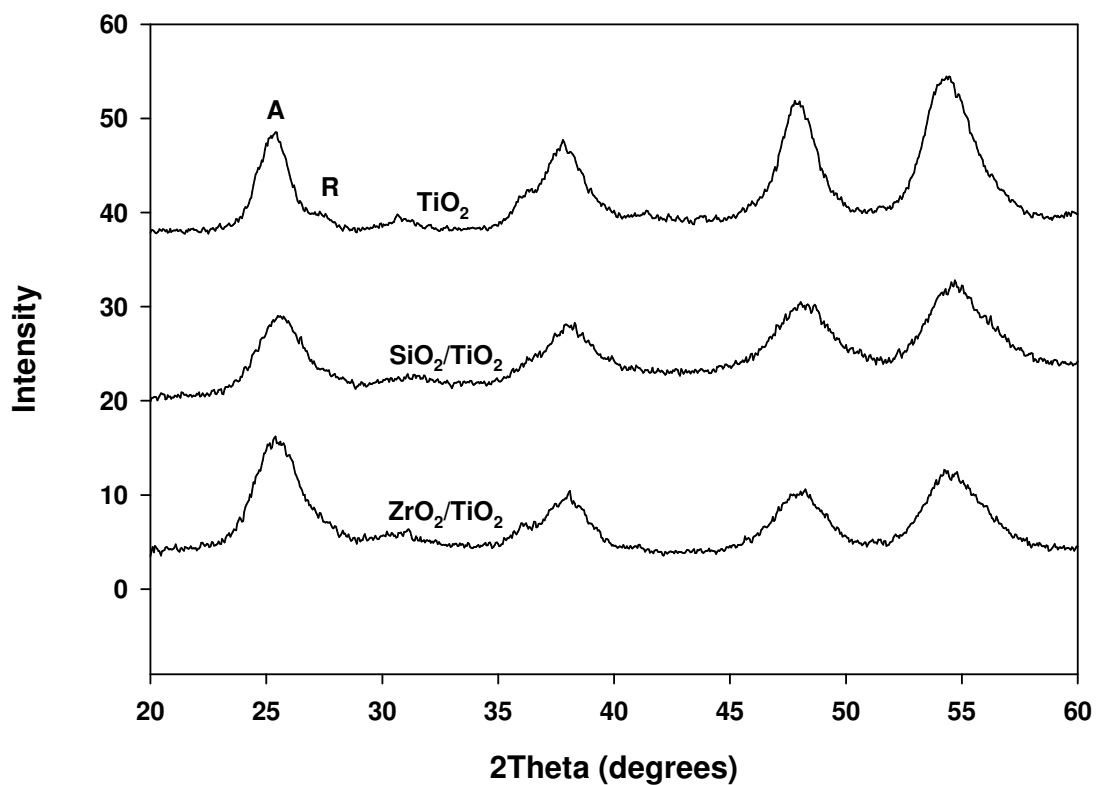


Figure 4.3 XRD patterns of TiO_2 , $\text{SiO}_2/\text{TiO}_2$ and $\text{ZrO}_2/\text{TiO}_2$ powders from sintered xerogels. A – indicates the (101) anatase reflection and R – indicates the (110) rutile peak.

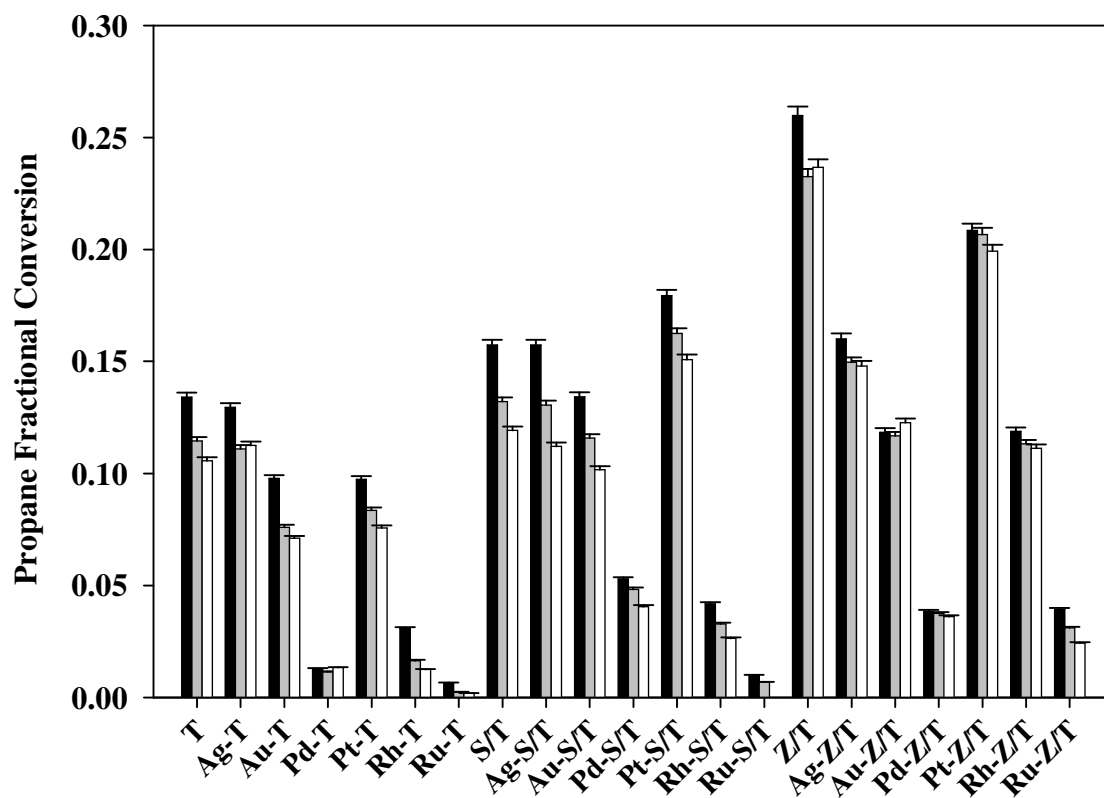


Figure 4.4 Fractional conversion of propane at 50% RH and reactor temperatures of 50°C (■), 75°C (▣), and 100°C (□). Error bars represent the 95% confidence level.

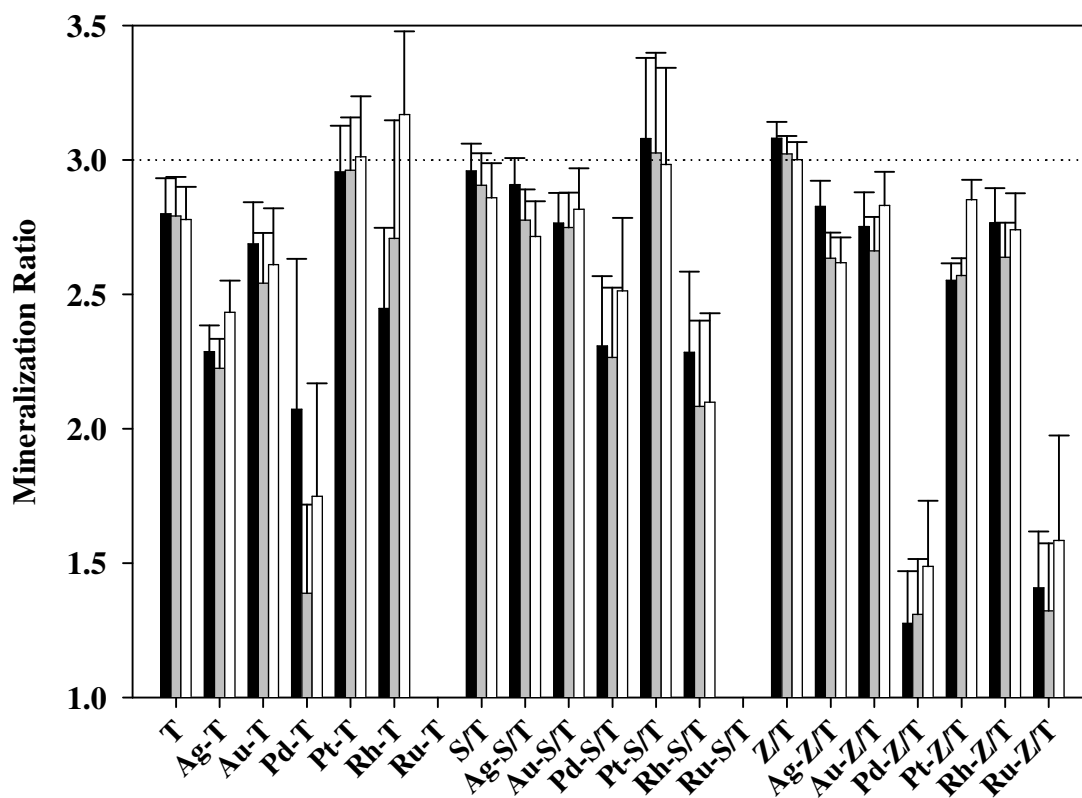


Figure 4.5 Mineralization ratio (MR) for conversion of 1000 ppmv propane at 50% RH and reactor temperatures of 50°C (■), 75°C (▒), and 100°C (□). The MR for Ru-T and Ru-ST was 0.0. The theoretical mineralization ratio for propane is 3 as indicated by the dotted line. Error bars represent the 95% confidence level.

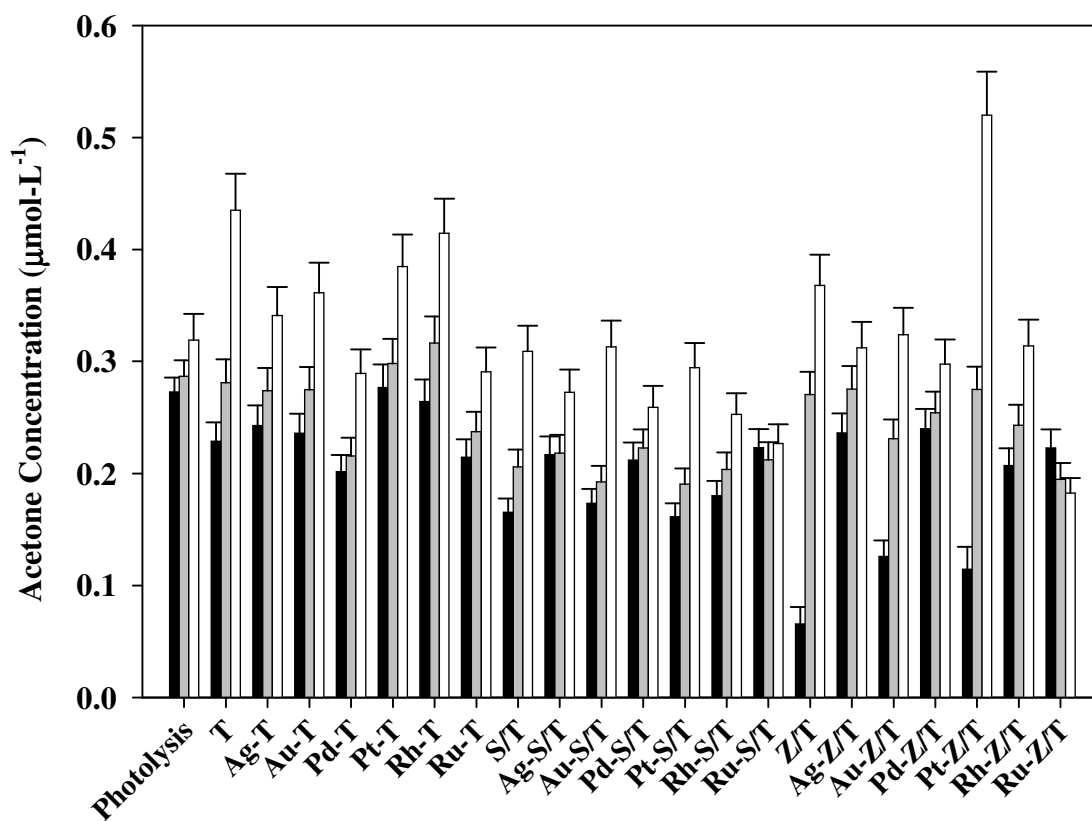


Figure 4.6 Effluent concentration of acetone during photocatalytic oxidation of 1000 ppmv ($80 \mu\text{mol}\cdot\text{L}^{-1}$) propane at 50% RH and reactor temperatures of 50°C (■), 75°C (■), and 100°C (□). Error bars represent the 95% confidence level.

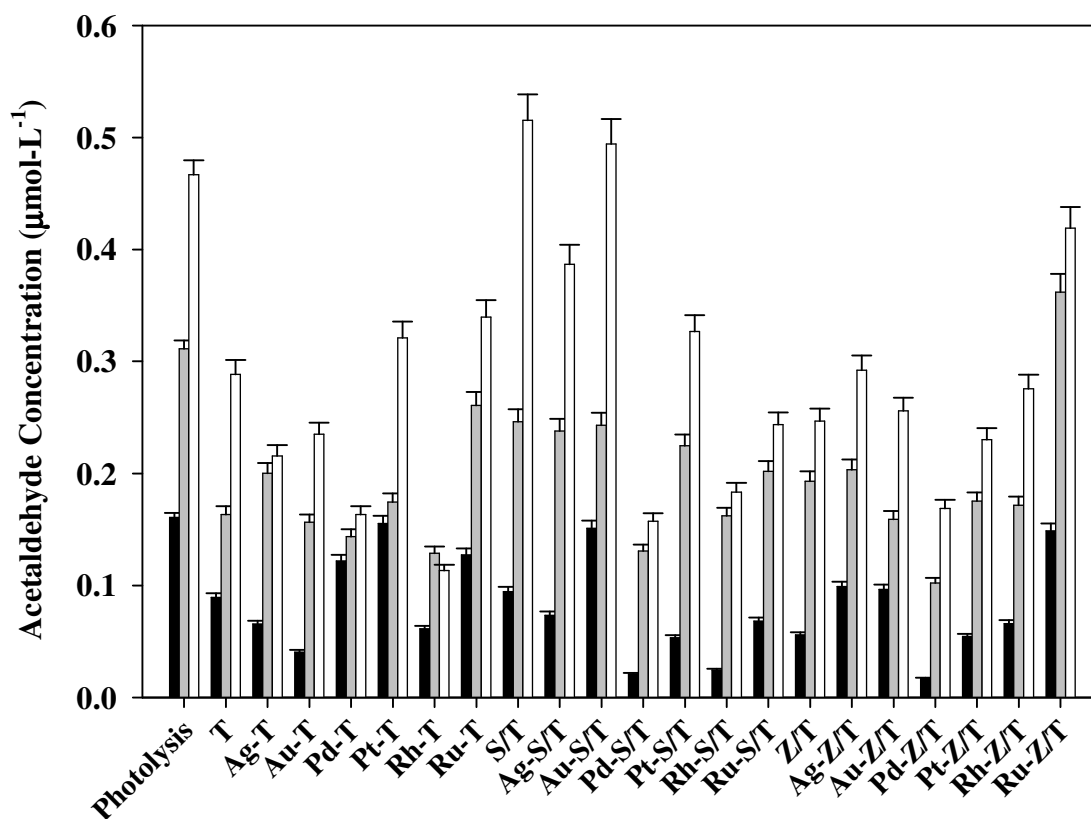


Figure 4.7 Effluent concentration of acetaldehyde during photocatalytic oxidation of 1000 ppmv ($80 \mu\text{mol}\cdot\text{L}^{-1}$) propane at 50% RH and reactor temperatures of 50°C (■), 75°C (■), and 100°C (□). Error bars represent the 95% confidence level.

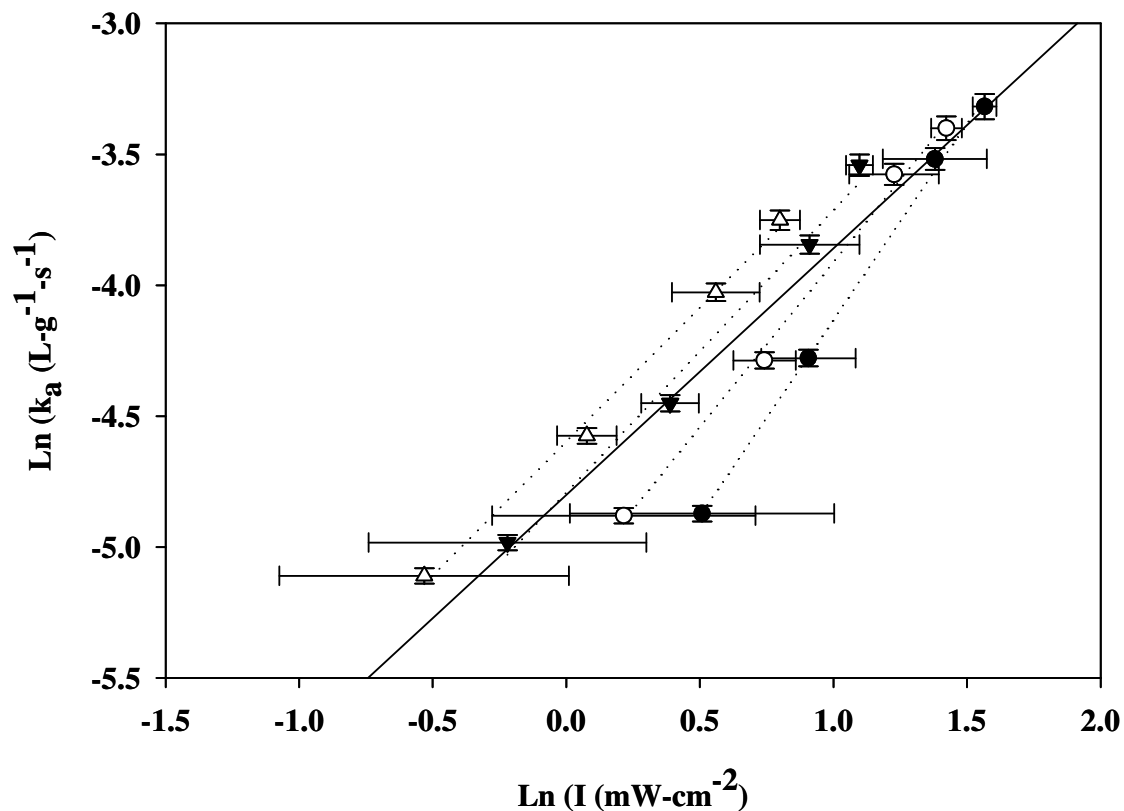


Figure 4.8 Dependence of propane oxidation on UV irradiance and reactor temperature, 1000 ppm propane and 50% RH. 35°C (●), 50°C (○), 75°C (▼), and 100°C (△). Solid black line is the linear least-squares fit of the combined data. Slope = 0.94, $R^2 = 0.95$. Dashed lines are the linear least squares fit of the individual data sets. X-error bars are based on an average of 8 irradiance measurements in the reactor. Y-error bars are based on an average of three replicates analyses.

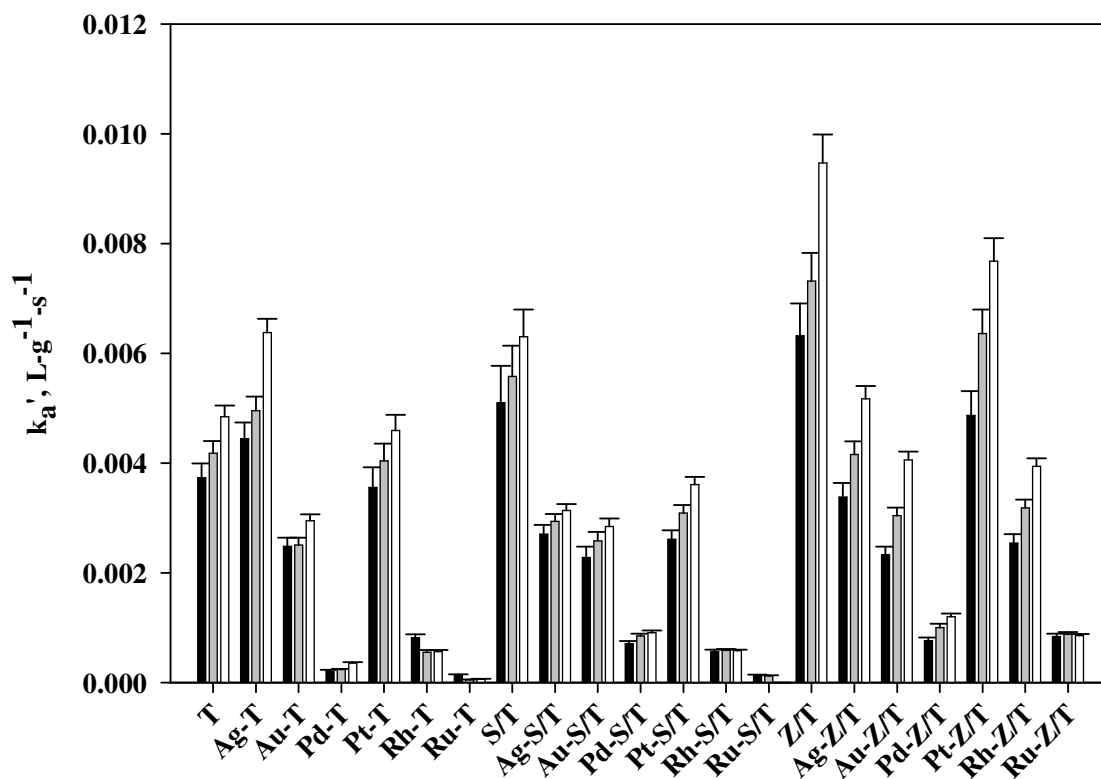


Figure 4.9 Pseudo-first order reaction rate constants for 1000 ppmv propane oxidation adjusted for irradiance according to Eq. 4.1. $\alpha = 0.94$. 50% RH and reactor temperatures of 50°C (■), 75°C (■), and 100°C (□). Error bars are based on propagation of the measurement uncertainties calculated for I , W , and f_a .

Chapter 5

Oxidation of Propane via Platinized Thin Film Photocatalysts: Relating Activity and Photoinduced Surface Potential via Atomic Force Microscopy

Abstract

Thin films of $\text{ZrO}_2/\text{TiO}_2$ were successfully synthesized containing low weight loadings of platinum and tested for oxidation of propane in a single-pass photocatalytic reactor. The photoactivity of the thin films was further characterized by AFM-SP measurements assessing the change in the electrostatic potential of the thin films between dark and illuminated conditions. Photocatalytic activity of the thin films decreased as the quantity of platinum loaded into the films increased between 0.001 wt % and 1 wt %. Surface potential measurements demonstrated a similar trend of decreasing change in potential with higher platinum loadings when heat conduction effects from the UV source were negated. Based on the demonstrated correlation between surface potential and photocatalytic activity, it is concluded that surface potential measurements may provide a means to quickly evaluate the photoactivity of thin film coatings for gas phase applications. Moreover, the capacity of surface potential measurements to monitor the decay of post-illumination film activity was reported and a dependence of the decay rate on the irradiance was observed.

5.1 Introduction

The addition of platinum into photocatalytic materials is a common approach for attempting to increase the rate of gas -phase photocatalytic reactions. Mostly owing to thermal catalytic effects, low platinum loadings (0.1% - 1%) have proven effective at improving reactivity when reaction temperatures exceed $\sim 80^{\circ}\text{C}$ [1-7]. However, in the case of propane, activation of a catalytic reaction using 1 wt % Pt loaded photocatalytic films was not observed at temperatures up to 100°C [8]. At higher loadings (>3 wt % Pt), less than 20% conversion was reported at 150°C [9] and only when reaction temperatures exceed 200°C has complete conversion been observed [10,11]. Furthermore, operation of a photocatalytic reactor at temperatures above 50°C is detrimental to the performance of the UV lights [8]; thus the benefit from thermal catalysis over a platinum modified photocatalyst needs to be significant in order to justify the elevated temperatures employed.

Several authors have reported that platinum loadings negatively affect the low temperature performance of photocatalysts [1,2,6,8,12]. However, some evidence suggests that small quantities (<0.1 wt %) of platinum may increase the charge carrier separation distance, thereby reducing recombination, providing a longer lifetime for electron hole pairs, and possibly enhancing photocatalytic activity [13]. Ultrafast laser spectroscopic methods are commonly used to probe the fundamentals of such charge carrier dynamics [14-17]; however, these techniques are of limited use for rapidly assessing photoactivity. In cases where the photocatalytic material can be deposited as a thin film, elucidation of the electronic properties is easily accomplished in aqueous phase photoelectrochemical (PEC) studies that allow direct measurement of photocurrent [18-20]. Unfortunately PEC techniques cannot be extended

to evaluation of gas-phase photocatalytic systems because of the difficulty of establishing a controlled current in the gas phase. Furthermore, the unique characteristics in aqueous systems (pH, double layer formation, O₂ limitations, etc.) and those in gaseous systems (surface coverage, O₂ excess, etc.) render it difficult to correlate the results of aqueous PEC studies to observed behaviors in gas phase systems (see Appendix A). We propose that surface potential measurements via atomic force microscopy may provide a straightforward means, akin to photocurrent measurement in PEC studies, in which to evaluate the electronic processes in photoactivated semiconductors.

Advances in atomic force microscopy techniques, specifically surface potential imaging, allow one to monitor the surface potential of photoactivated semiconductors [21-23]. Atomic Force Microscopy – Surface Potential (AFM-SP, also called Scanning Kelvin Force or Probe Microscopy) imaging maps the variation of the electrostatic potential across a sample through measurement of the contact potential between the probe tip and the sample surface. Contact potential is defined as the difference in work function (ϕ) between the probe tip and the sample surface. In a semiconductor, such as TiO₂, the work function is the difference between E_{vacuum} and the Fermi energy (E_F). When a photocatalyst is illuminated, excited electrons are elevated to the conduction band which results in a shift upward (higher potential) in the Fermi level of the TiO₂ [24]. Under constant illumination, the rate of charge carrier generation and the rate of recombination should reach steady state, establishing an elevated film potential relative to the potential of the film under dark conditions. Therefore, it stands to reason that the difference in potential between light and dark conditions should be

related to the activity of the film. Correlation of surface potential measurements and photocatalytic data should confirm this supposition.

5.2 Experimental Methods

5.2.1 Catalyst preparation

All catalysts were prepared using sol-gel methods [25,26]. The titania sol was prepared by adding titanium isopropoxide, $\text{Ti}(\text{OPri})_4$ (Aldrich, Milwaukee, WI), to an aqueous solution of nitric acid at a volumetric mixing ratio of 1 HNO_3 : 136.4 H_2O : 11.4 $\text{Ti}(\text{OPri})_4$. The zirconia sol was prepared by adding zirconium propoxide, $\text{Zr}(\text{OPrn})_4$ (Aldrich, Milwaukee, WI), to an aqueous solution of nitric acid at a volumetric mixing ratio of 1 HNO_3 : 50 H_2O : 3.7 $\text{Zr}(\text{OPrn})_4$. The individual sols were stirred continuously for 3-5 days until peptization was complete. The sol mixture consisted of 12% ZrO_2 and 88% TiO_2 . The unmodified acidic sols (pH of ca. 1) were dialyzed in ultrapure ($>18 \text{ M}\Omega\text{cm}$) water (Spectra/Por® 3 membrane, 3500 MW cutoff, Spectrum, Laguna Hills, CA) to a final pH of ca. 3. Metals were incorporated in the $\text{ZrO}_2/\text{TiO}_2$ mixed sol by adding an aliquot of an 8 weight percent aqueous metal salt solution and subsequent reduction by addition of NaBH_4 dissolved in a 0.01M NaOH solution. Thin film coatings were applied to borosilicate glass cylinders or “rings” following a dip coating procedure described previously [27]. For surface potential measurements, standard borosilicate microscope slides were coated with the photocatalyst materials following the same procedures used for coating the glass rings. The coated substrates were then fired at 350°C in air for 3 hours using a $3^\circ\text{C}/\text{min}$ ramp and allowing the furnace to cool at its natural rate after firing.

Structural and textural parameters of the materials were obtained from the N₂ adsorption isotherms at 77 K and x-ray diffraction (XRD) analysis of fired xerogels. The surface area measured for the xerogels averaged $230 \pm 10 \text{ m}^2/\text{g}$. XRD analysis indicated no distinct variation in catalyst crystallinity due to platinum loading and only the anatase crystalline phase of TiO₂ was detected.

5.2.2 Photocatalytic Testing

A photocatalytic reactor similar to that described previously [27] was used in this study, but with slight modification. Three hundred photocatalyst coated rings (annular tubes, with 3-mm ID; 4-mm OD; 12-mm long) were packed in a 2.5 cm (dia) x 30 cm (long) borosilicate glass column (Ace Glass Vineland, NJ). The column was surrounded by eight 8-W (Sylvania model F8T5, Danvers, Massachusetts) blacklight (BL) fluorescent bulbs. These bulbs/lamps were located 3.8 cm away from the centerline of the reactor and were evenly spaced every 45°. The lamps had a peak wavelength (λ_{peak}) of 365 nm and generated average, steady-state light irradiances of 4.1 ± 0.20 , 3.05 ± 0.09 , and $2.38 \pm 0.37 \text{ mW}\cdot\text{cm}^{-2}$ at 50, 75, and 100°C, respectively. Light irradiance was measured at the center of the glass column using a ramp probe light meter (250–400 nm wavelength range, IL1400, International Light, Newburyport, MA). The lamps and glass column were held in place by a piece of cylindrically-shaped (28 cm long and 12.7 cm diameter) sheet metal.

The entire reactor was placed in a Yamato DKN-600 mechanical convection oven (Santa Clara, CA), which allowed for maintaining control of the reactor and gas temperature during experiments. J-type thermocouple probes (P/N TC-J-NPT-G-72-SMP, Omega

Engineering Inc., Stamford, CT) measured gas temperatures at three locations – reactor inlet and outlet and within the oven chamber directly above the reactor apparatus.

As a probe reactant, we used compressed gas cylinders containing 1009 ppmv propane ($\pm 2\%$) in a balance of hydrocarbon-free air containing less than 0.1 ppmv total hydrocarbons (Linde Gas Co., Madison, WI). Trace levels (< 0.1 ppmv) of acetone, acetaldehyde, isobutane, n-butane, methane and ethane were detected in the propane cylinder. Gas flowrates were controlled by MKS 1179A mass flow controllers (MFC) (MKS Instruments, Wilmington, MA).

The reactor effluent was sampled via a six-way valve with a 250- μ l gas sampling loop connected to a gas chromatograph (Shimadzu GC-2010, Japan). The GC-2010 was equipped with a thermal conductivity detector (TCD) and a flame ionization detector (FID) positioned in series. The capillary column was a 30 m x 0.32 mm Rt-QPLOT (Fused Silica PLOT) from Restek Corp. (Bellefonte, PA). The temperature of the GC oven was maintained at 125°C. All experiments were performed at a flowrate of 50 mL \cdot min $^{-1}$ and 50% relative humidity (RH). To achieve this RH, the feed gas flow was split with a portion of the flow passing through a sparger to attain the desired relative humidity (RH) in the reactor inlet flow. Relative humidity was monitored upstream of the photoreactor (outside of the oven) with a humidity probe (P/N: HMP 235 Vaisala Inc., Woburn, MA). LabviewTM-based software and data acquisition and control hardware (National Instruments, Austin, Texas), employing a (proportional-integral-derivative) PID algorithm, was utilized to monitor the RH of the system and was also used to control the MFCs in order to adjust the flow split to maintain the 50% RH target.

Three reaction temperatures were studied sequentially. The oven temperature was ramped up to 50°C over 5 min, after which the reactor temperature was sustained at 50°C for 65 min. This was followed by a 5-min ramp and 65-min hold time at 75°C followed by a similar ramp to 100°C. A gas sample of the reactor effluent was acquired every 10 min during an entire experiment.

5.2.3 Surface Potential Imaging

Surface potential measurements were obtained with a Digital Instruments Dimension 3100 atomic force microscope (AFM) (Veeco Instruments, Santa Barbara, CA), with an installed electronics extender. Surface potential measurements were acquired via a two-pass process. For each scan line, the topography data was recorded during the first pass. For the second pass, the AFM tip lifted a set distance above the surface and scanned the same line while following the surface topography. The electrostatic forces between the conductive tip and the surface were recorded in the potential image. Further details of the surface potential methodology are available from Digital Instruments [28]. An antimony-doped (n-doped) Si cantilever with a platinum and iridium coated tip (P/N: SCM-PIT, Veeco Instruments, Santa Barbara, CA) was used to scan a 2 x 2 μm square at a scan rate of 1.95 Hz and 512 scan lines. The time to record an AFM-SP image was ~8.5 minutes at this scan rate. The lift height was 75 nm and the drive amplitude for the potential image was 6 V. Real-time and offline plane-fit for the potential image were turned off during the scan. When used, these options act as averaging filters and subtract the average potential value of all data points in a line (real-time) or of the whole image (offline) from the captured data. Thus, any offset of the measurements

is eliminated and the image is centered on zero. However, it should be noted that we did NOT use these averaging filters as our goal was to measure the difference in the potential offset between dark and illuminated conditions.

Two UV light sources were used during surface potential measurements to illuminate a section of the film approximately 3.5 cm away from the measurement location. The sample was not directly illuminated at the measurement site because UV radiation incident on the cantilever caused a change in the oscillation amplitude. During the first series of experiments, two UV-light emitting diodes (LED) (Type: NSHU590B, Nichia America Corp., Mountville, PA) ($\lambda_{\text{peak}} = 365 \text{ nm}$) wired in series and positioned $\sim 3 \text{ mm}$ above the film surface were utilized to produce a measured irradiance of $14 \text{ mW}\cdot\text{cm}^{-2}$. An area of approximately 2 cm^2 was illuminated by the LEDs. The second UV source used was a UV fiber guide (SuperSpot Max™ M/N: VSM3002, American Ultraviolet Company, Torrance, CA) with built-in IR filter, UV output range of 315 – 400 nm, and fitted with a single-leg fiber guide (P/N: OLB1062). The UV fiber guide was fixed $\sim 8 \text{ cm}$ above the film surface. The irradiance at the film surface was $45 \text{ mW}\cdot\text{cm}^{-2}$ incident over an approximate area of 6.3 cm^2 . A light detector (M/N: SSD001A, 250–400 nm wavelength range) and photometer (IL1400) from International Light Corp. (Newburyport, MA) were used to measure irradiance at the point of illumination. The AFM-SP system is schematically depicted in Figure 5.1.

5.3 Results and Discussion

5.3.1 Photocatalytic Oxidation Reaction Observations

Photocatalytic conversion of propane is depicted in Figure 5.2. The reactor temperature profile is shown to illustrate the transition of the temperature during the course of an experiment. Inspection of this figure indicates that the conversion of propane decreased as platinum content in the film increased. This observation suggests that the binary metal oxide mixture itself is optimal for maximizing photocatalytic activity, with modification of the oxide mixture via Pt loadings producing sub-optimal performance. It is noted that the spike (increase) in effluent propane concentrations as the reactor transitioned between temperatures suggests that propane adsorbed on the thin film surface was initially desorbed immediately as the thermal energy increased. Once the reactor temperature attained steady-state at the next oven temperature plateau, surface species' concentrations stabilized as evident via observing the propane effluent asymptotically approaching steady-state concentrations.

The corresponding time history of CO₂ concentrations in the effluent is plotted in Figure 5.3. These data demonstrate similar profiles as observed with propane effluent concentrations, but with a negative spike in CO₂ effluent during the thermal transitions. These CO₂ concentration profiles strongly suggest that propane is indeed driven off of the photocatalyst surface, decreasing the interaction between activated surface sites and propane molecules. Previously [8], we reported that the adsorption coefficient of the Langmuir-Hinshelwood-Hougen-Watson (LHHW) kinetic model decreased considerably (approximately four orders of magnitude) as temperature increased from 35°C to 100°C, while the LHHW reaction rate constant exhibited an approximate four order of magnitude increase as

temperature was increased. Moreover, these observations (Fig. 5.2 and 5.3) are supported by our previous study [8] wherein it was demonstrated that the irradiance in the reactor decreased with increasing reactor temperatures between 35°C and 100°.

5.3.2 Surface Potential

Figure 5.4a illustrates the results of a topography (left) and surface potential (right) scan for the $\text{ZrO}_2/\text{TiO}_2$ coating during an off – on sequence of the LEDs as indicated in the potential image on the right-hand side. The top of the images in Figure 5.4a corresponds to the beginning of the 8.5 minute scan. From analysis of the topography scan we determined the film to be a relatively homogenous surface consisting of particles between 41 and 58 nm. A change in color of the potential image was instantly noticeable after the LEDs were energized signifying a change in the measured surface potential (the color scale is not shown in Figure 5.4a). The lack of fine detail in the surface potential image was a result of the real-time and offline plane-fit settings during the scan as well as the homogenous nature of the film.

Figure 5.4b illustrates a section analysis (the section is indicated by the white box in the topography image of Figure 5.4a) which depicts the potential profile over the time-course of the scan. In a box section analysis the plotted potentials are the average of each scan line instead of just a single data point and thus provide a better representation of the potential across the homogeneous film. The change in scale for the potential profile makes the change between dark and illuminated conditions easily discernable. The surface potential (SP) of the film was very consistent during the dark portion of the scan at an average potential of 443 mV

(determined by a roughness analysis of the dark portion of the scan). Again, the response of the film when the LEDs were energized was immediate; signified by the distinct jump in measured potential. Roughness analysis of the illuminated portion of the scan yielded an average potential of 546 mV. This equated to a change in potential of 103 mV from dark to illuminated conditions.

Figure 5.5 presents the average potential change from two replicate SP analyses of the 5 thin films studied using the UV-LEDs as the illumination source. The small change in potential observed during analysis of uncoated microscope slides (*substrate* in Fig. 5.5) may be attributed to thermal energy influences on the surface potential. In other words, this small observed SP increase is due to heat (thermal energy) conducted (across the 3.5-cm distance; see Fig. 5.1) from the illuminated area to the measurement area. That is, the UV-LEDs produce a non-trivial amount of heat, producing a surface temperature $> 80^{\circ}\text{C}$ on the LED housing. Glass, being an insulator with low thermal conductivity, did exhibit a small increase in potential that occurred gradually and started approximately two minutes after the LEDs were energized. The delayed response and the small change in potential indicated the measured potential change in the glass substrate can be attributed to heating by the LEDs. Therefore, the thermal conductivity of the photocatalytic films may have affected the surface potential results. The films with higher loadings of platinum may have been more thermally conductive which could be one explanation for the parabolic trend of the surface potential measurements.

In measurements with no platinum loadings (*ZT* in Fig. 5.5), the SP change was highest indicating optimal conditions for charge carrier generation and separation.

However, there was a slight upward slope to the potential profile (which may not be clearly evident in Figure 5.4b) which could be an indication of a heating effect from the LEDs. As platinum was added to the film, surface potential decreased. This observation was attributed to recombination at the platinum particles until a point where the platinum loading was sufficient to induce an increase in SP due to conductive heating influences in the films. In order to evaluate the influence of thermal conductivity on the SP results, a sample of Pilkington Energy Advantage™ glass which has a fluorine-doped tin oxide coating was evaluated. The fluorine-doped tin oxide coating should not have been UV active; consequently, any observed change in potential can be attributed to the thermal conductivity of the thin film. The measured potential change of this material was 57 mV. Additionally, this potential did not reveal a distinct step-change in potential as was observed with the UV-active thin films. Therefore, in experiments wherein thin films were illuminated by UV-LEDs the thermal conductivity of the films likely had a significant influence as an unacceptable artifact on the SP measurements (Fig. 5.5).

Figure 5.6 illustrates the potential change of the thin films when illuminated with the UV fiber guide (i.e., .SuperSpot Max™). In these experimental observations, thermal influences due to heat conduction on the thin films should be negated by the IR filter built into the SuperSpot Max™. The 0.001%Pt-ZrO₂/TiO₂ and the blank slide were not analyzed under these conditions. The higher potentials measured under illumination by the fiber optic light source are due to the more than 3-fold increase in irradiance and a larger surface area being irradiated. Nonetheless, the potential change

of the 1%Pt-ZrO₂/TiO₂ film was lower under these conditions, which can be attributed to an absence of thermal heat-conduction artifact.

As depicted in Figure 5.6 the addition of platinum to the ZrO₂/TiO₂ caused a decrease in the potential change of the films. These observations suggest that the decrease in potential was a direct result of increased recombination of charge carriers at the platinum particles. The enhancement in recombination as the platinum content increased can be rationalized in several ways. As the platinum content increased it is probable that metal clusters formed which could build up excess negative charge thereby attracting holes from the valence band [29]. Additionally, higher platinum content would present a higher number density of particles which has been shown to decrease the charge carrier separation distance and lead to more recombination [13]. Finally, because the reaction condition of 50% RH provides enough water for nearly complete surface coverage of the catalyst [30], it is possible that hydrogen production was taking place at the interface between the platinum and the photocatalyst; consuming electrons that accumulated at the platinum particle and otherwise would form active oxygen species [31]. The platinum particles could also have blocked some of the UV from reaching the TiO₂ in the film; however, others have shown that such an effect was not significant until metal weight loading exceeded 3 wt %, at which point surface coverage surpassed 10% [32]. The observations presented in Figure 5.6 also correlate with the relative (reaction kinetic) activity of the films for the photocatalytic destruction of propane. From this we conclude that AFM-SP imaging can be a useful technique as a qualitative means to quickly compare the photocatalytic activity of thin films in the gas

phase. The use of such an analysis could save time and money in the development of new photocatalytic coatings for self-cleaning surfaces and photocatalytic films. Films that display high surface potentials under UV illumination can then be studied further using traditional quantification methods such as Fourier Transform Infrared (FTIR) spectroscopy [33-35] or gas chromatography [2,6,8,36-38]

Another interesting phenomenon observed during surface potential imaging was the failure of the films to fully recover to pre-illumination potential levels immediately after the light was turned off. In addition, the duration of the post – illumination, elevated film potentials showed evidence of a dependence on the irradiance. Figure 5.7 a and b depict section profiles of the $\text{ZrO}_2/\text{TiO}_2$ potential images captured when the light source was turned on and off during the course of a scan (8.5 min). Figure 5.7a was captured when the UV-LEDs were the source of illumination. Figure 5.7b was captured while the UV fiber guide was the source of illumination. When the LEDs were first energized, point 1 in Figure 5.7a, the initial potential change was 108 mV. When the LEDs were turned off (point 2), the potential immediately decreased approximately 58 mV, followed by a gradual decay of ~15 mV over the next 2.7 minutes at which point the LEDs were re-energized (point 3) and the potential increased ~71 mV. Again the LEDs were turned off (point 4) and the potential initially decreased ~63 mV followed by a steady but small potential decrease with time. By comparison, the potential decay depicted in Figure 5.7b did not show the immediate drop in potential that was observed under illumination by the LEDs. Upon removing (de-energizing) the high-intensity

illumination of the UV fiber guide (point 5), the potential decayed exponentially over the course of the 8.5-min scan, engendering a potential drop of approximately 153 mV.

The slow discharge of photoactivated potential in the films may be ascribed to charge trapping at surface states in the film between the ZrO_2 and TiO_2 particles. A similar phenomenon has previously been reported in surface potential measurements of photoactivated thin films of WO_3 - TiO_2 with trapping at interfacial sites between the WO_3 and TiO_2 nanoparticles rationalized as the cause [21]. Moreover, observations of the dependency of charge-carrier lifetime on illumination intensity have also been reported in photoconductivity experiments with reported charge-carrier lifetimes up to 10^4 seconds [39-41].

5.4 Conclusion

Thin films of $\text{ZrO}_2/\text{TiO}_2$ were successfully synthesized containing low weight loadings of platinum and tested for oxidation of propane in a single-pass photocatalytic reactor. The photoactivity of the thin films was further characterized by AFM-SP measurements assessing the change in film potential between dark and illuminated conditions. Photocatalytic activity of the thin films decreased as the quantity of platinum loaded into the films increased between 0.001 wt % and 1 wt %. Surface potential measurements demonstrated a similar trend of decreasing change at higher platinum loadings when heat conduction effects from the UV source were negated. These observations lead one to conclude that surface potential measurements may

provide a means to quickly evaluate the photoactivity of thin film coatings for gas phase applications. Furthermore, the capacity of surface potential measurements to monitor the decay of post-illumination film activity was reported.

References

- [1] J.L.Falconer, K.A.Magrini-Bair, J. Catal. 179 (1998) 171-178.
- [2] X.Z.Fu, L.A.Clark, W.A.Zeltner, M.A.Anderson, J. Photochem. Photobiol. A 97 (1996) 181-186.
- [3] J.C.Kennedy, A.K.Datye, J. Catal. 179 (1998) 375-389.
- [4] A.V.Vorontsov, E.N.Savinov, Z.S.Jin, J. Photochem. Photobiol. A 125 (1999) 113-117.
- [5] A.V.Vorontsov, V.P.Dubovitskaya, J. Catal. 221 (2004) 102-109.
- [6] M.E.Zorn, D.T.Tompkins, W.A.Zeltner, M.A.Anderson, Environ. Sci. Technol. 34 (2000) 5206-5210.
- [7] X.Z.Fu, W.A.Zeltner, M.A.Anderson, Appl. Catal. B 6 (1995) 209-224.
- [8] T.M.Twesme, Oxidation of Light Alkanes Using Photocatalytic Thin Films, Ph.D. Thesis, Chapter 4, University of Wisconsin-Madison, Madison, WI, 2006.
- [9] U.Rodemerck, D.Wolf, O.V.Buyevskaya, P.Claus, S.Senkan, M.Baerns, Chem. Eng. J. 82 (2001) 3-11.
- [10] Y.Yazawa, N.Kagi, S.Komai, A.Satsuma, Y.Murakami, T.Hattori, Catal. Lett. 72 (2001) 157-160.
- [11] Y.Yazawa, N.Takagi, H.Yoshida, S.Komai, A.Satsuma, T.Tanaka, S.Yoshida, T.Hattori, Appl. Catal. A 233 (2002) 103-112.
- [12] X.Z.Fu, W.A.Zeltner, M.A.Anderson, 1995, pp. 209-224.
- [13] M.Sadeghi, W.Liu, T.G.Zhang, P.Stavropoulos, B.Levy, J. Phys. Chem. 100 (1996) 19466-19474.
- [14] X.J.Yang, N.Tamai, Phys. Chem. Chem. Phys. 3 (2001) 3393-3398.
- [15] D.W.Bahnemann, M.Hilgendorff, R.Memming, J. Phys. Chem. B 101 (1997) 4265-4275.
- [16] B.A.Smith, D.M.Waters, A.E.Faulhaber, M.A.Kreger, T.W.Roberti, J.Z.Zhang, J. Sol-Gel Sci. Technol. 9 (1997) 125-137.
- [17] K.Miyashita, S.Kuroda, S.Tajima, K.Takehira, S.Tobita, H.Kubota, Chem. Phys. Lett. 369 (2003) 225-231.

- [18] N.Chandrasekharan, P.V.Kamat, J. Phys. Chem. B 104 (2000) 10851-10857.
- [19] J.J.Sene, W.A.Zeltner, M.A.Anderson, J. Phys. Chem. B 107 (2003) 1597-1603.
- [20] V.Subramanian, E.E.Wolf, P.V.Kamat, J. Am. Chem. Soc. 126 (2004) 4943-4950.
- [21] S.J.Wang, G.Cheng, X.H.Jiang, Y.C.Li, Y.B.Huang, Z.L.Du, Appl. Phys. Lett. 88 (2006).
- [22] A.Chavezpirson, O.Vatel, M.Tanimoto, H.Ando, H.Iwamura, H.Kanbe, Appl. Phys. Lett. 67 (1995) 3069-3071.
- [23] T.Meoded, R.Shikler, N.Fried, Y.Rosenwaks, Appl. Phys. Lett. 75 (1999) 2435-2437.
- [24] M.Gratzel, Heterogeneous Photochemical Electron Transfer, CRC Press, Boca Raton, FL, 1989.
- [25] Q.Y.Xu, M.A.Anderson, J. Mater. Res. 6 (1991) 1073-1081.
- [26] X.Z.Fu, L.A.Clark, Q.Yang, M.A.Anderson, Environ. Sci. Technol. 30 (1996) 647-653.
- [27] T.M.Twesme, D.T.Tompkins, M.A.Anderson, T.W.Root, Appl. Catal. B 64 (2006) 153-160.
- [28] Digital Instruments, in Veeco Metrology Group (Ed.), 2006.
- [29] W.Mu, J.M.Herrmann, P.Pichat, Catal. Lett. 3 (1989) 73-84.
- [30] J.M.Coronado, M.E.Zorn, I.Tejedor-Tejedor, M.A.Anderson, Appl. Catal. B 43 (2003) 329-344.
- [31] H.Haick, Y.Paz, J. Phys. Chem. B 107 (2003) 2319-2326.
- [32] I.M.Arabatzis, T.Stergiopoulos, D.Andreeva, S.Kitova, S.G.Neophytides, P.Falaras, J. Catal. 220 (2003) 127-135.
- [33] J.M.Coronado, S.Kataoka, I.Tejedor-Tejedor, M.A.Anderson, J. Catal. 219 (2003) 219-230.
- [34] C.Hagglund, B.Kasemo, L.Osterlund, J. Phys. Chem. B 109 (2005) 10886-10895.
- [35] M.D.Hernandez-Alonso, I.Tejedor-Tejedor, J.M.Coronado, J.Soria, M.A.Anderson, Thin Solid Films 502 (2006) 125-131.
- [36] A.Sirisuk, C.G.Hill, M.A.Anderson, Catal. Today 54 (1999) 159-164.

- [37] T.M.Twesme, D.T.Tompkins, M.A.Anderson, T.W.Root, Appl. Catal. B 64 (2006) 153-160.
- [38] M.E.Zorn, D.T.Tompkins, W.A.Zeltner, M.A.Anderson, Appl. Catal. B 23 (1999) 1-8.
- [39] Z.Xie, V.M.Burlakov, B.M.Henry, K.R.Kirov, H.E.Smith, C.R.M.Grovenor, H.E.Assender, G.A.D.Briggs, M.Kano, Y.Tsukahara, Phys. Rev. B 73 (2006).
- [40] A.Brajsa, K.Szaniawska, R.J.Barczynski, L.Murawski, B.Koscielska, A.Vomvas, K.Pomoni, Opt. Mater. 26 (2004) 151-153.
- [41] K.Pomoni, A.Vomvas, C.Trapalis, Thin Solid Films 479 (2005) 160-165.

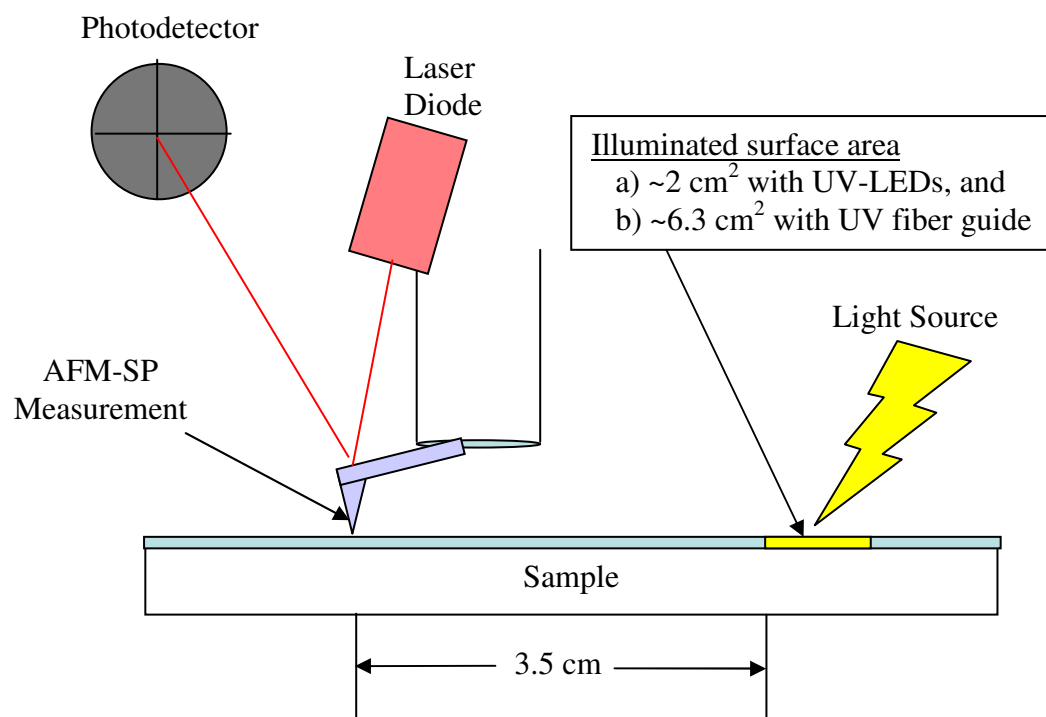
Figures

Figure 5.1 Experimental setup of the AFM-SP system. (drawing not to scale)

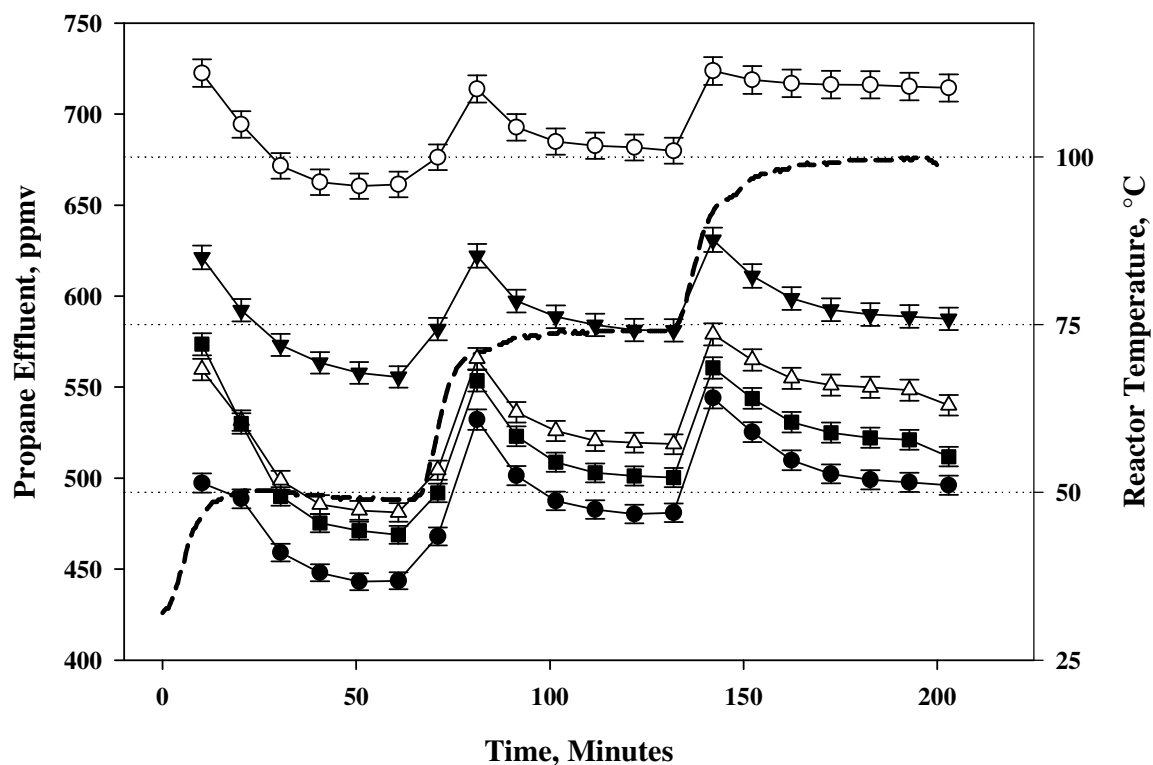


Figure 5.2 Time course of propane effluent concentration from the single pass photoreactor experiments, with superimposed reactor temperature (right-hand side). 1000 ppmv C_3H_8 at inlet to reactor with 50% RH. (●) ZrO_2/TiO_2 , (■) 0.001%Pt, (△) 0.01%Pt, (▼) 0.1%Pt, and (○) 1%Pt. ----- Reactor Temperature.

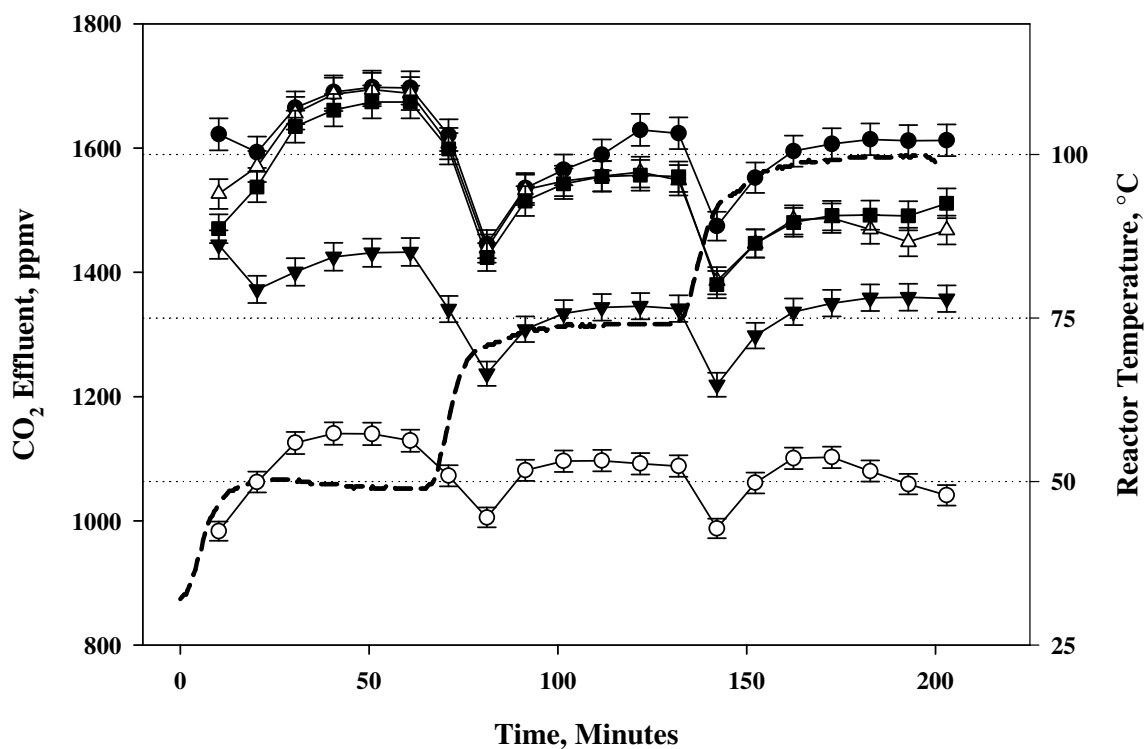


Figure 5.3 Time course of CO₂ effluent concentration from the single pass photoreactor experiments, with superimposed reactor temperature (right-hand side). 1000 ppmv C₃H₈ at inlet to reactor with 50% RH. (●) ZrO₂/TiO₂, (■) 0.001%Pt, (△) 0.01%Pt, (▼) 0.1%Pt, and (○) 1%Pt. ----- Reactor Temperature.

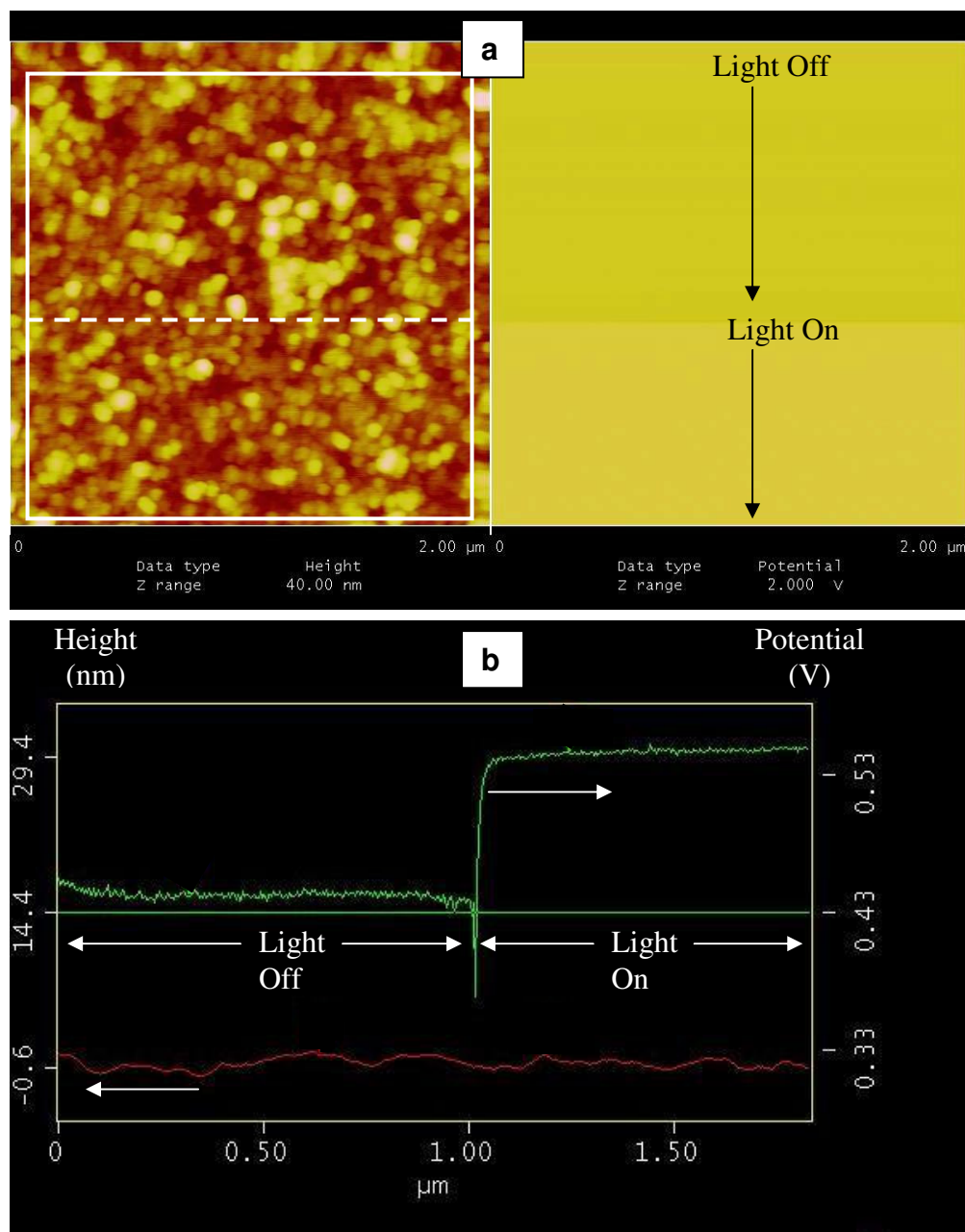


Figure 5.4 a) Topography and surface potential image of $\text{ZrO}_2/\text{TiO}_2$ thin film under dark and illuminated conditions. Scan proceeded from top to bottom beginning with dark conditions. UV-LEDs as light source with a measured surface irradiance of $14 \text{ mW}\cdot\text{cm}^{-2}$. b) Section analysis depicting the average height profile (bottom curve – left axis) and average potential profile (top curve – right axis). The area profiled is designated by the box in the topography image in Figure 5.4a. Left to right in the profile graph corresponds to top to bottom in the images, centered about the dashed line in the box. The average along the width of each scan line in the box is plotted.

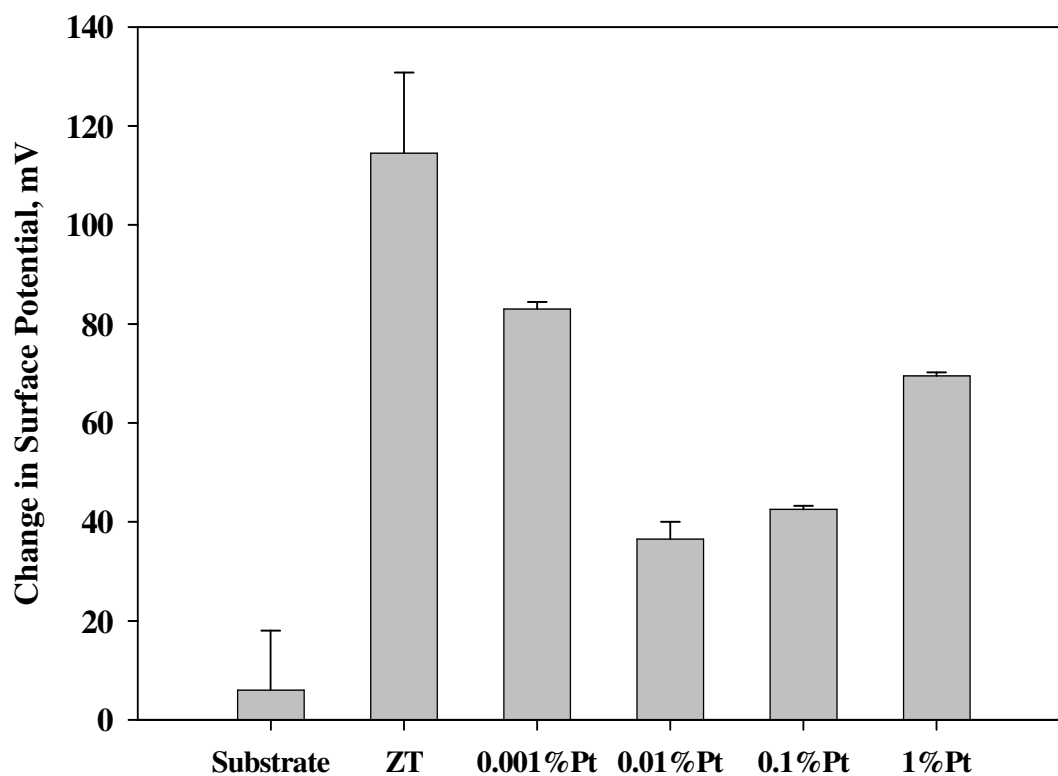


Figure 5.5 Measured surface potential change of $\text{ZrO}_2/\text{TiO}_2$ and platinum loaded $\text{ZrO}_2/\text{TiO}_2$ thin films (and a control - the *substrate*) between dark and illuminated conditions upon exposure to UV-LEDs, with measured surface irradiance of $14 \text{ mW}\cdot\text{cm}^{-2}$. Surface potentials are averages of two replicate experiments.

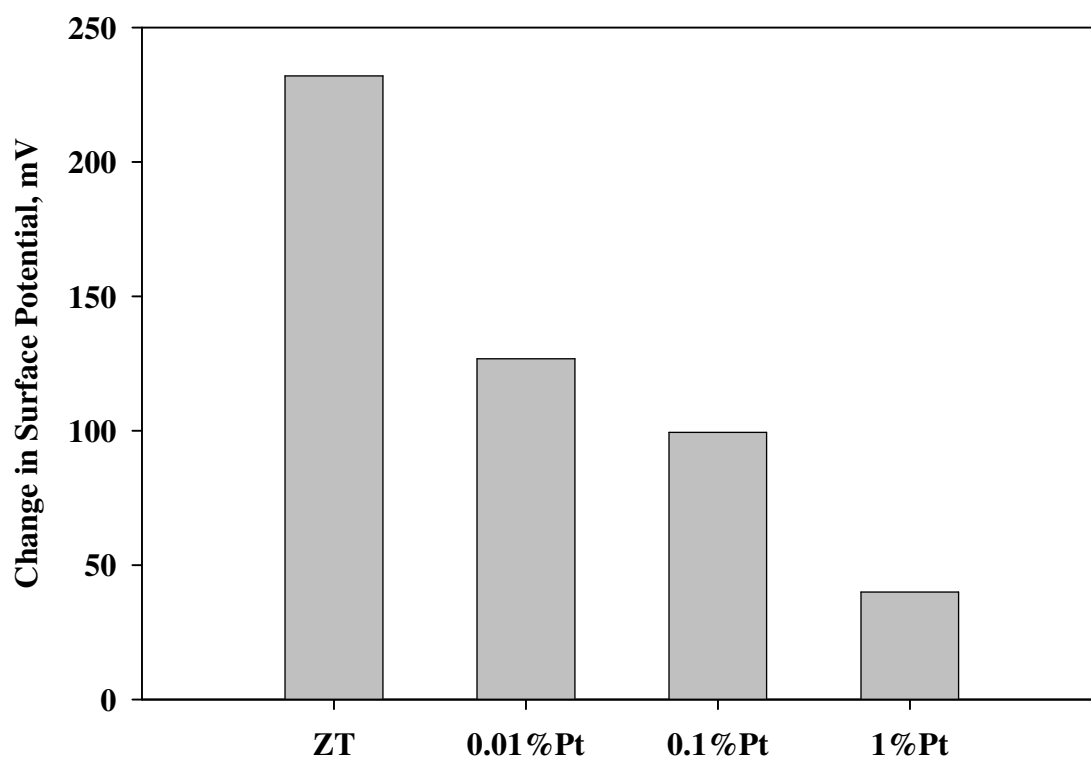


Figure 5.6 Measured surface potential change of ZrO₂/TiO₂ and platinum loaded ZrO₂/TiO₂ thin films between dark and illuminated conditions upon exposure to the UV fiber guide as the UV source with measured surface irradiance of approximately 45 mW-cm⁻². Surface potentials are based on single measurements i.e., $n = 1$.

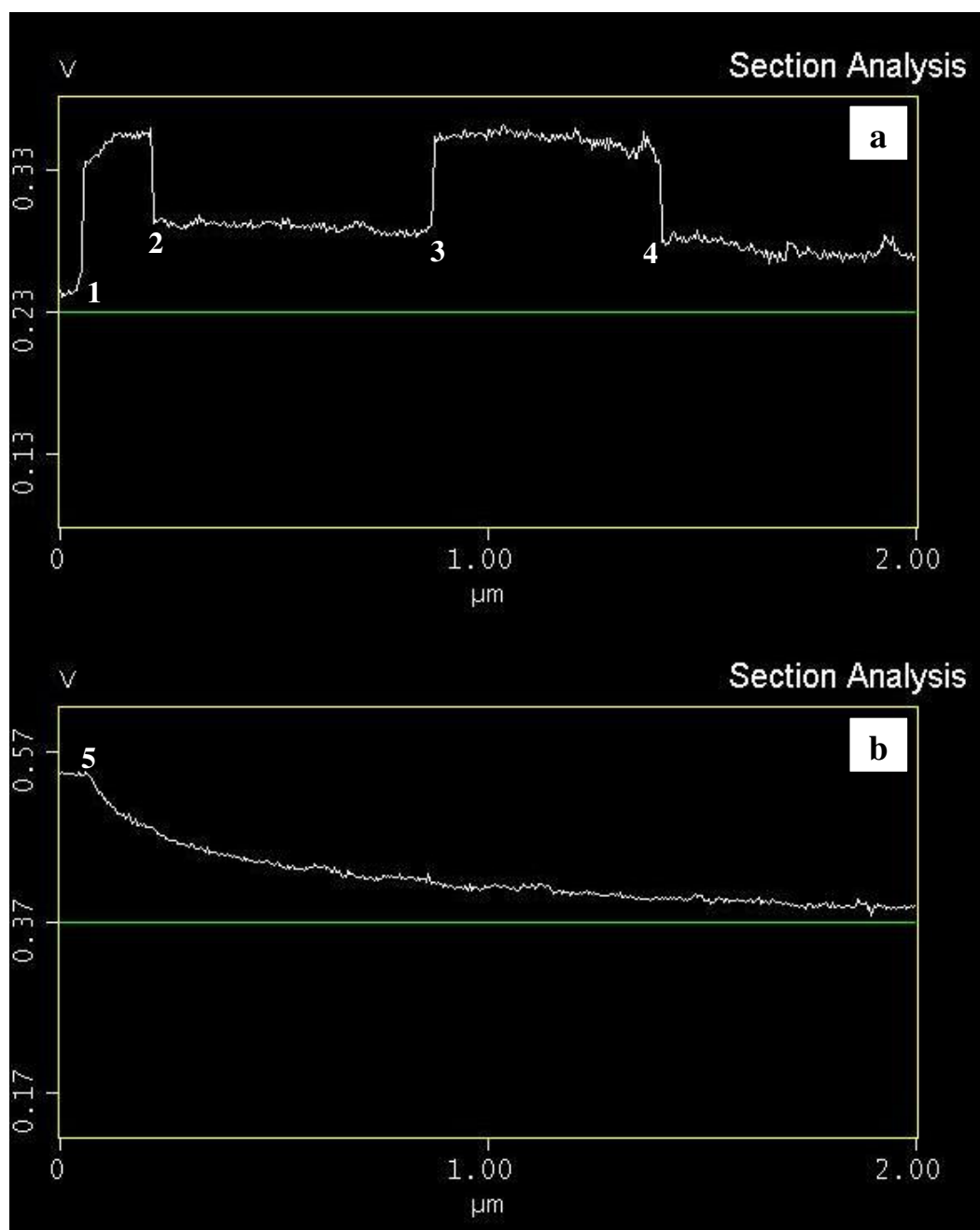


Figure 5.7 Surface potential section analyses depicting potential decay associated with on – off transitions of the illumination source during the timecourse (proceeding left to right) of a scan for the $\text{ZrO}_2/\text{TiO}_2$ sample. Arabic numbers located next to the potential curves indicate switching on or off of the illumination source as listed below. **a)** UV-LED illuminated with measured surface irradiance of $14 \text{ mW}\cdot\text{cm}^{-2}$. **1** – On, **2** – Off, **3** – On, **4** – Off **b)** UV fiber guide illuminated with measured surface irradiance of $45 \text{ mW}\cdot\text{cm}^{-2}$. **5** – Off.

Chapter 6

Concluding Remarks and Suggestions for Future Research

6.1 Concluding Remarks

Light alkanes are invariably one of the most challenging groups of compounds to photocatalytically oxidize owing to their simple and stable chemical structure. Yet, via research presented herein we demonstrate nearly complete oxidation of isobutane, n-butane and propane using $\text{ZrO}_2/\text{TiO}_2$ and several other thin film coatings. We demonstrated that relative humidity had little affect on the reaction rate of light alkanes, but higher humidity did promote the production of intermediate compounds. We also demonstrated that operating at elevated reactor temperatures was not beneficial to the oxidation of propane or minimization of reaction intermediates. Poor performance at elevated temperatures was linked to reduced irradiance from the UV lights and decreased adsorption affinity of contaminants on the photocatalyst surface. Additionally, precious metals loaded into our thin films did not improve the rate of the desired photocatalytic reaction as has been documented for many other VOCs.

A novel method using AFM-captured surface potential measurements to assess the relative photocatalytic activity of thin films was demonstrated. The utility of surface potential measurements for monitoring the photoinduced activity of thin films and the proposed existence of a relationship between measured potential change and photocatalytic activity is a promising development. The use of such a technique as a qualitative means to compare the activity of thin film coatings has *potential* in a myriad of thin film coating applications.

6.2 Suggestions for Future Work

The principal objective of the photocatalytic studies described herein was the desire to identify an active material (or photocatalyst) and suitable reaction conditions that would effectively and optimally oxidize a feedstream of gas containing a 1000-ppmv alkane mixture at a reaction rate sufficiently fast to suit development of a large-scale reactor for use at a manufacturing facility. Initial testing yielded promising results for complete oxidation, but the predicted reactor size based on reaction rate data was exorbitant. Indeed, nearly 1000 m³ of support *active* materials (photocatalyst) would be required to achieve a 50% conversion! Through improving the design and operation of our test reactor, the estimated quantity of supported photocatalyst has decreased to 90 m³ for 90% conversion – roughly the equivalent of one semi-truck load. However, we did not attain further improvements or reduction in quantity of supported photocatalyst through modification of the photocatalyst. Therefore, we believe that improving reactor design, rather than improving the *active* material itself, is where advances can be made to render the PCO of challenging compounds, like light alkanes, more feasible for commercial application.

Other than the prohibitive cost of building a large PCO reactor, the weight associated with glass *rings* used as catalyst supports may limit future development and implementation. For example, in the scenario describe above where approximately 90 m³ of coated rings is required, the weight of the *rings* is estimated at 90 tons. The handling of this quantity of material and the development of a design that could provide the structural support necessary to carry the weight of the catalyst rings, while not hindering operation and maintenance of the

lights, is not trivial. A possible option to help alleviate some of the weight of the catalyst would be the use of plastic supports for the thin films.

Plastic supports would be significantly lighter; however, they also present a noteworthy challenge. The final step in the synthesis of our thin film photocatalysts currently consists of a heating process to affix the film to the support and to sinter the film promoting crystallization of the TiO_2 to the anatase polymorph. This heating step usually occurs at 350°C which is well above the melting point of most plastics. Fortunately, recent work in our laboratory has demonstrated UV-promoted sintering of our films [1]. Thus, it is plausible to conclude that our materials could be coated on plastic media, placed in a photoreactor without having to undergo a heating process, and over the course of time (perhaps a couple of weeks) the films would sinter due to UV light and the heat from the lamps.

The use of AFM-SP methods to investigate photoactivated processes of thin films in the gas phase is an exciting area of research. The recent utilization of AFM-SP in characterizing photo-induced activity and our results herein demonstrate an apparent link or correlation between film surface potential and photocatalytic activity. These observations suggest the creation of a new sub-specialty of research and investigation in photocatalysis to further characterize relationships at the surface level. The list of experiments could include elucidation of the influence of irradiance, wavelength, humidity, surface area, and many other factors. It is my belief that surface potential measurements in the gas phase could become akin to photoelectrochemical measurement of photocurrent in the aqueous phase.

References

- [1] J.R.S.Brownson, T.J.Lee, M.A.Anderson, Chem. Mater. 17 (2005) 3025-3030.

Appendix A

Photoelectrochemical Studies

Part of the original research proposal was that through the photoelectrochemical technique of linear sweep voltammetry (LSV), the photocurrent generated from the photocatalytic thin films would be measured lending insight to the electronic process taking place in the metallized thin films. These experiments were completed for the 21 thin films synthesized as discussed in Chapter 4. However, as is briefly mentioned in Chapter 5, the unique factors that may determine the effectiveness of photocatalytic reactions in a given phase render it difficult to correlate the results of aqueous PEC studies to observed behaviors in gas phase systems. Furthermore, some of the precious metals that were used to dope the nanoparticulate oxides were susceptible to redox reactions over the range of applied potentials. Therefore, this appendix presents the LSV experimental results and a brief discussion in terms of comparing these results to those of the photocatalytic oxidation (PCO) data presented in Chapter 4 and the difficulties encountered that lead to the exploration of the surface potential measurements described in Chapter 5.

A.1 Materials and Methods

Photoelectrochemical studies were conducted using a 30-mL single-compartment Teflon cell, having a 50-mm diameter circular quartz window. A circular opening in the cell opposite the quartz window allowed exposure of 4.5 cm² of the working electrode to

UV illumination. The platinum counter electrode and a saturated calomel electrode (SCE), used as a reference, were placed close to the working electrode. The electrolyte was 0.5 M NaCl and adjustments to the electrolyte pH were made using HOCl or NaOH. Photoelectrodes were synthesized by dip-coating 2.5 cm x 2.5 cm pieces of 0.05 mm titanium foil (Goodfellow Ltd, Devon, PA) using the same coating procedure described in Ch. 4 and 5 for glass rings. Prior to coating and after depositing three coats, the titanium foil was fired at 350 °C for 3 hours at a ramp rate of 3°C/min.

A 500-W Oriel Xe(Hg) arc lamp capable of 200-600-nm excitation wavelengths (with ozone venting) was used as the light source. Source light first passed through a water-cooled IR filter and then on through a Czerny-Turner-style monochromator (with 3-mm slit widths on both sides). Labview™ instrumentation was in place to control the monochromator. A Princeton Applied Research (PAR) potentiostat model 6310 was used to bias the photoanode in the photoelectrocatalytic experiments, and to record the linear sweep voltammetry (LSV) plots for measuring photocurrents. LSV analysis began at an applied potential of -1 V and proceeded at a scan rate of 10 mV·s⁻¹ up to 1 V. Open circuit potential measurements (E_{oc}) were also collected for un-illuminated conditions. The dark open circuit potential accounts for the equilibrium arrived at between the electrolyte and the electrode surface prior to illumination.

A.2 Results

Results of LSV analyses of the 21 electrodes at pH 2 are plotted in Figures A.1a - c corresponding to the TiO₂, SiO₂/TiO₂ and ZrO₂/TiO₂ based photocatalysts,

respectively. The values of current density that are plotted reflect the photocurrent generated relative to the illuminated surface area on the electrode. The TiO₂ electrode produced the highest sustained anodic photocurrent ($\sim 800 \mu\text{A}\cdot\text{cm}^{-2}$). This was followed by the Ag-S/T and Pd-S/T electrodes at 725 and $675 \mu\text{A}\cdot\text{cm}^{-2}$, respectively. The remaining electrodes produced photocurrents below $450 \mu\text{A}\cdot\text{cm}^{-2}$. Interestingly, the ZrO₂/TiO₂ thin film produced only $65 \mu\text{A}\cdot\text{cm}^{-2}$ even though this thin film coating demonstrated the highest activity for gas phase PCO of propane (see Chapter 4). At this time the reason for the low photocurrent produced by the ZrO₂/TiO₂ is not clear.

The large peaks (spikes) in the curves of the Rh electrodes at ~ 350 mV (Figures A.1a-c) are characteristic of the oxidation of adsorbed hydrogen on the electrode surface according to the reaction:



At applied potentials more negative than ~ -450 mV, hydrogen was readily reduced on the Rh-TiO₂. As the potential was swept past the -450 mV mark and to more positive potentials, the adsorbed hydrogen was oxidized generating the current spike. All of the adsorbed hydrogen was quickly oxidized leading to the decrease in measured current to a point where the photoinduced current was dominant. The current spike was of the largest magnitude at pH 2 because of the high concentration of $\text{H}^+_{(\text{aq})}$, hence at pH 12 this phenomenon was not observed. Similar spikes were observed in other electrodes, but these were generally not as pronounced and occurred at more negative potentials.

Photocurrent measurements were collected at six pH values to provide adequate data for determining flat band potentials of the thin films. The performance of the

electrodes for photocurrent generation varied significantly as the electrolyte pH changed (meaning the electrode with the highest photocurrent at pH 2 did not necessarily have the highest photocurrent at higher pH values). As an example, Figures A.2a and b present the current density versus potential curves for the TiO₂ based electrodes at pH 6 and 12, respectively. Comparing Figure A.1a to A.2a and b we observe that the photocurrent of the unmodified TiO₂ electrode dropped from 800 to 400 to 200 $\mu\text{A}\cdot\text{cm}^{-2}$ at pH 2, 6 and 12, respectively, while the photocurrents of the metal-modified electrodes did not change as dramatically. In fact, in some cases (such as the Au-T and Pt-T) the measured photocurrent was higher at pH 12 than that measured at pH 2 or pH 6. These variations in the effect of pH on electrode performance make comparison to gas phase reactions extremely challenging; especially considering that in a gaseous system an electrolyte species akin to the aqueous phase is likely not present and the surface pH is ill-defined.

There are several possible causes for the observed inconsistency in the effect of pH on the electrodes. Double layer formation at the electrode – electrolyte surface will influence interfacial charge transfer at the electrode surface which is suggested to be a dominant factor affecting photocurrent in nanocrystalline electrodes [1]. It is probable that formation of the double layer was not consistent for all of the electrodes, especially between the TiO₂, S/T and Z/T groups. The photocurrent generated from a semiconductor electrode corresponds to the injection of holes from the valence band into the electrolyte, therefore, it can also be influenced by the dynamics of hole generation, recombination, and transport to the electrode surface [2]. Differences in the density and

nature of surface states due to the presence of the precious metals likely contributed to charge trapping and charge recombination leading to decreases in photocurrent efficiency [1]. Conversely, the magnitude of the photocurrent is dependent on the efficiency of hole scavenging at the electrolyte interface [3] and surface states may have made it easier for the photogenerated holes to transport to the electrolyte solution leading to higher photocurrents for some electrodes [4].

It was also evident from the LSV results that some of the metals were more susceptible to oxidation reactions than others during the experiments. The silver loaded electrodes produced a relatively consistent maximum photocurrent of $> 400 \mu\text{A}\cdot\text{cm}^{-2}$ regardless of pH. We expect the consistency and magnitude of the photocurrent was a result of a reaction between the silver and the NaCl electrolyte. The reaction shown in Eq. A.1, has a standard reduction potential of 222 mV vs NHE [5].

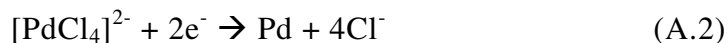


Once the applied potential in the LSV experiments became more positive than this value (~ -20 mV vs. SCE) the reverse reaction occurred producing electrons. Evaluation of the Ag electrodes in another electrolyte such as Na_2SO_4 would provide a means to test this theory.

Similarly, in the ruthenium loaded thin films, oxidation of the ruthenium metal to Ru^{2+} at applied potentials more positive than ~ 230 mV vs. SCE may explain the gradual increase in photocurrent at positive potentials. Palladium metal is susceptible to the reverse of reaction (A.2) at potentials more positive than 349 mV vs. SCE and may also

be oxidized at potentials more positive than 709 mV vs. SCE in accordance with Eq.

A.3. These oxidation reactions may explain the high currents measured for the Pd electrodes.



The flatband potential of the electrodes was determined by the onset photocurrent method as described by Finklea [2]. Using this method, the applied potential when the photocurrent transitions from cathodic to anodic is plotted versus pH. Table A.1 presents the calculated flatband potential (extrapolated to pH 0) for the 21 electrodes along with the slope of the regression line and the R-squared value. The majority of the values lie within the range (-200 to -620 mV vs. SCE) previously reported for similar thin film electrodes [3,6], however several of the curves were not very linear as indicated by the R-squared values.

The amphoteric nature of metal oxides causes surface protonation/deprotonation to occur as pH changes which leads to changes in the potential across the double layer. Such an effect should result in a negative shift in the flat band potential as pH increases and a slope of the regression curve in accordance with Nernstian behavior as shown in Eq. A.4 [2].

$$E_{fb} = E_{fb}^\circ + 0.059 \text{pH} \quad (\text{A.4})$$

However, there is some debate as to whether or not metal oxides surfaces are truly Nernstian [7].

In theory, positive shifts in the flatband potential suggest that the oxidizing power of a photogenerated hole becomes greater; therefore, oxidation of a target species should be easier. Yet, once again, these data do not correlate well with our gas phase PCO data when one considers that the Pd and Ru loaded thin films had the more positive flatband potentials and exhibited very little activity for propane oxidation.

A.3 Conclusion

Thin film electrodes were evaluated via the LSV technique to measure photocurrent and calculate the flatband potential of the thin film coatings. A significant amount of data was collected during PEC studies; yet, the information garnered from these studies is restricted in its application. Although we were able to observe some interesting phenomena, unfortunately little, if any, of the trends identified in the PEC experiments correlated with the gas phase PCO studies.

References

- [1] S.Licht, Semiconductor Electrodes and Photoelectrochemistry, Wiley-VCH, Weinheim, 2002.
- [2] Finklea H.O., Semiconductor electrodes, Elsevier, New York, 1988.
- [3] J.J.Sene, W.A.Zeltner, M.A.Anderson, J. Phys. Chem. B 107 (2003) 1597-1603.
- [4] G.Zhao, H.Kozuka, T.Yoko, Thin Solid Films 277 (1996) 147-154.
- [5] A.J.Bard, R.Parsons, J.Jordan, Standard Potentials in Aqueous Solutions, Marcel Dekker, New York, 1985.
- [6] B.P.Nelson, R.Candal, R.M.Corn, M.A.Anderson, Langmuir 16 (2000) 6094-6101.
- [7] Larson I., Attard P., J. Colloid Interface Sci. 227 (2000) 152-163.

Tables

Table A.1 Calculated flatband potentials extrapolated to pH 0 for thin film electrodes based on measurement of the photocurrent onset potential.

	E_{fb} (mV vs. SCE)	Slope (mV/pH unit)	R²
TiO ₂	-303	-60	.93
Ag-T	-366	-46	.74
Au-T	-275	-64	.89
Pd-T	-210	-41	.66
Pt-T	-505	-49	.54
Rh-T	-339	-71	.69
Ru-T	-40	-46	.53
S/T	-380	-54	.83
Ag-S/T	-291	-47	.86
Au-S/T	-213	-47	.87
Pd-S/T	-7	-64	.91
Pt-S/T	-139	-54	.92
Rh-S/T	-102	-39	.75
Ru-S/T	-36	-66	.83
Z/T	-330	-38	.76
Ag-Z/T	-405	-54	.95
Au-Z/T	-228	-71	.92
Pd-Z/T	-238	-39	.98
Pt-Z/T	-432	-57	.76
Rh-Z/T	-734	-35	.23
Ru-Z/T	-418	-27	.92

Figures

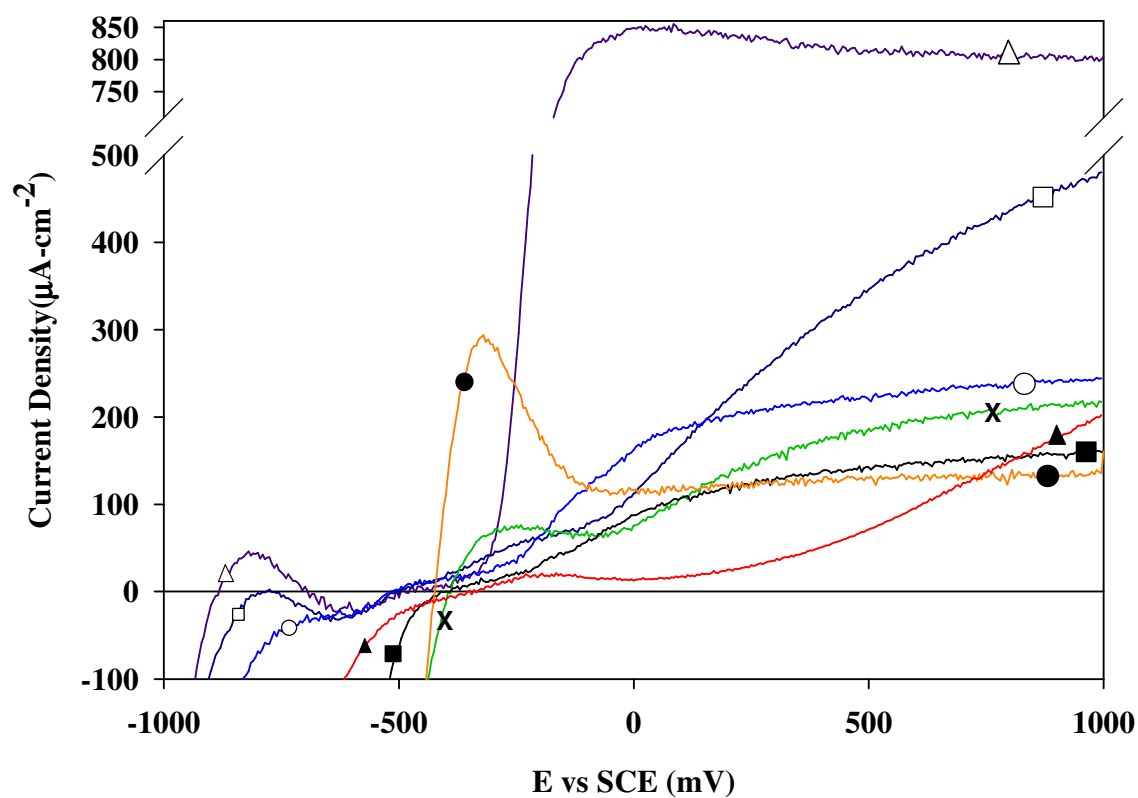


Figure A.1a Current density versus applied potential for TiO_2 -based thin film electrodes at pH 2. $10 \text{ mV}\cdot\text{sec}^{-1}$ scan rate starting at -1000 mV and progressing to 1000 mV . (\triangle) TiO_2 , (\square) Ag-T, (\circ) Au-T, (\times) Pd-T, (\blacksquare) Pt-T, (\bullet) Rh-T, (\blacktriangle) Ru-T.

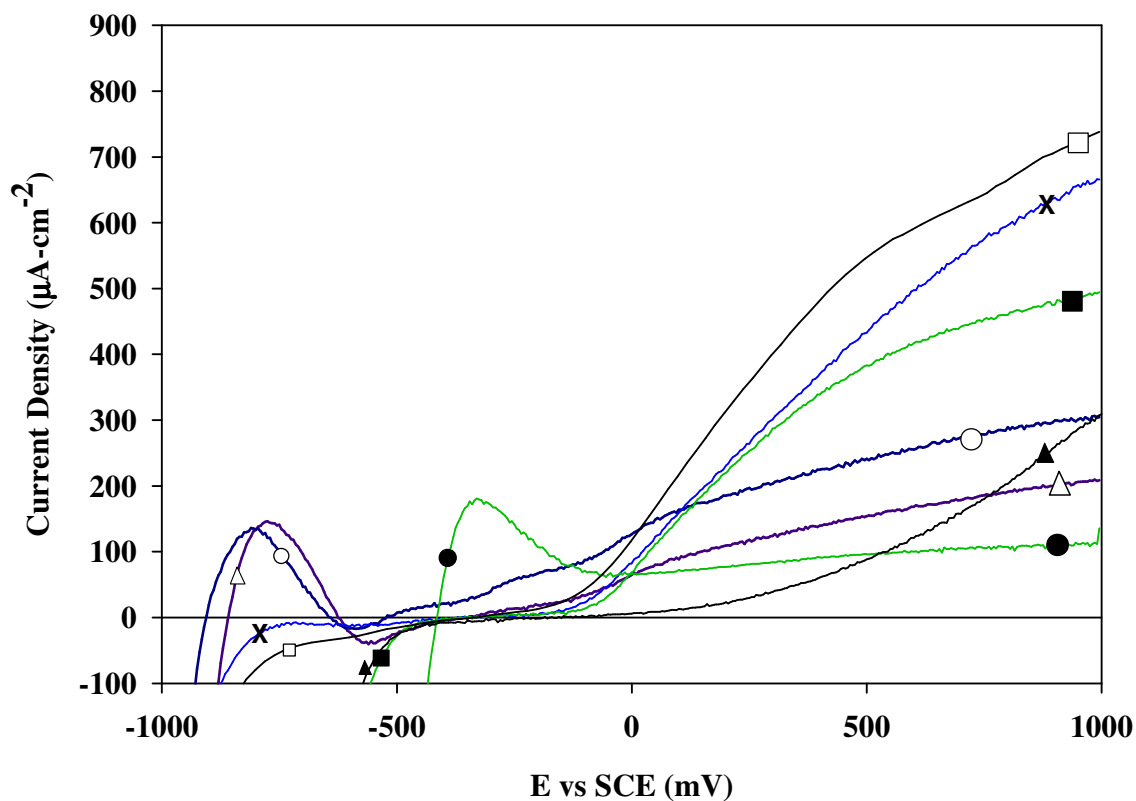


Figure A.1b Current density versus applied potential for SiO₂-TiO₂-based thin film electrodes at pH 2. 10 mV·sec⁻¹ scan rate starting at -1000 mV and progressing to 1000 mV. (△) S/T, (□) Ag-S/T, (○) Au-S/T, (×) Pd-S/T, (■) Pt-S/T, (●) Rh-S/T, (▲) Ru-S/T.

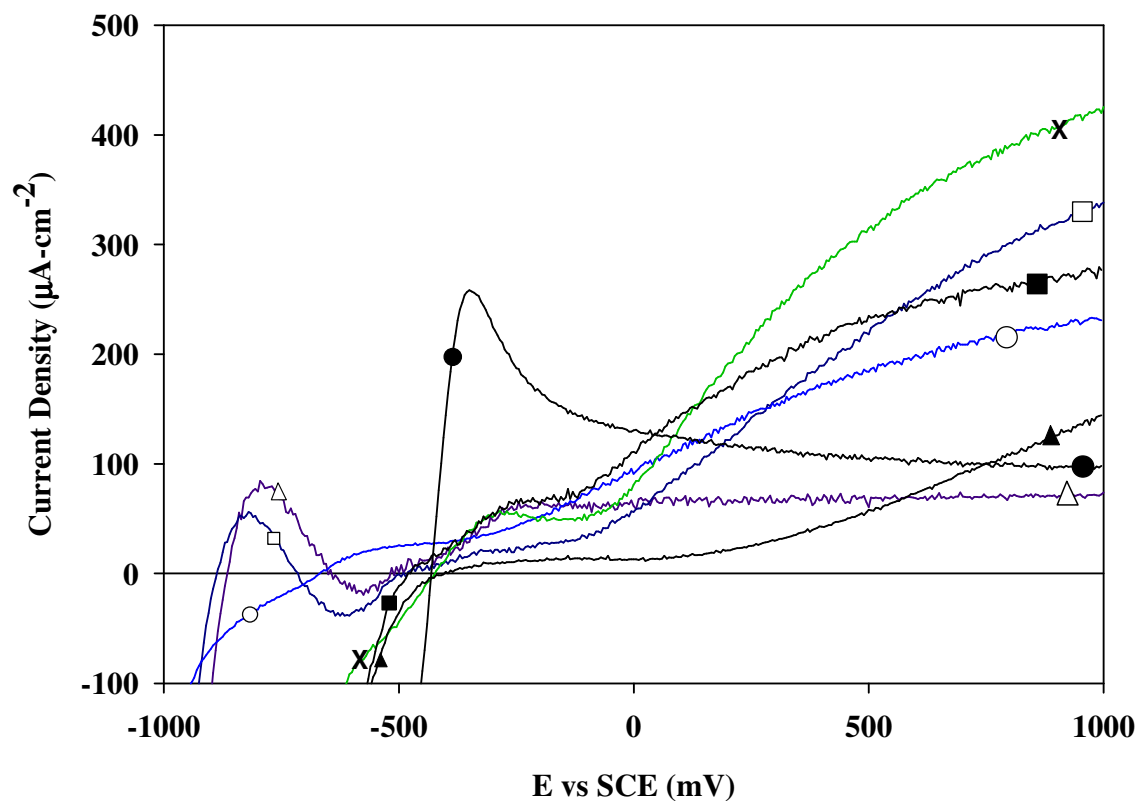


Figure A.1c Current density versus applied potential for ZrO₂-TiO₂-based thin film electrodes at pH 2. 10 mV·sec⁻¹ scan rate starting at -1000 mV and progressing to 1000 mV. (Δ) Z/T, (\square) Ag-Z/T, (\circ) Au-Z/T, (\times) Pd-Z/T, (\blacksquare) Pt-Z/T, (\bullet) Rh-Z/T, (\blacktriangle) Ru-Z/T.

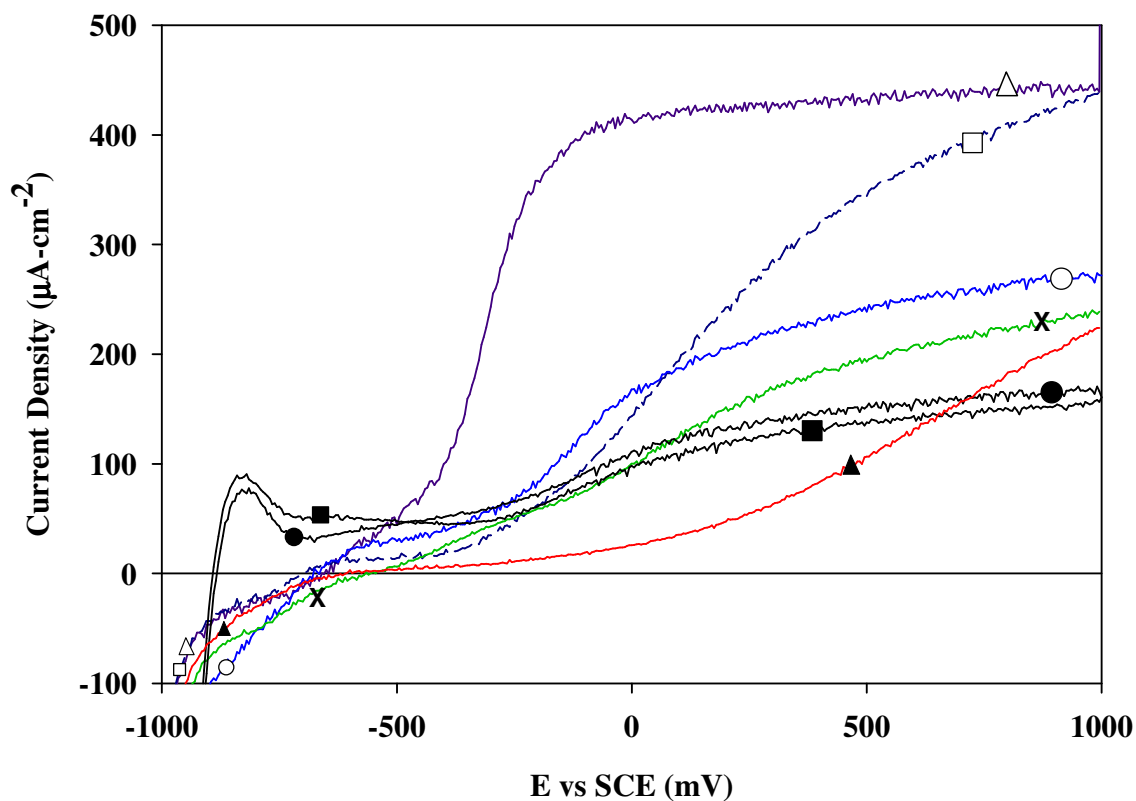


Figure A.2a Current density versus applied potential for TiO₂-based thin film electrodes at pH 6. 10 mV·sec⁻¹ scan rate starting at -1000 mV and progressing to 1000 mV. (Δ) TiO₂, (□) Ag-T, (○) Au-T, (x) Pd-T, (■) Pt-T, (●) Rh-T, (▲) Ru-T.

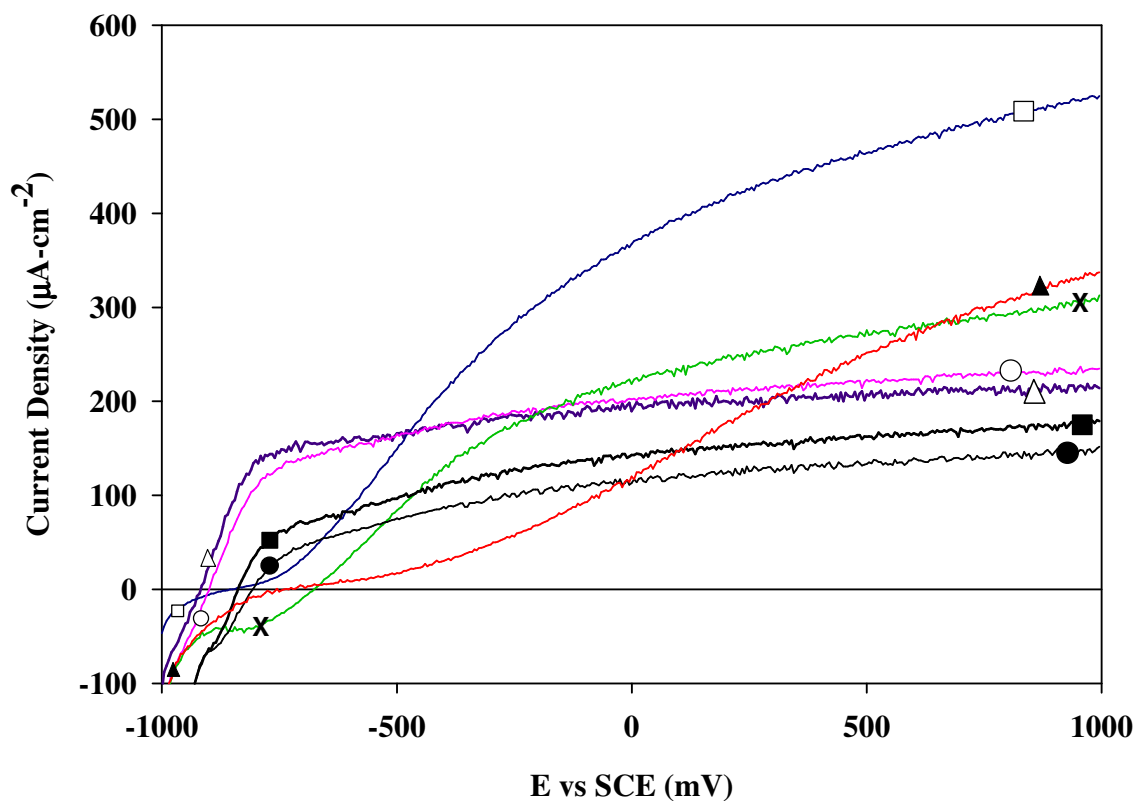


Figure A.2b Current density versus applied potential for TiO₂-based thin film electrodes at pH 12. 10 mV·sec⁻¹ scan rate starting at -1000 mV and progressing to 1000 mV. (△) TiO₂, (□) Ag-T, (○) Au-T, (x) Pd-T, (■) Pt-T, (●) Rh-T, (▲) Ru-T.

Appendix B

Lamp Irradiance

As has been demonstrated in the main text of the thesis, PCO reaction rates correlate strongly with light irradiance. The U.S. market consists of a myriad of ballasts to power several types of UV lamps. This appendix contains the results of an experiment that measured irradiance from new UV lamps. The irradiance of several ballast-lamp combinations are reported for comparison.

B.1 Materials and Methods

Light irradiance (mW cm^{-2}) was determined for five types of new fluorescent UV lamps (cold-cathode) including three so-called *blacklight* (BL) lamps (F8T5BL (WIKO, Japan), F8T5BL (EIKO, Japan), F8T5/350BL (Sylvania, U.S.)) and two so-called *blacklight-blue* (BLB) lamps (F8T5BLB (WIKO, Japan), and F8T5BLB (EIKO, Japan)). [NOTE: Fluorescent BL lamps are white in color due to the white-colored phosphor located on the inner surface of BL lamps, while fluorescent BLB lamps are purple color. Additionally, the glass comprising the BL and BLB lamps is slightly different in material composition.] Lamps were randomly labeled (from 1 to 10) for data recording. Two lamps were powered during any individual experiment, with one lamp powered by a magnetic ballast (Radionic Industries, Chicago, IL) and the other lamp powered by an electronic ballast (M/N: Workhorse 2, Fulham Corp., Hawthorne, CA). Each experiment was initiated by powering the lamps, allowing for a warm-up period lasting 30-40 min. The surface temperature of each lamp was monitored via

J-type thermocouple (Omega Engineering Inc., Stamford, CT) to ensure the temperature of the lamps was consistent between experiments and between lamps (i.e., equal lamp surface temperatures) at the time of irradiance measurement. Thereafter, irradiance measurements were acquired at five locations along the surface of each lamp. The five locations were at the 1/10-, 2/5-, 1/2-, 2/3-, 9/10-locations along the length of the bulb's glass (cylindrical) surface. Replicate (x 2) experiments were performed for each of the lamps. The irradiance was measured with a probe (SuperSlim, International Light Corp., Newburyport, MA) measuring total irradiance between ~250 nm and 400 nm. The probe was connected to a calibrated light meter (IL1400, International Light Corp., Newburyport, MA) that provided the irradiance (mW cm^{-2}). Irradiance measurements were recorded in a laboratory notebook. The irradiance obtained at the center position (1/2-location) of a lamp was used to calculate the mean and standard deviation of lamp irradiance.

B.2 Results

The average irradiance of several lamp-ballast combinations are reported in Fig. B.1, where the irradiance plotted is the irradiance at the lamp's center position and an average of the replicate lamps of each lamp type and for the replicate ($n = 2$) experiments. Similarly, the average irradiance of several lamp-ballast combinations is provided in Fig. B.2. However, in Fig. B.2, the irradiance plotted is an average of all five measurement locations of each lamp and for replicate experiments ($n = 2$) of each lamp. Results indicate that WIKO BL lamps have higher irradiance than WIKO BLB lamps, while EIKO BLB lamps have higher irradiance than EIKO BL lamps. The F8T5/350BL lamp (Sylvania) exhibited the highest

irradiance. All lamps tested demonstrated a higher lamp surface irradiance when powered with an electronic ballast compared to a magnetic ballast. It is noteworthy to indicate that testing performed and reported in Chapter 3 of this thesis utilized the WIKO F8T5BL-magnetic ballast combination, while studies conducted and reported in Chapters 4 and 5 employed the F8T5/350BL-electronic ballast combination. Figure B.3 contains a plot of the fractional conversion of propane versus space time for these two lamp-ballast combinations.

B.3 Conclusion

These observations indicate that selection of lamps and ballasts for application in PCO reactors will have a non-trivial influence on reported reaction rates and overall reactor performance. Additionally, it is known that the lamp irradiance produced by (cold-cathode) fluorescent lamps as studied herein will decay to about 50% of the irradiance of new lamps within about 3 months during 24 hr/day and 7 day/wk operation [1]. Thus, the irradiance of a new UV fluorescent lamp will decay somewhat exponentially and appear to approach asymptotically a *steady-state* lamp irradiance. Therefore, it is highly recommended that modeling and prediction of PCO reactor performance for commercial-scale applications consider and utilize these *steady-state* lamp irradiances.

References

- [1] W.A.Zeltner, D.T.Tompkins, ASHRAE Trans. 111 (2005) 523-534.

Figures

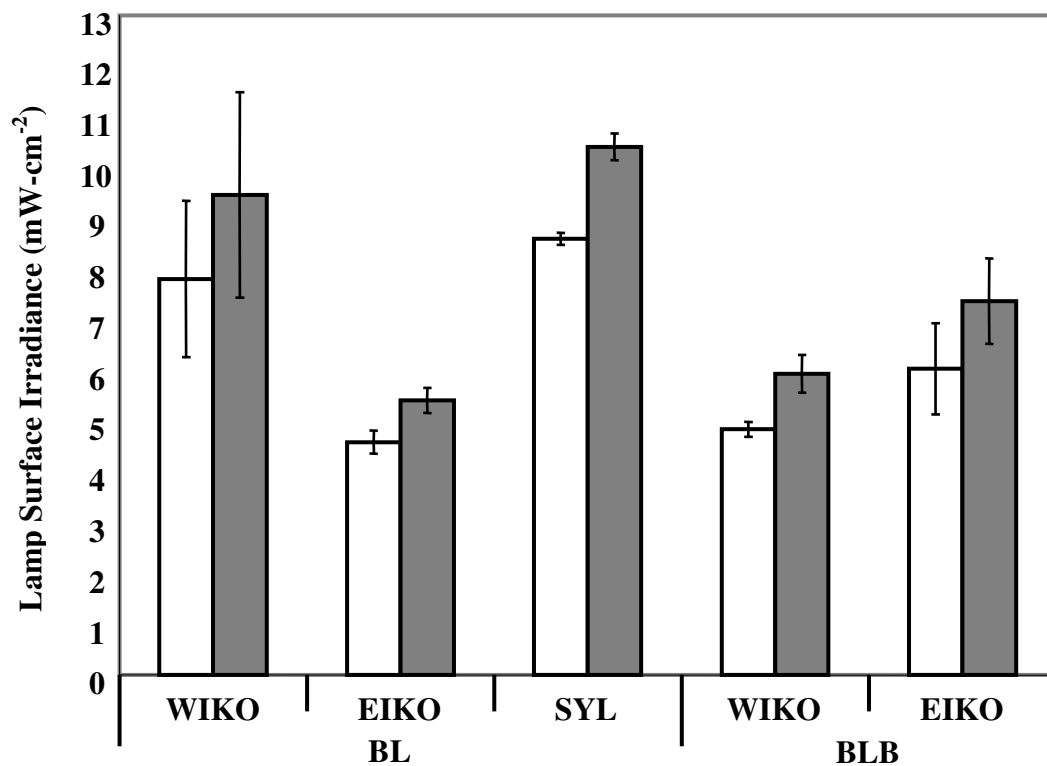


Figure B.1 Irradiance (or intensity) (mW cm^{-2}) of several lamp-ballast combinations. □—magnetic ballast, ■—electronic ballast. [Average irradiance as plotted is the irradiance at the lamp's center position and an average of the replicate lamps of each lamp type and for the replicate (x 2) experiments.]

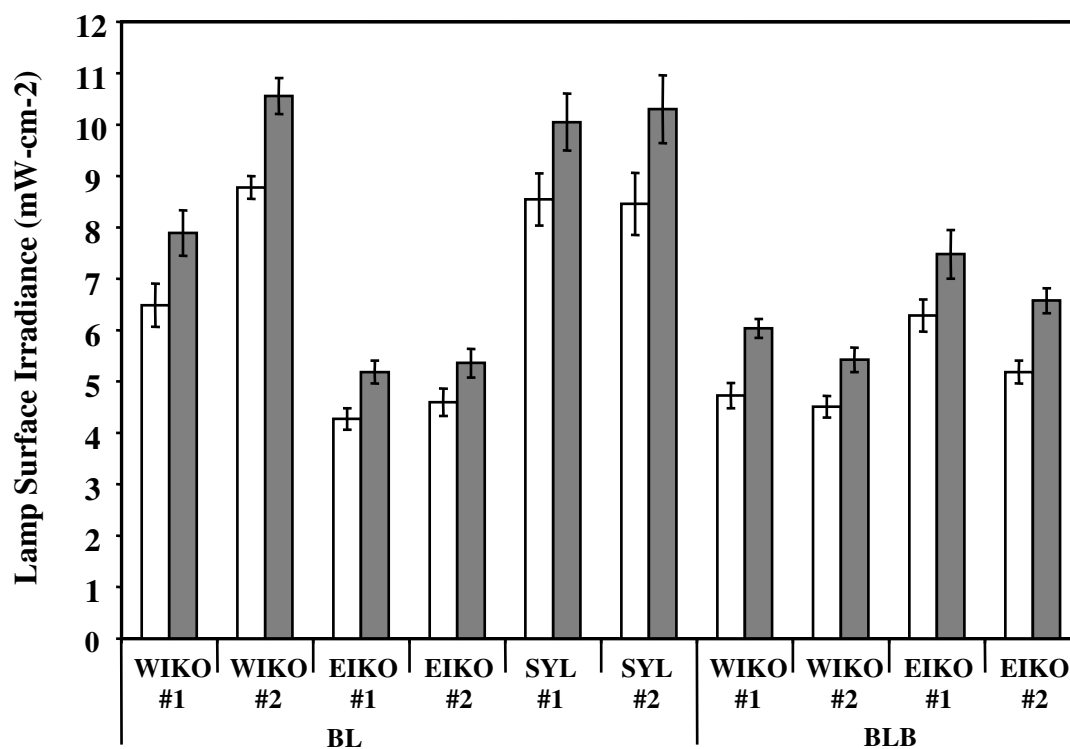


Figure B.2 Irradiance (mW cm⁻²) of several lamp-ballast combinations. □—magnetic ballast, ■—electronic ballast. [Average irradiance as plotted is an average of all five measurement locations of each lamp and for replicate experiments (x 2) of each lamp.]

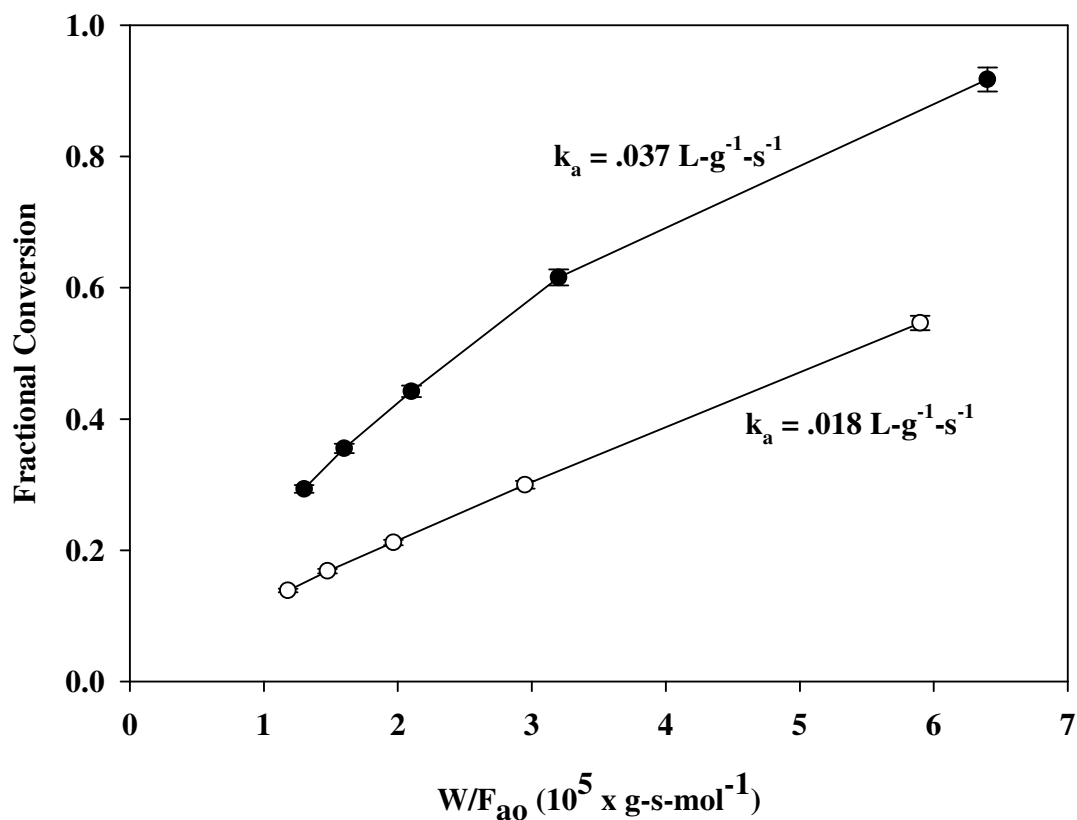


Figure B.3 Fractional conversion versus space time for two lamp-ballast ensembles – WIKO F8T5BLB-magnetic ballast combination (Ch. 3 herein) and F8T5-350BL-electronic ballast combination (Ch. 4 and 5). [Experimental conditions were 1000 ppmv C_3H_8 , 50% RH and 35°C .]